

THEORETICAL VISUALIZATION OF ATOMIC-SCALE PHENOMENA IN  
INHOMOGENEOUS SUPERCONDUCTORS

By

PEAYUSH K. CHOUBEY

A DISSERTATION PRESENTED TO THE GRADUATE SCHOOL  
OF THE UNIVERSITY OF FLORIDA IN PARTIAL FULFILLMENT  
OF THE REQUIREMENTS FOR THE DEGREE OF  
DOCTOR OF PHILOSOPHY

UNIVERSITY OF FLORIDA

2017

© 2017 Peayush K. Choubey

To my mother

## ACKNOWLEDGMENTS

First and foremost, I would like to express deepest gratitude to my advisor Prof. Peter Hirschfeld for his constant support, understanding, and guidance. None of this would have been possible without his wonderful insights, patience, and encouragement. Many thanks to Prof. Dmitrii Maslov for his insightful and crystal-clear lectures. I am especially indebted to my friend and collaborator Dr. Andreas Kreisel for his help and support at various stages of my doctoral work. I would like to thank my collaborators Prof. Brian Andersen, Prof. Ting-Kuo Lee, Prof. Wei Ku, Dr. Tom Berlijn, and Wei-Lin Tu. Without your help I could not have published. I am thankful to former and present group colleagues, Dr. Vivek Mishra, Dr. Yan Wang, Dr. Wenya Rowe, Dr. Andreas Linschied, Dr. Saurabh Maiti, Xiao Chen, Shinibali Bhattacharyya, and Jasdip Sidhu. I would like to thank the members of my supervisory committee, Prof. Pradeep Kumar, Prof. Khandkar Muttalib, Prof. Greg Stewart, and Prof. Juan Nino for their time and expertise to improve my work. I am thankful to David Hansen, Brent Nelson, and Clint Collins for their help with various aspects of computing and other technical support. I thank Physics Department staff for their assistance over past years, especially I express my gratitude to Kristin Nichola, Tessie Colson, and Pam Marlin for their support. I would also like to acknowledge the help and assistance of all my friends at the University of Florida, especially Varun Rishi, Avinash Rustagi, Tathagata Choudhuri, Naween Anand, Pancham Gupta, Akhil Ahir, and Akash Kumar. Finally and most importantly, I would like to thank all my family members for their help, understanding and constant support. I thank my wife, Pallavi, for being a continuous source of encouragement and support to me.

# TABLE OF CONTENTS

	<u>page</u>
ACKNOWLEDGMENTS . . . . .	4
LIST OF FIGURES . . . . .	7
ABSTRACT . . . . .	9
CHAPTER	
1 INTRODUCTION . . . . .	11
1.1 Historical Background . . . . .	11
1.2 BCS Theory . . . . .	12
1.3 Overview of Cuprate Superconductors . . . . .	15
1.4 Overview of Iron-Based Superconductors . . . . .	18
1.5 STM Studies of Superconductors . . . . .	22
2 BOGOLIUBOV-DE GENNES-WANNIER APPROACH . . . . .	26
2.1 Impurities in Superconductors . . . . .	26
2.2 Mean-Field Theory . . . . .	27
2.2.1 Hamiltonian . . . . .	27
2.2.2 BdG Equations . . . . .	29
2.3 Calculation of STM Observables . . . . .	31
2.3.1 Lattice LDOS . . . . .	31
2.3.2 Continuum LDOS . . . . .	32
2.4 Numerical Implementation . . . . .	33
3 IMPURITY INDUCED STATES IN IRON BASED SUPERCONDUCTORS . . . . .	35
3.1 Motivation . . . . .	35
3.2 Normal State Properties of FeSe . . . . .	37
3.3 Homogeneous Superconducting State . . . . .	40
3.4 Effects of an Impurity . . . . .	44
3.5 Conclusion . . . . .	48
4 IMPURITY INDUCED STATES IN CUPRATES . . . . .	50
4.1 Motivation . . . . .	50
4.2 Normal State . . . . .	52
4.3 Homogeneous Superconducting State . . . . .	54
4.4 Effects of a Strong Non-Magnetic Impurity . . . . .	58
4.5 Effects of a Magnetic Impurity . . . . .	60
4.6 Quasiparticle Interference . . . . .	65
4.7 Conclusion . . . . .	68

5	CHARGE ORDER IN CUPRATES . . . . .	70
5.1	Motivation . . . . .	70
5.2	Extended $t - J$ Model . . . . .	75
5.2.1	Renormalized Mean-Field Theory . . . . .	75
5.2.2	Quasi 1D BdG Equations . . . . .	78
5.2.3	Calculation of STM Observables . . . . .	81
5.3	Unidirectional Charge Ordered States in Extended $t - J$ Model . . . . .	83
5.3.1	Anti-Phase Charge Density Wave State . . . . .	86
5.3.2	Nodal Pair Density Wave State . . . . .	90
5.4	Conclusion . . . . .	98
6	SUMMARY AND FINAL CONCLUSIONS . . . . .	100
APPENDIX		
A	DERIVATION OF BOGOLIUBOV-DE GENNES EQUATIONS . . . . .	106
B	SUPERCELL METHOD . . . . .	112
C	ANALYTICAL PROOF OF U-SHAPED CONTINUUM LDOS IN SUPERCONDUCTING BSCCO . . . . .	115
D	MICROSCOPIC JUSTIFICATION OF THE "FILTER" THEORY . . . . .	121
	REFERENCES . . . . .	124
	BIOGRAPHICAL SKETCH . . . . .	136

## LIST OF FIGURES

<u>Figure</u>	<u>page</u>
1-1 $T_c$ versus year of discovery for various superconductors. . . . .	13
1-2 Unit cell of a typical cuprate. . . . .	15
1-3 Schematic phase diagram of hole-doped cuprates. . . . .	16
1-4 Unit cell and Fermi surface of pnictides. . . . .	19
1-5 Schematic phase diagram of iron-based superconductors. . . . .	20
1-6 STM set-up and working. . . . .	22
1-7 Zn impurity-induced resonance states in $\text{Bi}_2\text{Sr}_2\text{CaCu}_2\text{O}_{8+\delta}$ . . . . .	23
3-1 STM topography of FeSe thin film. . . . .	36
3-2 FeSe Wannier orbitals. . . . .	37
3-3 Properties of the normal state of FeSe. . . . .	39
3-4 Properties of the homogeneous superconducting state of FeSe. . . . .	43
3-5 Lattice LDOS in the vicinity of an impurity. . . . .	46
3-6 Continuum LDOS maps at various biases and heights from Fe-plane. . . . .	47
3-7 Topography of impurity states. . . . .	48
4-1 Cu- $d_{x^2-y^2}$ Wannier function in $\text{Bi}_2\text{Sr}_2\text{CaCu}_2\text{O}_{8+\delta}$ . . . . .	52
4-2 Properties of the normal state of $\text{Bi}_2\text{Sr}_2\text{CaCu}_2\text{O}_{8+\delta}$ . . . . .	53
4-3 Properties of the homogeneous superconducting state of $\text{Bi}_2\text{Sr}_2\text{CaCu}_2\text{O}_{8+\delta}$ . . . . .	55
4-4 $\text{Bi}_2\text{Sr}_2\text{CaCu}_2\text{O}_{8+\delta}$ Wannier function at a height $z \approx 5 \text{ \AA}$ above the BiO plane. . . . .	57
4-5 LDOS spectrum in the vicinity of a Zn impurity in BSCCO. . . . .	59
4-6 LDOS maps at the Zn impurity induced resonant energy. . . . .	60
4-7 LDOS spectrum in the vicinity of a local magnetic impurity. . . . .	62
4-8 LDOS spectrum in the vicinity of an extended magnetic impurity. . . . .	63
4-9 LDOS maps at the magnetic impurity-induced resonant energies. . . . .	64
4-10 QPI patterns obtained from lattice and continuum LDOS. . . . .	66
4-11 QPI Z-maps and $\Lambda$ -maps obtained from lattice and continuum LDOS. . . . .	67

5-1	Peirels distortion in 1D metals. . . . .	71
5-2	Characteristics of the charge order in cuprates. . . . .	72
5-3	Energy per site at various hole dopings for homogeneous superconducting state, APCDW, and nPDW states. . . . .	84
5-4	Characteristic features of the APCDW state. . . . .	86
5-5	Continuum LDOS maps in the APDW state. . . . .	88
5-6	Continuum LDOS, form factors, and spatial phase difference in the APCDW state. . . . .	89
5-7	Characteristic features of the nPDW state. . . . .	91
5-8	Continuum LDOS maps in the nPDW state. . . . .	92
5-9	Continuum LDOS spectrum in the nPDW state. . . . .	93
5-10	Bias dependence of the intra-unit cell form factors in the nPDW state. . . . .	94
5-11	Bias dependence of average spatial phase difference in the nPDW state. . . . .	96
5-12	Importance of the PDW character of the nPDW state. . . . .	97
B-1	Supercell set-up . . . . .	113
C-1	Nodal coordinates . . . . .	118

Abstract of Dissertation Presented to the Graduate School  
of the University of Florida in Partial Fulfillment of the  
Requirements for the Degree of Doctor of Philosophy

THEORETICAL VISUALIZATION OF ATOMIC-SCALE PHENOMENA IN  
INHOMOGENEOUS SUPERCONDUCTORS

By

Peayush K. Choubey

May 2017

Chair: Peter Hirschfeld

Major: Physics

Scanning tunneling microscopy (STM), with its unique capabilities to image the electronic structure of solids with atomic resolution, has been extensively used to study superconductors. The tunneling conductance measured by STM is proportional to the local density of states (LDOS) at the STM tip position and, hence, provides indispensable information about the superconducting gap in the energy spectrum. Many of the unconventional superconductors are layered materials where, generally, the layer exposed to the STM tip is different from the 'active' layer responsible for superconductivity. The intervening layers between STM tip and the active layer can provide indirect tunneling paths and hence significantly alter the conclusions drawn from assuming a direct tunneling. To address this issue, we have developed a novel 'BdG+W' method which combines the solution of the widely used lattice Bogoliubov-de Gennes (BdG) equations and first principles Wannier functions. Here, the BdG equations are solved on a two-dimensional (2D) lattice in the active layer, and the effect of other degrees of freedom are included through Wannier functions, enabling calculation of LDOS at STM tip position with sub-unit cell resolution.

As the first application of the BdG+W method, we study the response of the superconductor FeSe to a single point-like impurity substituting on a Fe site. Using the solution of the 10-Fe-orbital BdG equations in conjunction with the first principles Wannier functions, we show that that the atomic-scale dimer-like states observed in STM

experiments on FeSe and several other Fe-based superconductors can be understood as a consequence of simple defects located on Fe sites due to hybridization with the Se states. Next, we study the effects of Zn and Ni impurities on the local electronic structure in cuprate superconductor  $\text{Bi}_2\text{Sr}_2\text{CaCuO}_8$  (BSCCO). Modeling Zn as a strong on-site potential scatterer, we obtain LDOS maps at a typical STM tip height using BdG+W method showing excellent agreement with the STM measurements, resolving the long-standing 'Zn-paradox'. Moreover, we show that the LDOS obtained using BdG+W framework treating Ni in a simple model of a magnetic impurity shows excellent agreement with the STM results. Finally, we study the charge ordered states in the extended t-J model using a renormalized mean-field theory. We show that the nodal pair density wave state supported by this model has characteristics very similar to that observed in the STM experiments on the underdoped cuprates.

# CHAPTER 1 INTRODUCTION

## 1.1 Historical Background

Superconductivity - characterized by zero resistivity and perfect diamagnetism below a critical temperature ( $T_c$ ) - represents one of the most remarkable manifestations of quantum mechanics at the macroscopic scale. It was discovered by Kamerlingh Onnes in 1911 with the observation of a sudden drop in the resistivity of mercury when it was cooled below 4.2 K [1]. Twenty-two years later, Meissner and Ochsenfeld showed that the superconductor is more than just a perfect conductor by discovering the "Meissner effect", the complete expulsion of magnetic field when a material is cooled below  $T_c$  regardless of its past history [2]. It led the London brothers to propose the existence of a macroscopic quantum-mechanical condensate which carries the supercurrent [3]. In 1950, Ginzburg and Landau introduced an order parameter description of the superconducting condensate and proposed the famous "Ginzburg-Landau (GL)" equation leading to a successful phenomenological description of superconductivity [4] as a macroscopic quantum phenomenon. In the same year, the discovery of the isotope effect- a change in  $T_c$  caused by isotopic substitution of lattice ions- paved the way for the microscopic theory of superconductivity [5, 6]. It showed, for the first time, that the lattice degrees of freedom play important role in the superconductivity of simple materials. Soon after, Bardeen and Fröhlich showed that the lattice vibrations can mediate an effective attraction between electrons, even if Coulomb repulsion is taken into account [7–9]. In another important development, Cooper showed that the Fermi sea is unstable against the formation of bound pairs of electrons, called "Cooper pairs", in presence of effective electron-electron attractive interaction, no matter how weak it is [10]. With these two important ingredients, Bardeen, Cooper, and Schrieffer proposed the famous BCS theory in 1957 [11], explaining the microscopic origin of superconductivity for which they were awarded the Nobel prize in 1972. BCS theory explained most of the experimental

observations in elemental superconductors and is regarded as one of the cornerstones of the condensed matter physics.

In the next two decades of the BCS theory, even after intense experimental efforts,  $T_c$  could not be raised beyond 23 K. A major breakthrough was achieved by Bednorz and Müller in 1986 [12]. They discovered superconductivity in doped perovskite  $\text{La}_{2-x}\text{Ba}_x\text{CuO}_4$  with record-breaking  $T_c$  of 35 K; a truly remarkable result given that the undoped compound is an insulator. Within a year, intense experimental efforts across many laboratories resulted into discovery of similar compounds with increasing  $T_c$  such as  $\text{YBa}_2\text{Cu}_3\text{O}_{7-\delta}$  ( $T_c = 93$  K),  $\text{Ba}_2\text{Sr}_2\text{CaCu}_2\text{O}_{8+\delta}$  ( $T_c = 85$  K), and  $\text{TlBa}_2\text{Ca}_2\text{CuO}_{8+\delta}$  ( $T_c = 110$  K). These compounds have  $\text{CuO}_2$  layers as a common structural unit and hence they are called cuprates. In section 1.3, we review some of the important properties of these materials. The second class of high- $T_c$  superconductors was discovered in iron-based materials by Hosono and co-workers who reported 26K superconductivity in fluorine-doped  $\text{LaFeAsO}$  in early 2008 [13]. Soon after that, highest  $T_c$  in this class of materials reached to 55 K by the discovery of  $\text{SmO}_{1-x}\text{F}_x\text{FeAs}$  [14] and 65-70 K in monolayer  $\text{FeSe}$  grown on  $\text{SrTiO}_3$  substrate [15]. In section 1.3, we review some of the important properties of these Fe-based materials. Figure 1-1 summarizes the history of high-temperature superconductivity.

## 1.2 BCS Theory

Here, we will review some main results of the BCS theory. Detailed discussions and derivations can be found in many excellent textbooks [17–19]. BCS considered the following pairing Hamiltonian as a minimal model to produce a superconducting ground state:

$$H_{\text{SC}} = \sum_{\mathbf{k}\sigma} \xi_{\mathbf{k}} c_{\mathbf{k}\sigma}^\dagger c_{\mathbf{k}\sigma} + \sum_{\mathbf{k}\mathbf{k}'} V_{\mathbf{k}\mathbf{k}'} c_{\mathbf{k}'\uparrow}^\dagger c_{-\mathbf{k}'\downarrow}^\dagger c_{-\mathbf{k}\downarrow} c_{\mathbf{k}\uparrow} \quad (1-1)$$

Here,  $c_{\mathbf{k}\sigma}^\dagger$  creates an electron with momentum  $\mathbf{k}$  and spin  $\sigma = \uparrow, \downarrow$ . The first term in the above Hamiltonian represents the kinetic energy of electrons, with  $\xi_{\mathbf{k}}$  being the single-particle energy relative to the Fermi energy. The second term represents an

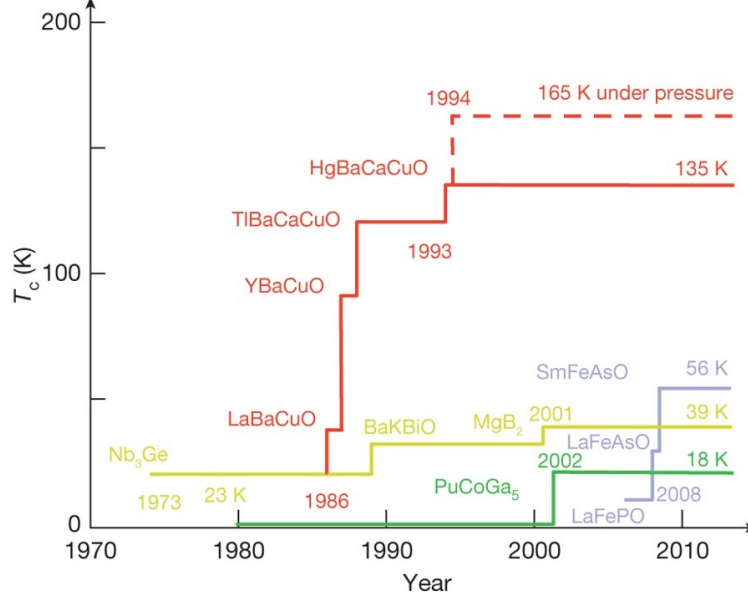


Figure 1-1. Superconducting transition temperature ( $T_c$ ) versus year of discovery for various superconductors. Reprinted by permission from Macmillan Publishers Ltd: Nature [16], copyright 2015.

attractive interaction which scatters a pair of electrons in state  $(\mathbf{k} \uparrow, -\mathbf{k} \downarrow)$  to state  $(\mathbf{k}' \uparrow, -\mathbf{k}' \downarrow)$  with an amplitude  $V_{\mathbf{k}\mathbf{k}'} < 0$ . This Hamiltonian can be studied by a variety of approaches such as variational method, mean-field decomposition, and Greens function methods. Originally, BCS used the variational approach, and hypothesized the following trial wavefunction

$$|\Psi\rangle = \prod_{\mathbf{k}} \left( u_{\mathbf{k}} + v_{\mathbf{k}} c_{\mathbf{k}\uparrow}^\dagger c_{-\mathbf{k}\downarrow}^\dagger \right) |0\rangle \quad (1-2)$$

Here,  $|0\rangle$  represents the vacuum state.  $u_{\mathbf{k}}$  and  $v_{\mathbf{k}}$  are the variational parameters with respect to which the ground state energy  $E = \langle \Psi | H_{SC} | \Psi \rangle$  has to be minimized under the constraint  $|u_{\mathbf{k}}|^2 + |v_{\mathbf{k}}|^2 = 1$  as required for the normalization. The BCS wavefunction represents a coherent superposition of Cooper pairs with  $|v_{\mathbf{k}}|^2$  ( $|u_{\mathbf{k}}|^2$ ) being the probability of pair state  $|\mathbf{k} \uparrow, -\mathbf{k} \downarrow\rangle$  to be occupied (empty).

One of the key quantities in the BCS theory is the superconducting gap parameter  $\Delta_{\mathbf{k}}$ , defined as:

$$\Delta_{\mathbf{k}} = \sum_{\mathbf{k}'} V_{\mathbf{k}\mathbf{k}'} \langle c_{-\mathbf{k}'\downarrow} c_{\mathbf{k}'\uparrow} \rangle = - \sum_{\mathbf{k}'} V_{\mathbf{k}\mathbf{k}'} u_{\mathbf{k}'} v_{\mathbf{k}'} \quad (1-3)$$

The excitation energy of a quasi-particle with momentum  $\hbar\mathbf{k}$  in the superconducting state depends on  $\Delta_{\mathbf{k}}$ , and is given by

$$E_{\mathbf{k}} = \sqrt{\xi_{\mathbf{k}}^2 + |\Delta_{\mathbf{k}}|^2} \quad (1-4)$$

It shows that an energy gap is opened at the Fermi level ( $\xi_{\mathbf{k}} = 0$ ) and that the minimum energy to excite a quasi-particle with wavevector  $\mathbf{k}$  is  $|\Delta_{\mathbf{k}}|$ . The superconducting gap parameter depends on the pair potential  $V_{\mathbf{k}\mathbf{k}'}$  and is obtained by solving the so called "BCS gap equation"

$$\Delta_{\mathbf{k}} = - \sum_{\mathbf{k}'} V_{\mathbf{k}\mathbf{k}'} \frac{\Delta_{\mathbf{k}'}}{2E_{\mathbf{k}'}} \tanh \frac{\beta E_{\mathbf{k}'}}{2} \quad (1-5)$$

where  $\beta = 1/k_B T$ , with  $k_B$  and  $T$  being the Boltzmann constant and temperature, respectively. It is a highly non-linear integral equation and has a trivial solution  $\Delta_{\mathbf{k}} = 0$  representing the high-temperature normal state. At sufficiently low temperatures, a non-trivial solution can exist, implying a superconducting state.

Equation 1-5 is hard to solve for a general  $V_{\mathbf{k}\mathbf{k}'}$ . BCS used a simplified model of the phonon-mediated attractive interaction to get a closed-form solution of the gap equation:

$$V_{\mathbf{k}\mathbf{k}'} = \begin{cases} -V, & \text{if } |\xi_{\mathbf{k}}|, |\xi_{\mathbf{k}'}| \leq \hbar\omega_D \\ 0, & \text{otherwise} \end{cases} \quad (1-6)$$

Where  $V$  is a positive constant and  $\omega_D$  refers to the Debye frequency. Using this simplified model in Equation 1-5, we find that the superconducting gap is constant for  $\mathbf{k}$  within an energy  $\hbar\omega_D$  of the Fermi energy, and its zero-temperature value, in the weak-coupling limit, is given by

$$\Delta(0) = 2\hbar\omega_D \exp \left[ \frac{-1}{N_F V} \right] \quad (1-7)$$

Here,  $N_F$  represents the electronic density of states (DOS) at the Fermi level and  $N_F V \ll 1$ . Taking the limit  $\Delta(T) \rightarrow 0$  in Equation 1-5 yields  $T_c$ :

$$k_B T_c = 1.13 \hbar\omega_D \exp \left[ \frac{-1}{N_F V} \right] \quad (1-8)$$

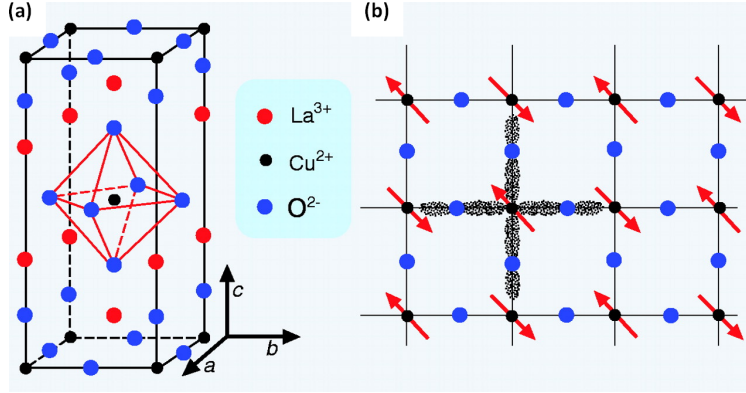


Figure 1-2. (a) Crystal structure of stoichiometric cuprate  $\text{La}_2\text{CuO}_4$  (b) Schematic of  $\text{CuO}_2$  plane. Red arrows indicate a possible alignment of spins on Cu ions in the antiferromagnetic ground state of  $\text{La}_2\text{CuO}_4$ . The shaded region indicates the hybridization of  $\text{Cu}-d_{x^2-y^2}$ ,  $\text{O}-p_x$  and  $\text{O}-p_y$  orbitals which leads to an effective 1-band system in cuprates. Both figures are from [22]. Reprinted with permission from AAAS.

The universal ratio  $\Delta(0)/k_B T_c = 1.764$  predicted by BCS theory (compare Equations 1-7 and 1-8) has been found to be in good agreement with the experiments [20, 21].

### 1.3 Overview of Cuprate Superconductors

Cuprates contain  $\text{CuO}_2$  layers as a common structural unit, generally separated by insulating spacer layers. As an example, Figure 1-2(a) shows the crystal structure of stoichiometric cuprate  $\text{La}_2\text{CuO}_4$  which is the "parent compound" of the first high- $T_c$  cuprate family  $\text{La}_{2-x}\text{Sr}_x\text{CuO}_4$  also known as LSCO. In the  $\text{CuO}_2$  plane Cu form a square lattice and has four-fold coordination with O atoms as shown in Figure 1-2(b). It was realized early by Anderson that the  $\text{CuO}_2$  plane plays the most important role in the physics of cuprates. Spacer layers are thought to act as the charge reservoirs which dope the  $\text{CuO}_2$  plane.

In the parent compounds, Cu has a valence state  $\text{Cu}^{2+}$  and electronic configuration  $3d^9$  leading to an occupancy of one electron per  $\text{CuO}_2$  unit cell. For such a half-filled system, band theory predicts a metallic state. However, cuprate parent compounds are "Mott" insulators with a charge gap of order 2 eV. In the half-filled configuration, any hopping of an electron will produce a doubly occupied site. Due to strong Coulomb

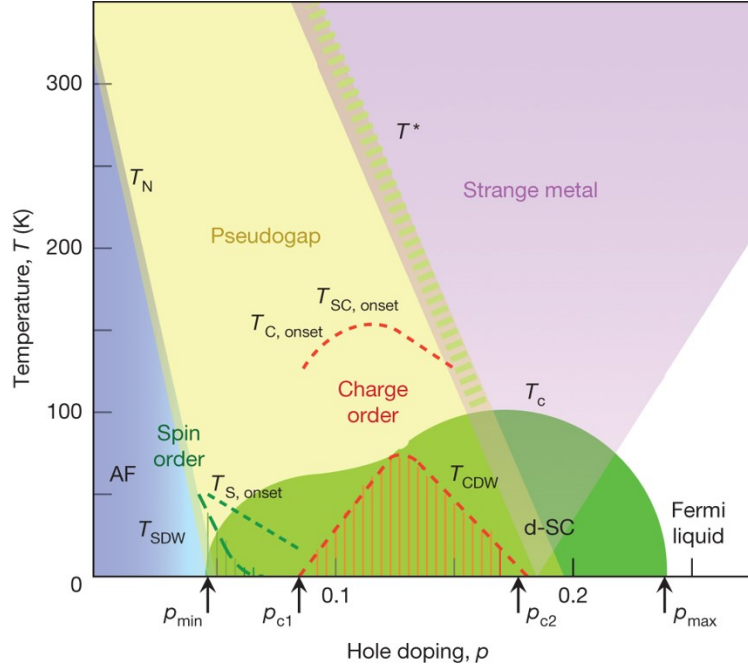


Figure 1-3. Schematic phase diagram of cuprates as a function of temperature and hole doping.  $T_N$ ,  $T_{SDW}$ , and  $T_{CDW}$  represents the temperatures at which antiferromagnetic, spin-density wave and charge density wave orders set-in.  $T^*$  represents the crossover temperature between strange metal and pseudogap phases.  $T_{c, onset}$ ,  $T_{SDW, onset}$ , and  $T_{SC, onset}$  indicates the temperature at which fluctuations of charge, spin and superconducting order becomes apparent. Quantum critical points for superconducting and charge order are indicated by arrows. Reprinted by permission from Macmillan Publishers Ltd: Nature [16], copyright 2015.

repulsion, the energy cost ( $U$ ) of such a double occupancy is huge compared to the hopping energy  $t$ , prohibiting the hopping of electrons and thus blocking the charge conduction. Although charge fluctuations are prohibited in the Mott phase, spins are free to have dynamics. In fact, the virtual hopping of electrons produces an effective antiferromagnetic coupling ( $J$ ) between spins, a mechanism known as "super-exchange" [23]. This leads to a simple antiferromagnetic ordering of spins as shown in Figure 1-2(b).

Doping the parent compound with holes, i.e. lowering the number of electrons per unit cell from 1 to  $1 - p$ , where  $p$  denotes the doping level, produces an incredibly rich phase diagram as shown in Figure 1-3 taken from Ref. [16]. With increasing  $p$ , the Neel temperature ( $T_N$ ) decreases sharply and at a critical doping  $p = p_c$  ( $\approx 0.02$  in LSCO

[22]) antiferromagnetic order vanishes. Almost immediately afterwards, superconductivity sets in at  $p = p_{min}$  ( $\approx 0.06$  in LSCO [24]). With increasing doping, the  $T_c$  line traces a dome-like shape. The maximum  $T_c$  occurs at the "optimal" doping  $p = p_{opt}$  dividing the phase diagram by convention into two regions namely underdoped ( $p < p_{opt}$ ) and overdoped ( $p > p_{opt}$ ). It has been established by phase-sensitive experiments [25, 26] that the superconducting gap ( $\Delta_{\mathbf{k}}$ ) in cuprates has a  $d$ -wave symmetry, meaning that the gap changes sign under  $90^\circ$  rotation. Furthermore, angle-resolved photoemission spectroscopy (ARPES) experiments [27] reveal that the gap has  $d_{x^2-y^2}$  structure which, in its simplest form, can be expressed as  $\Delta_{\mathbf{k}} \sim (\cos k_x - \cos k_y)$ . The gap magnitude vanishes at four points on the Fermi surface near  $(\pm\pi/2, \pm\pi/2)$  called nodes, and achieves a maximum on eight points near  $(\pm\pi, 0)$  and  $(0, \pm\pi)$  called anti-nodes. The presence of low energy "nodal" excitations leads to very different temperature dependence of thermodynamic and transport observables, such as specific heat, thermal conductivity and superfluid density, compared to the fully-gaped conventional superconductors [28].

On the overdoped side, many of the properties of the superconducting state can be phenomenologically explained in a simple BCS theory framework with a  $d_{x^2-y^2}$  gap. This approach is substantiated by the ARPES observation of well defined quasiparticles and a hole-like Fermi surface, similar to the band theory predictions, suggesting a Fermi liquid-like normal state in overdoped cuprates [27]. We use this framework in Chapter 4 to study the effects of magnetic and non-magnetic impurities in over-to-optimally doped cuprates.

The underdoped side, on the other hand, is considered to be much more strongly correlated due to its proximity to the Mott insulator phase, and not suitable for a description in terms of a simple BCS framework. In this context, a simple but extensively studied model which captures the idea of superconductivity originating from "doping a Mott insulator" [24] is the  $t - J$  model [29]. As the strong coupling limit ( $U \rightarrow \infty$ ) of the Hubbard model, it excludes all configurations of states with any double occupancy

of sites. Although an exact solution is not known yet, various approximate treatments such as variational Monte-Carlo methods [30], Gutzwiller mean-field theory [30, 31], and slave-boson approach [24, 32, 33] have found a superconducting ground state with  $d_{x^2-y^2}$  symmetry. In Chapter 5, we use an extended version of this model, including next-nearest hopping  $t'$ , to study the coexistence phase of superconductivity and charge order which has been observed across the cuprate family in the underdoped region (see Figure 1-3). Various experimental probes such as nuclear magnetic resonance (NMR) [34], scanning tunneling microscopy (STM) [35], and resonant X-ray scattering [36] reveal that the charge order is short-range, uni-directional, and incommensurate with a  $d$ -wave type intra-unit cell symmetry. Moreover, it generally does not accompany a magnetic order [36] and is thought to be distinct from the "stripe order", which consists of combined unidirectional modulating magnetic and charge order, observed primarily in  $\text{La}_{2-x}\text{Ba}_x\text{CuO}_4$  near  $p = 1/8$  doping [37].

By crossing the  $T_c$  line in the underdoped regime one enters into the "psuedogap" region of the phase diagram. The psuedogap is characterized by the suppression of low energy single-particle spectral weight and is observed through various experimental means including, but not limited to, NMR, ARPES and specific heat measurements (see [24, 27, 38] for review). In particular, ARPES finds opening of an incoherent gap in the anti-nodal region of Brillouin zone and disconnected arc-like features, called "Fermi arcs", in the nodal region [27]. The crossover line denoted by  $T^*$  in Figure 1-3 separates the psuedogap regime from another exotic regime, namely the "strange metal" which is characterized by lack of the well-defined quasiparticles and resistivity varying linearly with temperature. These two regimes constitute least understood and most contentious part of the cuprate phase diagram.

#### 1.4 Overview of Iron-Based Superconductors

Iron based superconductors (FeSCs) are divided into two categories: Fe-pnictides (e.g.  $\text{LiFeAs}$ ) and Fe-chalcogenides (e.g.  $\text{FeSe}$ ). Figure 1-4(a) shows crystal structure of

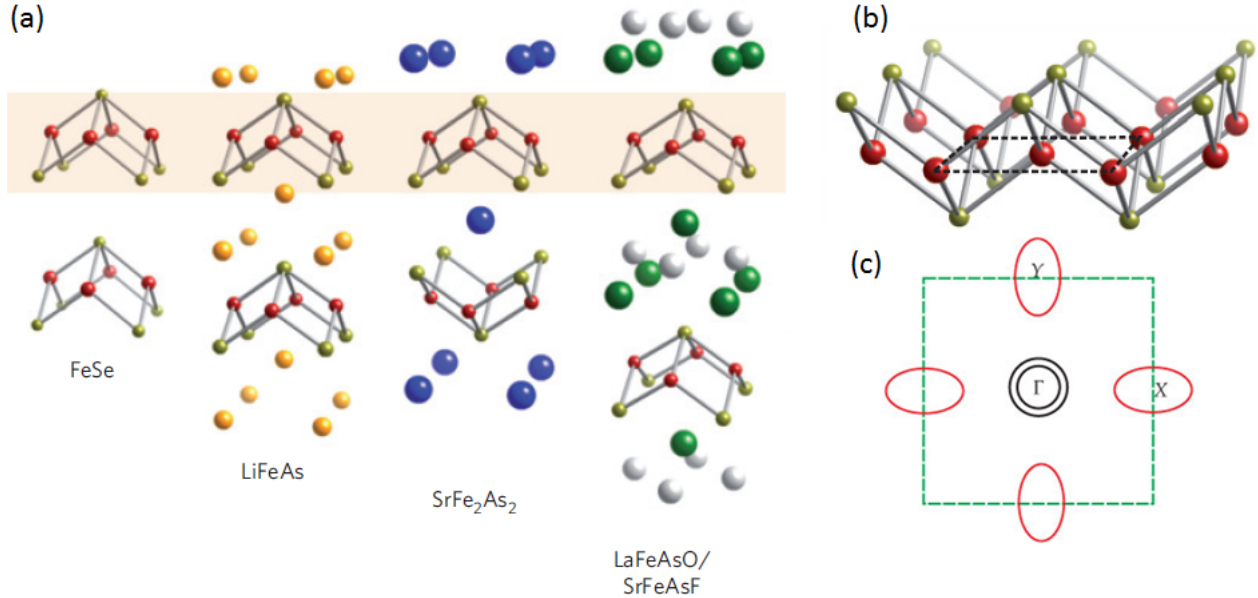


Figure 1-4. (a) Crystal structure of representative members of the various families of iron-based superconductors. Fe atoms are shown in red and pnictogen/chalcogen atoms are shown in gold. (b) Schematic of iron-pnictogen/iron-chalcogen layer. Here, Fe atoms, shown in red, form a square lattice and pnictogen/chalcogen atoms, shown in gold, are located above and below the Fe-plane in an alternating manner. (a) and (b) are reprinted by permission from Macmillan Publishers Ltd: Nature [39], copyright 2010. (c) A generic Fermi surface of iron-based superconductors in normal state. Green dotted lines denote the boundary of the 1-Fe Brillouin zone.  $\Gamma$  represents the Brillouin zone center.  $X$  and  $Y$  represent the Brillouin zone edge centers. Reproduced from [40], with the permission of the American Institute of Physics.

representative members of the four most studied families of iron based superconductors (FeSCs) namely 11, 111, 122 and 1111, reflecting the formulas of their stoichiometric parent compounds. All these structures are characterized by a common FePn or FeCh layers, Pn (Ch) being the pnictogen (chalcogen) elements such as As (Se), separated by spacer layers. Like CuO<sub>2</sub> layers in cuprates, FePn/FeCh layers play the most important role in the physics of FeSCs. The spacer layer primarily acts as a reservoir of charge carriers, as in cuprates, or a source of chemical pressure. As shown in Figure 1-4(b), Fe forms a square lattice and Pn or Ch ions are located above and below the center of squares in alternating fashion. Apart from these bulk materials, monolayers of FeSe,

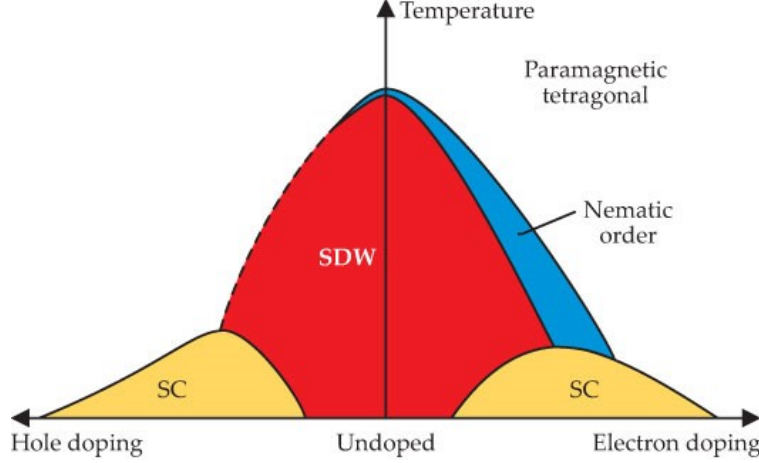


Figure 1-5. Schematic phase diagram of iron-based superconductors as a function of temperature and doping. SDW and SC refers to spin density wave and superconducting phases, respectively. Reproduced from [40], with the permission of the American Institute of Physics.

epitaxially grown on strontium titanate (STO) substrate, have attracted enormous attention recently [41] owing to their high  $T_c$  (110K from resistive measurements [42] and 70K from ARPES measurements [43]) which is an order of magnitude larger than the bulk FeSe ( $T_c \approx 8\text{K}$ ).

In parent compounds, Fe has a valence state  $\text{Fe}^{2+}$  and electronic configuration  $3d^6$ . Unlike cuprates, where only one  $d$ -orbital ( $d_{x^2-y^2}$ ) contributes to the Fermi surface, first-principles band structure calculations [44] and ARPES results [45] show that all five  $d$ -orbitals contribute to the Fermi surface of FeSC parent compounds with  $d_{xy}$ ,  $d_{xz}$ , and  $d_{yz}$  having the largest weight. Moreover, it is found that the hole-like and electron-like bands cross the Fermi energy near the Brillouin zone center ( $\Gamma$  point) and Brillouin zone boundary ( $X$  and  $Y$  points), leading to a Fermi surface with nearly circular "hole pockets" at the  $\Gamma$  point and elliptical "electron pockets" at the  $X$  and  $Y$  points as shown in Figure 1-4(c). This multi-band nature plays a central role in the physics of FeSCs.

A schematic phase diagram of a representative Fe pnictide as a function of electron and hole doping is shown Figure 1-5. The high temperature phase of undoped parent compound is a paramagnetic metal with a tetragonal lattice. Lowering the temperature

results in an almost simultaneous structural and magnetic transition to an orthorhombic spin density wave (SDW) phase [46]. In this phase, generally, ordered spins form a "stripe" pattern, characterized by ferromagnetic order in one direction and antiferromagnetic (Neel-type) order in other. In doped compounds, the structural transition precedes the magnetic transition i.e.  $T_s > T_N$ , where  $T_s$  and  $T_N$  represents structural and magnetic transition temperatures, respectively. The blue region between  $T_s$  and  $T_N$  phase lines as shown in Figure 1-5 is called the "Nematic" phase, borrowing the terminology from liquid-crystals where it corresponds to a phase with broken rotational symmetry but preserved translational symmetry. The nematic phase in Fe-based materials is believed to have an electronic origin [47], as the large anisotropy observed in various experiments, such as in-plane resistivity measurements [48], STM [49], ARPES [50], and torque magnetometry [51], can not be explained by the very small orthorhombic lattice distortion.

At low temperatures, doping the parent compound with electrons or holes typically leads to the appearance of the superconducting phase. The  $T_c$  line traces an asymmetric dome-like shape with maximum  $T_c$  taking values as large as 57K in 1111 materials [52]. NMR experiments on many FeSCs [53] strongly indicate that the superconducting state is spin singlet, making a case for even parity superconducting gap such as  $s$ -wave and  $d$ -wave. However, unlike cuprates, there is no definitive experimental evidence of a particular gap symmetry in FeSCs. At moderate doping levels, most of the experiments point towards a multi-band  $s$ -wave type gap with two possible scenarios, namely  $s_{++}$  [54] and  $s_{\pm}$  [55]. In  $s_{++}$  ( $s_{\pm}$ ) pairing the superconducting gap has same (opposite) sign on electron and hole pockets. Although, there is no "smoking gun" evidence to favor one over the other,  $s_{\pm}$  is widely believed to be the pairing symmetry in most of the weak-to-moderately doped FeSCs. In Chapter 3, we study the impurity bound states in the superconducting FeSe with  $s_{\pm}$  pairing.

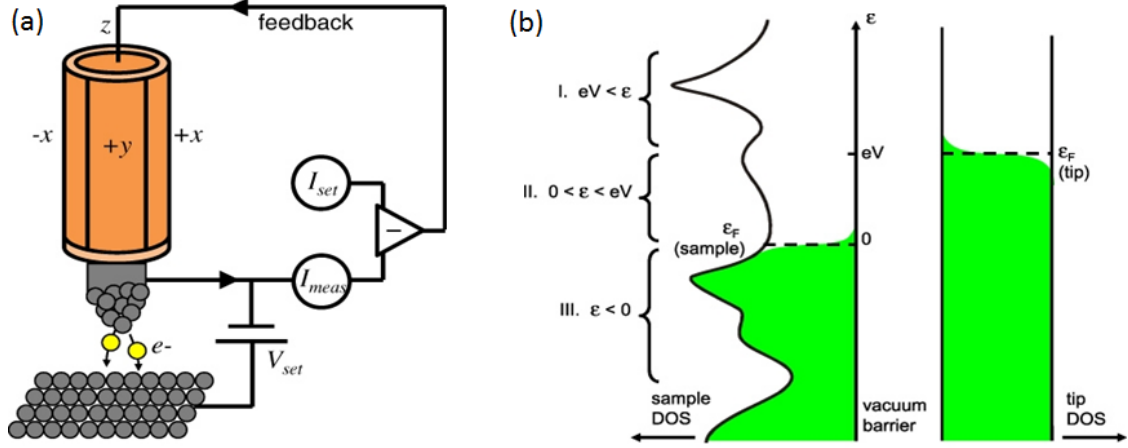


Figure 1-6. (a) Schematic of a scanning tunneling microscope. A bias voltage  $V$  is applied between a sharp metallic tip and the sample, which results in a measurable tunneling current. (b) Schematic of tip-sample tunneling. When a positive bias is applied on the sample, its Fermi level lowers by an amount  $eV$  compared to the tip Fermi level. Electrons tunnel primarily from filled states in the tip to empty states in the sample. Reprinted from [56]. Copyright IOP Publishing. Reproduced with permission.

### 1.5 STM Studies of Superconductors

Scanning tunneling microscopy (STM), with its unique capabilities to image the electronic structure of solids with atomic resolution, has been extensively used to study superconductors [56–59]. The STM apparatus consists of an atomically thin metallic tip separated from a conducting sample surface through a vacuum barrier as shown in Figure 1-6(a). The position of the tip ( $\mathbf{r}$ ) can be controlled with a sub-Å resolution using piezoelectric actuators. Applying a bias voltage between an appropriately placed tip and the sample results in a measurable tunneling current through the vacuum barrier. Under various justifiable assumptions such as low temperature, energy-independent tunneling matrix element, and featureless density of states in the tip material, differential tunneling conductance turns out to be proportional to the local density of states (LDOS) of the sample [56, 57],

$$\frac{dI}{dV} \propto \rho_s(\mathbf{r}, eV) \quad (1-9)$$

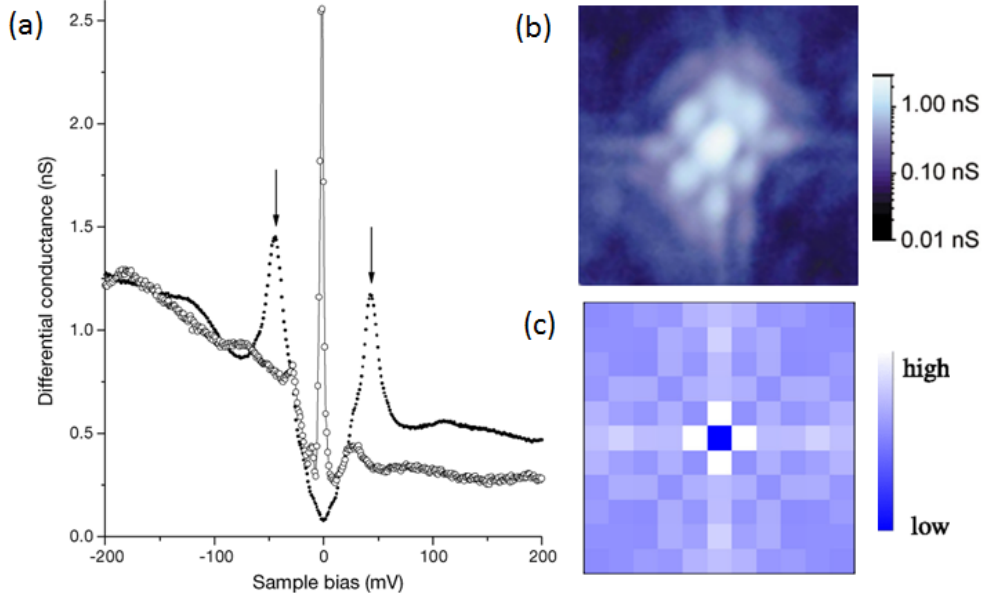


Figure 1-7. (a) Comparison of tunneling conductance spectra directly above Zn impurity site and at a site far away from impurity in superconducting  $\text{Bi}_2\text{Sr}_2\text{CaCu}_2\text{O}_{8+\delta}$  doped with Zn. (b) Spatial conductance map around Zn impurity at resonant energy ( $-1.2$  meV) showing intensity maximum right above the impurity site. Both figures are reprinted by permission from Macmillan Publishers Ltd: Nature [60], copyright 2000. (c) Local density of states around impurity site at the resonant energy resulting from a simple theoretical model of a strong non-magnetic impurity in a  $d$ -wave superconductor.

Here,  $I$  is the tunneling current,  $V$  is the applied bias,  $\rho_s$  is the sample LDOS and  $e$  is the electronic charge. Thus, conductance measured the tip position  $\mathbf{r}$  and a bias voltage  $V$  is equivalent to the sample's LDOS at the spatial position  $\mathbf{r}$  and energy  $\omega = eV$ . The sub-Å resolution spectroscopic imaging of LDOS provides indispensable information about the superconducting gap. Further information about the nature of superconductivity can be obtained by studying the atomic-scale electronic structures around impurities in superconductors. Finally, momentum resolved details of the Fermi surface and superconducting gap can be obtained using 'quasi-particle interference (QPI)' technique which essentially involves the Fourier transform of the conductance maps.

In layered superconductors such as cuprates and FeSCs, generally, the layer exposed to the STM tip where material cleaves turns out to be different from the 'active' layer

responsible for the superconductivity ( $\text{CuO}_2$  layer in cuprates and Fe layer in FeSCs). In this scenario, a direct comparison of STM results with theoretical calculations which only take the active layer's degrees of freedom into account can lead to misinterpretation of data. This is nicely illustrated by the famous "Zn-paradox" in the cuprate compound BSCCO which cleaves at the BiO plane, two layers above the  $\text{CuO}_2$  plane. STM conductance spectra taken over a Zn impurity in superconducting BSCCO [60] reveal that Zn induces an in-gap bound state as shown in Figure 1-7(a). The conductance map taken at the bound state energy ( $-1.2$  meV) shows intensity maxima at the Zn site (Figure 1-7(b)) whereas theoretical calculations of impurity-induced states in a  $d$ -wave superconductor (based on a simple, on-site nonmagnetic potential) predict LDOS minima at the Zn site [61]. It was proposed that this discrepancy can be reconciled if the BiO layer is assumed to act as a "filter" providing a non-trivial tunneling path from STM tip to Zn atom [62].

To address the aforementioned issue, I have developed a novel 'BdG+W' method which combines the solution of Bogoliubov-de Gennes (BdG) equations, widely used to study inhomogenous superconductivity, and first principles Wannier functions to yield LDOS at STM tip position with sub-Å resolution. Here, the BdG equations are solved self-consistently on a two-dimensional lattice in the active layer, and the effect of atoms in other layers is included through Wannier functions defined in 3D continuum space. In Chapter 2, I describe the mathematical framework behind the 'BdG+W' method. As the first application, in Chapter 3, I study the effects of a single non-magnetic impurity in the superconducting FeSe, and show that the geometrical dimer states observed in STM experiments [63] can be understood as a consequence of simple defects located on Fe sites due to hybridization with the Se state. In Chapter 4, I compute the impurity induced resonant LDOS and QPI patterns, within the BdG+W framework, in superconducting BSCCO doped with Zn and Ni impurities and show that the results are in excellent agreement with the STM experiments [60, 64]. In Chapter 5, using renormalized

mean-field theory and Wannier function based analysis, I show that the extended  $t - J$  model supports incommensurate charge ordered states which display characteristics very similar to the charge ordered states observed through STM experiments [65, 66] in underdoped cuprates. Finally, in Chapter 6, I present the summary and conclusions of my dissertation work.

## CHAPTER 2 BOGOLIUBOV-DE GENNES-WANNIER APPROACH

In this chapter, I will discuss the mathematical formulation behind the BdG+W scheme introduced in Section 1.5. Some of the material presented here is based on a published paper [67]. All the published contents (excerpts and figures) are reprinted with permission from Peayush Choubey, T. Berlijn, A. Kreisel, C. Cao, and P. J. Hirschfeld, *Phys. Rev. B* **90**, 134520 (2014), copyright 2014 by the American Physical Society.

### 2.1 Impurities in Superconductors

Studying controlled disorder in a correlated system can provide important insights about its ground state [68]. Effects of disorder in conventional s-wave superconductors, to a great extent, are encapsulated in "Anderson's theorem" [69] and the Abrikosov-Gorkov (AG) theory [70]. The former states that the non-magnetic impurities do not affect  $T_c$  or the superconducting gap due to time-reversal invariance. Magnetic impurities, on the other hand, break time-reversal symmetry and lead to the suppression of  $T_c$ , and the rate of suppression is described by the AG theory for weak scatterers. For stronger potentials, impurity-induced in-gap bound states are created, often referred as the Yu-Shiba-Rusinov states [71–73]. Anderson's theorem does not apply, however, if the superconducting gap has a strong momentum dependence, which is often the case with the unconventional superconductors. In such a scenario, even non-magnetic impurities can suppress  $T_c$  and produce in-gap states. Thus, an experimental observation of  $T_c$  suppression and the presence of in-gap states (or its indirect manifestation) can be an indication of unconventional pairing.

Earlier studies of disorder effects were mainly focused on the bulk properties of superconductors [74] such as  $T_c$ , penetration depth, specific heat and planar tunneling. In recent times, however, the focus has shifted towards local studies of impurity effects [56, 75] mostly owing to rapid technological advancements in STM techniques. The first observation of the in-gap bound states localized around a magnetic impurity in a

conventional superconductor was reported by Yazdani et al. in 1997 [76]. Subsequently, detection of the virtual bound states induced by a non-magnetic impurity (Zn) [60] and a magnetic impurity (Ni) [64] in the cuprate compound  $\text{Bi}_2\text{Sr}_2\text{CaCu}_2\text{O}_{8+\delta}$ , confirmed the earlier theoretical predictions [61] of such states in a  $d$ -wave superconductor. The in-gap bound states observed in many bulk FeSCs [63, 77–79] have indicated, although not conclusively, that a sign changing  $s_{\pm}$  is the more likely pairing symmetry compared to the non-sign changing  $s_{++}$ . More recently, the absence (presence) of bound states induced by non-magnetic (magnetic) impurities in the monolayer FeSe grown on STO substrate has been taken as evidence that the pairing state in this system should be isotropic  $s_{++}$ -wave [80]. This is not necessarily correct, however, if the pairing involves states away from the Fermi level [81].

Here, we will present a simple scheme to study the effects of an impurity in a superconductor in the context of STM experiments. We assume that a BCS-like mean-field description, with proper gap symmetry, can describe the superconducting state. Although such a description neglects correlation effects or treats them at a very crude level (e.g. through an overall band renormalization), it has been used successfully to capture qualitative aspects of the impurity effects in superconductors [75]. Furthermore, the normal state of a material under study is assumed to be well described by a tight-binding model derived from the density functional theory (DFT) calculations. This is justified in case of overdoped cuprates and many FeSCs where ARPES determined Fermi surface displays strong similarity with the corresponding DFT results [27, 45]. For strongly-correlated materials such as optimal-to-underdoped cuprates, it should still be applicable for symmetry-related questions.

## 2.2 Mean-Field Theory

### 2.2.1 Hamiltonian

The simplest Hamiltonian describing effects of impurities in a superconductor consists of three terms, namely a kinetic energy term  $H_0$  describing the non-interacting electrons in

the normal state, a BCS type pairing interaction term  $H_{\text{BCS}}$  describing superconductivity, and an impurity term  $H_{\text{imp}}$ .

$$H = H_0 + H_{\text{BCS}} + H_{\text{imp}}, \quad (2-1)$$

To express the Hamiltonian in a tight-binding model, we first construct a single particle basis of Wannier functions  $w_{i\mu}$  using the DFT wave functions. Here,  $i$  represents an unit cell with the lattice vector  $\mathbf{R}_i$  and  $\mu$  labels the orbital degrees of freedom within the unit cell. Subsequently, hopping parameters are obtained leading to the tight-binding model for the normal state,

$$H_0 = \sum_{ij,\mu\nu,\sigma} t_{ij}^{\mu\nu} c_{i\mu\sigma}^\dagger c_{j\nu\sigma} - \mu_0 \sum_{i,\mu,\sigma} c_{i\mu\sigma}^\dagger c_{i\mu\sigma}. \quad (2-2)$$

Here,  $c_{i\mu\sigma}^\dagger$  ( $c_{i\mu\sigma}$ ) creates (destroys) an electron with spin  $\sigma$  in the Wannier orbital  $\mu$  located in the unit cell  $i$ .  $t_{ij}^{\mu\nu}$  is the amplitude of hopping from the unit cell  $i$  and orbital  $\mu$  to the unit cell  $j$  and orbital  $\nu$ . The average electron filling can be set by tuning the chemical potential  $\mu_0$ . Often the Wannier function information is discarded after constructing the tight-binding model, but in our formalism it plays a crucial role as we will show in Section [2.3.2](#).

The superconducting state is accounted for via a BCS-like pairing term as

$$H_{\text{BCS}} = - \sum_{ij,\mu\nu} V_{ij}^{\mu\nu} c_{i\mu\uparrow}^\dagger c_{j\nu\downarrow}^\dagger c_{j\nu\downarrow} c_{i\mu\uparrow}, \quad (2-3)$$

where  $V_{ij}^{\mu\nu} > 0$  is the real-space pair potential between orbital  $\mu$  in the unit cell  $i$  and orbital  $\nu$  in the unit cell  $j$ .  $V_{ij}^{\mu\nu}$  can be either put in "by hand" to yield a particular gap magnitude and symmetry, or it can be determined from a microscopic theory of pairing. For example, in Chapter [3](#) we use pair potentials determined from a spin fluctuation theory of pairing in FeSCs, and in Chapter [4](#) we put it in "by hand", choosing a non-zero value only for the nearest-neighbor interaction, to yield a  $d$ -wave gap with the experimentally observed magnitude.

Defects in a material can be of many types such as twin boundaries, grain boundaries, interstitial atoms, and substitutional atoms. Here, we consider the simplest kind of defect: substitutional impurity atoms. Impurity atoms interact with the conduction electrons through the screened Coulomb potential which, in the limit of perfect screening, can be accounted for via the following Hamiltonian,

$$H_{\text{imp}} = \sum_{\mu\sigma} V_{\text{imp}} c_{i^*\mu\sigma}^\dagger c_{i^*\mu\sigma}, \quad (2-4)$$

where,  $i^*$  is the impurity unit cell and  $V_{\text{imp}}$  is the impurity potential taken to be proportional to the identity matrix in orbital space for the sake of simplicity. This model can be easily generalized to include an extended range potential, orbital dependence, as well as magnetic scattering. We will return to the latter in Section 4.5.

### 2.2.2 BdG Equations

To diagonalize the Hamiltonian  $H$  (Equation 2-1), we use the mean-field approximation and decompose the quartic operator in Equation 2-3 into two bilinear ones, namely the pair creation operator  $c_{i\mu\uparrow}^\dagger c_{j\nu\downarrow}^\dagger$  and the pair destruction operator  $c_{j\nu\downarrow} c_{i\mu\uparrow}$ . The following is the resulting mean-field Hamiltonian:

$$H_{\text{MF}} = \sum_{ij,\mu\nu,\sigma} t_{ij}^{\mu\nu} c_{i\mu\sigma}^\dagger c_{j\nu\sigma} - \mu_0 \sum_{i,\mu,\sigma} c_{i\mu\sigma}^\dagger c_{i\mu\sigma} - \sum_{ij,\mu\nu} \left[ \Delta_{ij}^{\mu\nu} c_{i\mu\uparrow}^\dagger c_{j\nu\downarrow}^\dagger + \text{H.c.} \right] + \sum_{\mu,\sigma} V_{\text{imp}} c_{i^*\mu\sigma}^\dagger c_{i^*\mu\sigma}, \quad (2-5)$$

where H.c. implies Hermitian conjugate. The superconducting order parameter is given by

$$\Delta_{ij}^{\mu\nu} = V_{ij}^{\mu\nu} \langle c_{j\nu\downarrow} c_{i\mu\uparrow} \rangle. \quad (2-6)$$

The mean field Hamiltonian is quadratic in electron operators and can be diagonalized using the following spin-generalized Bogoliubov transformation,

$$\begin{aligned} c_{i\mu\sigma} &= \sum_n \left[ u_{i\mu\sigma}^n \gamma_{n\sigma} + v_{i\mu\sigma}^{n*} \gamma_{n\bar{\sigma}}^\dagger \right] \\ c_{i\mu\sigma}^\dagger &= \sum_n \left[ u_{i\mu\sigma}^{n*} \gamma_{n\sigma}^\dagger + v_{i\mu\sigma}^n \gamma_{n\bar{\sigma}} \right], \end{aligned} \quad (2-7)$$

where  $\bar{\sigma}$  represents the opposite of spin  $\sigma$ , the  $\gamma$  operators are Bogoliubov quasiparticle fields that satisfy the fermion commutation rules, and the coefficients  $u$  and  $v$  satisfy  $\sum_n |u_{i\mu\sigma}^n|^2 + |v_{i\mu\sigma}^n|^2 = 1$ . When applied to  $H_{\text{MF}}$  (Equation 2-5) the above transformation yields a Hamiltonian diagonal in the  $\gamma$  operators:

$$H_{\text{MF}} = E_0 + \sum_{n\sigma} E_{n\sigma} \gamma_{n\sigma}^\dagger \gamma_{n\sigma} \quad (2-8)$$

Here,  $E_0$  is the ground state energy and  $E_{n\sigma}$  is the quasiparticle energy labeled by indices  $n$  and  $\sigma$ . It should be noted that the sum in Equation 2-8 runs over  $(n, \sigma)$  corresponding to positive eigenvalues ( $E_{n\sigma} > 0$ ). Comparing the commutator  $[H_{\text{MF}}, c_{i\mu\sigma}]$  obtained from the two definitions of mean-field Hamiltonian (Equation 2-5 and Equation 2-8) yields two sets of the BdG equations, related to each other by the particle-hole symmetry (see Appendix A for details). We choose to work with the following set

$$\sum_{j\nu} \begin{pmatrix} \xi_{ij\uparrow}^{\mu\nu} & -\Delta_{ij}^{\mu\nu} \\ -\Delta_{ji}^{\nu\mu*} & -\xi_{ij\downarrow}^{\mu\nu} \end{pmatrix} \begin{pmatrix} u_{j\nu\uparrow}^n \\ v_{j\nu\downarrow}^n \end{pmatrix} = E_{n\uparrow} \begin{pmatrix} u_{i\mu\uparrow}^n \\ v_{i\mu\downarrow}^n \end{pmatrix}. \quad (2-9)$$

Here,  $\xi_{ij\sigma}^{\mu\nu} = t_{ij}^{\mu\nu} - \mu_0 \delta_{ij} \delta_{\mu\nu} - V_{\text{imp}} \delta_{ii^*} \delta_{ij} \delta_{\mu\nu}$  where  $\delta$  represents the Kronecker delta function. Mean-fields such as the orbital-resolved electron density  $n_{i\mu\sigma} = \langle c_{i\mu\sigma}^\dagger c_{i\mu\sigma} \rangle$  and superconducting gap  $\Delta_{ij}^{\mu\nu}$  can be expressed as

$$\begin{aligned} n_{i\mu\uparrow} &= \sum_n |u_{i\mu\uparrow}^n|^2 f(E_{n\uparrow}) \\ n_{i\mu\downarrow} &= \sum_n |v_{i\mu\downarrow}^n|^2 (1 - f(E_{n\uparrow})) \\ \Delta_{ij}^{\mu\nu} &= V_{ij}^{\mu\nu} \sum_n u_{i\mu\uparrow}^n v_{j\nu\downarrow}^{n*} f(E_{n\uparrow}). \end{aligned} \quad (2-10)$$

Here,  $f$  represents the Fermi function and the sum runs over all values of  $n$ . The derivation of Equations 2-9 and 2-10 is straightforward but lengthy, and is provided in Appendix A. The entries of the BdG matrix in Equation 2-9 depend implicitly upon the eigenvalues and eigenvectors through the mean-fields defined in Equation 2-10; thus

the equation must be solved self-consistently. To do so, we first guess the initial values of mean-fields ( $n_\uparrow, n_\downarrow, \Delta$ ) and chemical potential  $\mu_0$ . Then the eigenvalues and eigenvectors of the BdG matrix are obtained, which, in turn, are used to compute mean-fields (Equation 2–10). The process is iterated until the superconducting gap and electron density converge up to a desired accuracy.

### 2.3 Calculation of STM Observables

As explained in Section 1.5, under a wide set of assumptions, the STM tunneling conductance measured at the applied bias  $V = \omega/e$  is proportional to the sample LDOS  $\rho(\mathbf{r}, \omega)$  where  $\mathbf{r}$  is the STM tip position. Thus, to compare with the STM results we must calculate the local density of states in the 3D continuum space. In the following, we first describe the calculation of lattice LDOS, the quantity most often used in literature to compare with the STM observations. Then, we derive the expression for the continuum LDOS which is a more appropriate quantity to compare.

#### 2.3.1 Lattice LDOS

Using the self-consistent solution of the BdG equations (Equation 2–9), lattice Green's functions  $G_{ij\sigma}^{\mu\nu}(\omega)$ , for the propagation between sites  $i, j$  of a real space lattice can be constructed using the following formula (see Appendix A for the derivation)

$$G_{ij\sigma}^{\mu\nu}(\omega) = \sum_{n>0} \left[ \frac{u_{i\mu\sigma}^n u_{j\nu\sigma}^{n*}}{\omega - E_{n\sigma} + i0^+} + \frac{v_{i\mu\sigma}^{n*} v_{j\nu\sigma}^n}{\omega + E_{n\bar{\sigma}} + i0^+} \right], \quad (2-11)$$

where  $0^+$  is the artificial broadening, taken to be much smaller than smallest physical energy in the problem, and  $n > 0$  indicates that the sum is to be performed over eigenstates with positive eigenvalues only. For easier numerical implementation, the above expression can be further simplified as below (see Appendix A for the details)

$$\begin{aligned} G_{ij\uparrow}^{\mu\nu}(\omega) &= \sum_n \frac{u_{i\mu\uparrow}^n u_{j\nu\uparrow}^{n*}}{\omega - E_{n\uparrow} + i0^+} \\ G_{ij\downarrow}^{\mu\nu}(\omega) &= \sum_n \frac{v_{i\mu\downarrow}^{n*} v_{j\nu\downarrow}^n}{\omega + E_{n\uparrow} + i0^+} \end{aligned} \quad (2-12)$$

Here, the sum runs over all values of  $n$ . The orbitally-resolved lattice LDOS can be obtained using the imaginary part of the diagonal lattice Green's functions

$$N_{i\mu\sigma}(\omega) = -\frac{1}{\pi}\text{Im}[G_{ii\sigma}^{\mu\mu}(\omega)] \quad (2-13)$$

where  $\text{Im}$  represents the imaginary part. The total lattice LDOS can be found by summing over all orbitals i.e.  $N_{i\sigma}(\omega) = \sum_{\mu} N_{i\mu\sigma}(\omega)$ .

### 2.3.2 Continuum LDOS

The continuum LDOS is related to the retarded continuum Green's function  $G_{\sigma}(\mathbf{r}, \mathbf{r}'; \omega)$ , defined in the 3D continuum space, as

$$\rho(\mathbf{r}, \omega) = \sum_{\sigma} -\frac{1}{\pi}\text{Im}[G_{\sigma}(\mathbf{r}, \mathbf{r}; \omega)] \quad (2-14)$$

where  $\mathbf{r}$  is a continuum real space position. The continuum Green's function itself can be defined in the time domain in the usual way

$$G_{\sigma}(\mathbf{r}t, \mathbf{r}'t') = -i\theta(t - t')\langle[\Psi_{\sigma}(\mathbf{r}t), \Psi_{\sigma}^{\dagger}(\mathbf{r}'t')]_{+}\rangle, \quad (2-15)$$

where  $\theta$  is the step function,  $[\ ]_{+}$  represents the anti-commutator, and  $\Psi_{\sigma}(\mathbf{r}t)$  denotes the field operator that annihilates an electron with spin  $\sigma$  located at position  $\mathbf{r}$  at time  $t$ .

Now, to transform the single-particle basis from the continuum space  $\mathbf{r}$  to the lattice space  $(i, \mu)$ , we utilize the following representation of the field operators

$$\Psi_{\sigma}(\mathbf{r}t) = \sum_{i, \mu} w_{i\mu}(\mathbf{r})c_{i\mu\sigma}(t), \quad (2-16)$$

where  $w_{i\mu}$  labels the Wannier orbital  $\mu$  located in the unit cell  $i$ . Putting Equation 2-16 in Equation 2-15 yields

$$G_{\sigma}(\mathbf{r}t, \mathbf{r}'t') = \sum_{ij, \mu\nu} G_{ij\sigma}^{\mu\nu}(t, t')w_{i\mu}(\mathbf{r})w_{j\nu}^*(\mathbf{r}'), \quad (2-17)$$

where  $G_{ij\sigma}^{\mu\nu}(t, t') = -i\theta(t - t')\langle[c_{i\mu\sigma}(t), c_{j\nu\sigma}^{\dagger}(t')]_{+}\rangle$  is the lattice Green's function in the time domain. Taking Fourier transform with respect to time on both sides leads to the

frequency domain result

$$G_{\sigma}(\mathbf{r}, \mathbf{r}'; \omega) = \sum_{ij, \mu\nu} G_{ij\sigma}^{\mu\nu}(\omega) w_{i\mu}(\mathbf{r}) w_{j\nu}^*(\mathbf{r}'). \quad (2-18)$$

Thus using Equation 2-18 with  $\mathbf{r}' = \mathbf{r}$  in conjunction with Equation 2-14, the continuum LDOS can be obtained.

Note that the lattice LDOS (Equation 2-13) is completely determined by the local and diagonal (in orbital space) lattice Green's function, whereas the continuum LDOS includes contributions from the non-local and off-diagonal lattice Green's functions  $G_{i \neq j, \sigma}^{\mu \neq \nu}(\omega)$  too. The non-local terms can lead to interference effects, as the sign of their imaginary part is not fixed. Such effects can cause a qualitative change in the spectral features of the lattice LDOS. We discuss this issue in detail in Section 4.3 in the context of overdoped cuprates.

## 2.4 Numerical Implementation

To study the effects of an impurity on the local electronic structure in a superconductor within the BdG+W framework, we first need the DFT derived Wannier functions and tight-binding parameters characterizing the normal state of the material. Wannier functions can be constructed from the DFT wavefunctions, spanning an energy window of several eV, using a projection analysis [82] or a maximal localization routine such as Wannier90 [83]. Then superconductivity is introduced using real-space pair potentials ( $V_{ij}^{\mu\nu}$ ) that can be either obtained from a microscopic theory or can be put in "by hand" to yield an experimentally relevant gap magnitude and symmetry. The impurity potential is usually introduced "by hand", but a more accurate estimate can be obtained from the first-principles calculations.

The next step is to solve the inhomogeneous BdG equations in a self-consistent way. We take a  $N \times N$  square lattice with each lattice site representing a unit cell with  $N_{orb}$  Wannier orbitals, and solve Equation 2-9 in conjunction with Equation 2-10 on this lattice using the following steps:

1. Choose initial guesses for electron density  $n_\sigma$ , superconducting gap  $\Delta$ , and chemical potential  $\mu_0$ .
2. Construct the BdG matrix in Equation 2–9 and find its eigenvalues and eigenvectors.
3. Find mean-fields using Equation 2–10. Let the values thus obtained be  $n_\sigma^{new}$  and  $\Delta^{new}$ .
4. Check convergence. If  $|n_\sigma^{new} - n_\sigma|, |\Delta^{new} - \Delta|, |n_0 - n_{avg}| < \epsilon$ , then convergence is achieved and there is no need for further iterations; otherwise go to the step 5. Here,  $\epsilon$  is the desired accuracy,  $n_{avg}$  is the average electron density at each iteration, and  $n_0$  is the desired electron density.
5. Update the mean-fields and chemical potential.

$$\begin{aligned}
n_\sigma &\rightarrow \beta n_\sigma^{new} + (1 - \beta)n_\sigma \\
\Delta &\rightarrow \beta \Delta^{new} + (1 - \beta)\Delta \\
\mu_0 &\rightarrow \mu_0 + \alpha(n_0 - n_{avg})
\end{aligned} \tag{2-19}$$

where  $0 < \alpha, \beta < 1$ . Here, mean-fields have been mixed with their values in the previous iteration. Such an update scheme is very often needed for the proper convergence of the self-consistent solution.

6. Go to step 2.

Using the self-consistent solution of the BdG equations, the lattice Green’s function matrix (Equation 2–12) is constructed in a ”supercell” set-up to achieve a better spectral resolution. The supercell method is described in detail in Appendix B. Local and diagonal elements of the lattice Green’s function matrix yield the lattice LDOS as in Equation 2–13. To find the continuum LDOS, values of the Wannier orbitals at the STM tip position, usually a few Angstroms above the exposed layer, are first extracted. Then using Equations 2–15 and 2–14 the continuum LDOS is obtained.

## CHAPTER 3 IMPURITY INDUCED STATES IN IRON BASED SUPERCONDUCTORS

In this chapter, I will discuss the effects of a single non-magnetic impurity in the superconducting FeSe. Most of the material presented here is based on a published paper [67]. All the published contents (excerpts and figures) are reprinted with permission from Peayush Choubey, T. Berlijn, A. Kreisel, C. Cao, and P. J. Hirschfeld, *Phys. Rev. B* **90**, 134520 (2014), copyright 2014 by the American Physical Society.

### 3.1 Motivation

Impurity induced states have been observed in STM studies on variety of FeSCs including FeSe [63, 84, 85], LiFeAs [77, 86], NaFeAs [49], LaOFeAs [87] and Na(Fe<sub>0.97-x</sub>Co<sub>0.03</sub>Cu<sub>x</sub>)As [79]. As an example, Figure 3-1(a) shows the STM topography of FeSe film grown on SiC(001) substrate. FeSe cleaves at the Se layer and the Fe layer resides below it <sup>1</sup>. Defects appear as atomic-scale bright dumbbell like structures ("geometric dimers"), labeled as  $\mu$  and  $\nu$ , and accompanying longer, unidirectional depressions of LDOS ("electronic dimers"). The electronic dimers are oriented at 45° with respect to geometric dimers, and extend to a length  $\approx 16a_{\text{Fe-Fe}}$ , where  $a_{\text{Fe-Fe}}$  denotes the Fe-Fe bond length, as shown in Figure 3-1(c). Similar features have been interpreted as emergent defect states in the ordered magnetic phase [88]. A zoomed-in view of geometric dimers (Figure 3-1(b)) shows them to be centered at the Fe atomic sites in the subsurface Fe layer with bright lobes extending to the neighboring Se atoms in the top-most Se layer. Due to mutually orthogonal arrangement of Se atoms in top layer around two inequivalent Fe atoms in the unit cell, geometric dimers appear in two orthogonal orientations labeled as  $\mu$  and  $\nu$  in Figure 3-1. It is not known conclusively whether these defect structures are caused by adatoms, Fe vacancies, or site switching, however, a recent first-principles study claims that the Fe vacancy is the most probable candidate [89].

---

<sup>1</sup> see Figure 1-4(a) for the details of the FeSe crystal structure

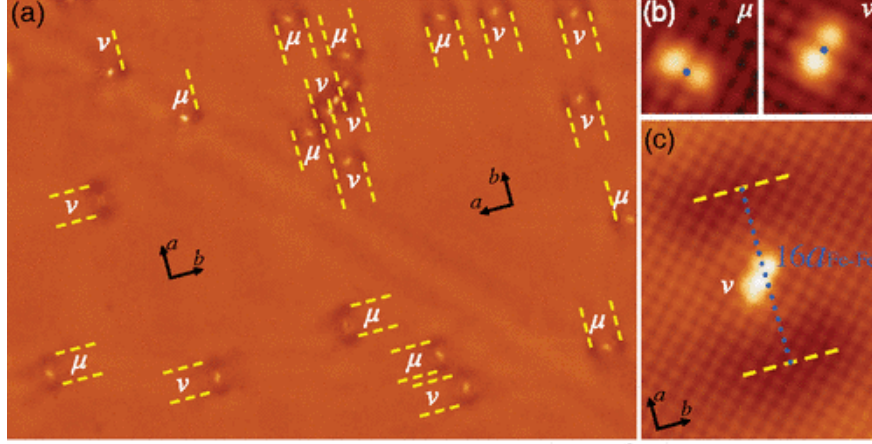


Figure 3-1. (a) STM topography of FeSe thin film grown on SiC(001) substrate. Defects appear as bright atomic-scale dumbbells (“geometric dimers”), surrounded by larger “electronic dimers” characterized by unidirectional depressions in the density of states. A twin boundary runs along the diagonal of the figure across which the crystalline axes, denoted by  $a$  and  $b$ , switch their orientation. (b) Zoomed-in view of defects. The mutually orthogonal geometric dimers, labeled as  $\mu$  and  $\nu$ , are centered at two inequivalent Fe atomic sites, in the subsurface Fe layer, and its bright lobes extend to the neighboring Se atoms in the top-most Se layer. (c) A larger, zoomed-in view of defects showing electronic dimers, marked by yellow dotted lines, which extend to a length  $\approx 16a_{\text{Fe-Fe}}$ . Subsurface Fe atoms are marked by blue dots in figures (b) and (c). Reprinted with permission from [63], copyright 2014 by the American Physical Society.

The STM experiments clearly suggest that the geometric dimer states involve coupling of the impurity with Se (or As in case of Fe-pnictides [49, 77, 79]) states in the topmost surface exposed to the STM tip, and hence, it can not be captured by a Fe-lattice only theoretical calculation, most often employed to study the impurity states in FeSCs [90–93]. The BdG+W approach described in Chapter 2, on the other hand, can account for the local  $C_4$  symmetry breaking due to Fe/Se atoms via the first-principles Wannier functions. Here, using a 10-orbital tight binding model for FeSe and corresponding Wannier functions derived from the DFT calculations, we show that the geometric dimer states can be understood as the consequence of impurity induced in-gap bound states in an  $s_{\pm}$  superconductor hybridizing with Se states.

In the following sections, we first describe the normal state electronic structure of FeSe within a DFT derived tight-binding model. Next, we use pair potentials obtained

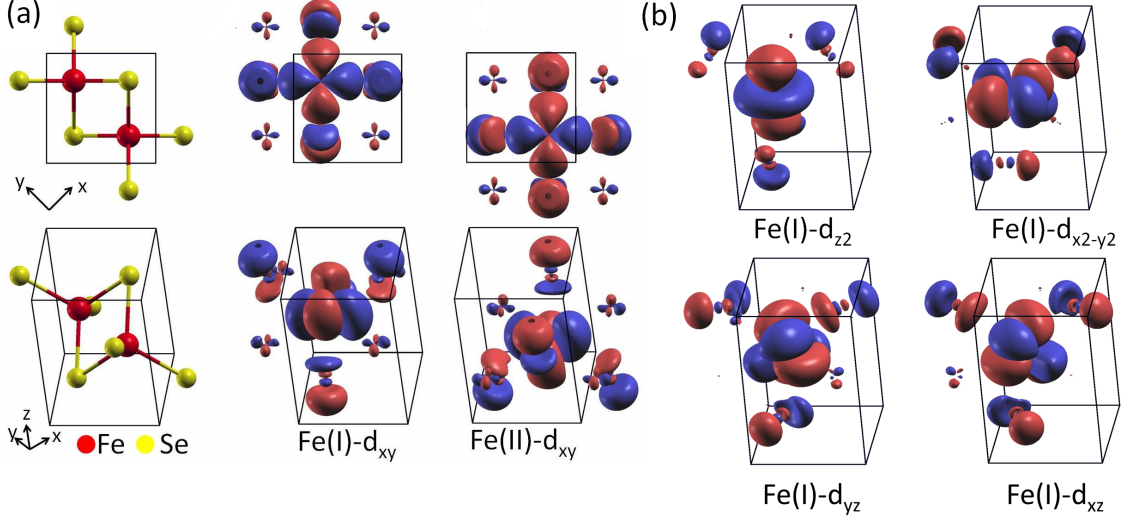


Figure 3-2. (a) Top and side view of the isosurface plots of FeSe  $d_{xy}$  Wannier orbital on Fe(I) and Fe(II) site obtained at isovalue  $0.03 \text{ bohr}^{-3/2}$ . Red and blue indicate sign of the Wannier orbital. (b) Isosurface plots of remaining Fe- $d$  Wannier orbitals on on Fe(I) site at the same isovalue.

from the spin-fluctuation theory to realize the  $s_{\pm}$  pairing symmetry and describe the properties of the homogeneous superconducting state. Then, within BdG+W framework, we study the response of a single point-like substitutional impurity and calculate the continuum LDOS at a typical STM tip position as well as a topographic map of the impurity state showing the emergence of geometric dimers.

### 3.2 Normal State Properties of FeSe

FeSe crystallizes in the symmetry group  $P4/nmm$  with lattice constants  $a = b = 7.13 \text{ bohr}$ ,  $c = 10.44 \text{ bohr}$  and fractional position of Se atoms  $z = 0.265c$  [94]. Starting with this experimental crystal structure information, the electronic structure of FeSe was calculated using the WIEN2K package [95]. DFT results show that the bands close to the Fermi energy have dominant contributions from Fe  $d$ -orbitals with small weights of Se  $p$ -orbitals. Subsequently, a 10-orbital Wannier basis was constructed by projecting the DFT wavefunctions [82] within the energy range  $[-2.5 \text{ eV}, 3 \text{ eV}]$  to Fe  $d$ -orbitals corresponding to the two in-equivalent Fe atoms namely Fe(I) and Fe(II). Figure 3-2(a) shows the top and side views of  $d_{xy}$ -Wannier orbitals on Fe(I) and Fe(II) sites. The

Wannier orbital is exponentially localized on the Fe sites with features that can be associated with the corresponding atomic orbital. Moreover, it has significant weights on other nearby atoms such as Fe and Se atoms in the same unit cell and Fe atoms in the two adjacent unit cells. Furthermore, at heights several Angstroms above the Se plane, where the STM tip would be typically placed, the dominant contribution to the Wannier orbitals is derived from the Se- $p$  states, as clearly seen in the side view of the isosurface plots (Figure 3-2(b), and bottom right plots in Figure 3-2(a)). In Section 3.4, we show that this particular feature of the Wannier orbitals gives rise to the geometric dimer impurity states. The Fe(I) and Fe(II) Wannier orbitals are related to each other by a symmetry transformation, namely translation by  $\mathbf{a}_{Fe-Fe}$  and subsequent reflection in Fe-plane. Thus in Figure 3-1(b) we only show the rest of the Wannier orbitals centered on Fe(I).

Figure 3-3(a) shows that the band structure obtained from downfolding to the 10-orbital Wannier basis compares very well with the DFT bands. To avoid the computational complexity associated with a 3D calculation, we ignore the hoppings in the  $z$ -direction and work with a 2D tight-binding model of the normal state described by Equation 2-2 with the filling set to  $n = 6$  electrons per Fe site. The orbitally-resolved DOS, and the Fermi surface with color-coded orbital character for this 2D model is shown in Figure 3-3(b) and 3-3(c), respectively. The DOS is mostly flat around the Fermi level and has largest contributions from Fe- $d_{xy}$ ,  $d_{xz}$ , and  $d_{yz}$  Wannier orbitals. The Fermi surface has three hole pockets centered around  $\Gamma$  point (Brillouin zone center) and two electron pockets centered at the M point (Brillouin zone corners) in the 2-Fe Brillouin zone as shown in Figure 3-3(c). The inner and outer hole pockets have  $d_{yz}/d_{xz}$  characters whereas middle hole pocket has  $d_{xy}$  character. The outer and inner electron pockets have  $d_{xy}$  and  $d_{yz}/d_{xz}$  characters, respectively.

Figure 3-3(d) shows a very recent ARPES determined  $k_z = \pi$  (in reciprocal lattice units) cut of the quasi-2D Fermi surface of FeSe at  $T = 7$  K [96]. Note that since the measurements were taken in the nematic phase ( $T < T_s \approx 90$  K), the Fermi surface

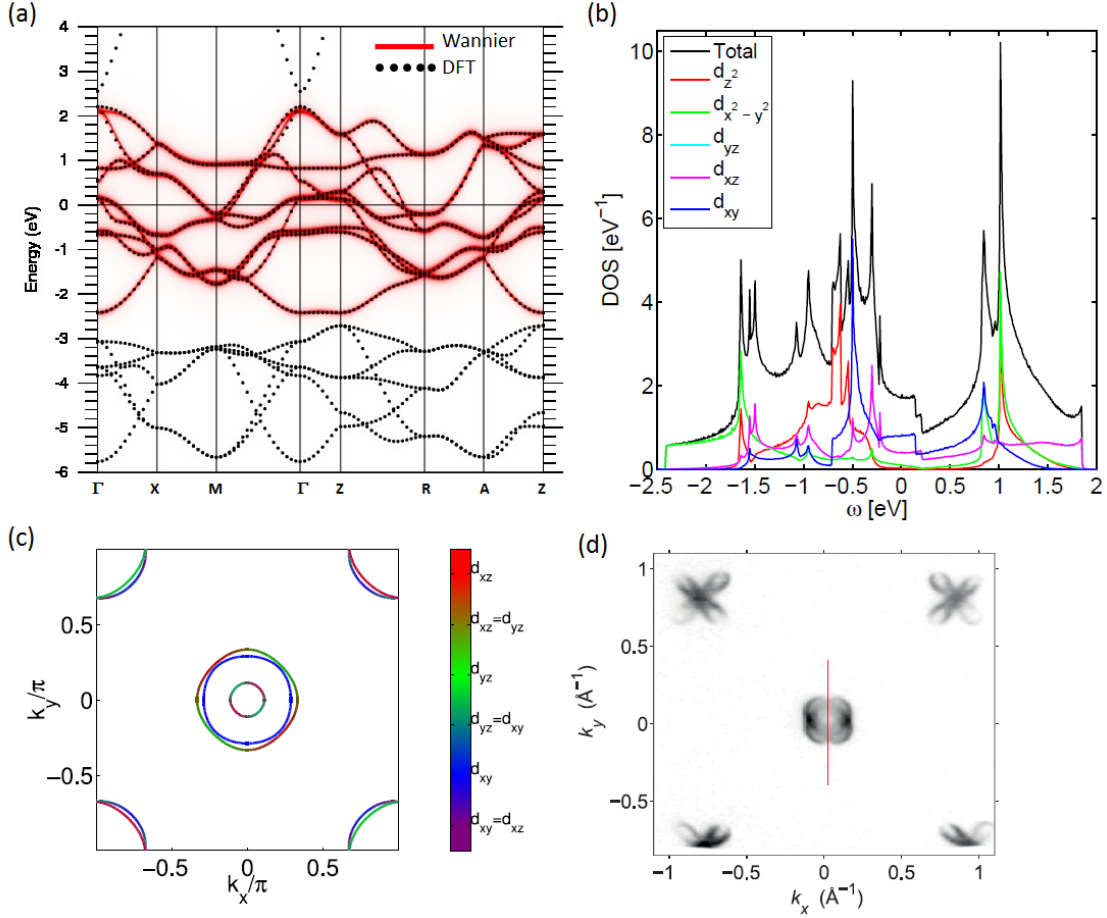


Figure 3-3. (a) Electronic structure of FeSe showing DFT and Wannier-fitted bands. (b) FeSe Fermi surface with color-coded orbital character. (c) Orbital-resolved density of states in the normal state. (d) The ARPES determined Fermi surface of FeSe at  $T = 7$  K. Reprinted with permission from [96], copyright 2016 by the American Physical Society.

shown here also contains duplicate electron and hole pockets rotated by  $90^\circ$ , arising from twin domains. Clearly, the hole pockets at Brillouin zone center and electron pockets at the corners show significant shrinkage compared to the DFT-determined Fermi surface by almost a factor of  $\sim 5$  [97]. Moreover, ARPES observes only one hole pocket at the Brillouin zone center with  $d_{xz}/d_{yz}$  character, and two electron pockets at the Brillouin zone corners with outer (inner) pocket having  $d_{xy}$  ( $d_{xz}/d_{yz}$ ) character [96], in contrast to the three hole pockets and two electron pockets in the DFT-derived Fermi surface. At the time our work was done, there were no available ARPES data due to lack of clean

FeSe samples. Hence, we assumed that the normal state of the FeSe is reasonably well represented by the DFT-derived band structure. Moreover, we did not take into account the small orthorhombic distortion of the lattice at low temperatures ( $T < T_s$ ). However, these differences will not change our final conclusion regarding the origin of the geometric dimer states, which is based on the presence of an impurity-induced bound state in an  $s_{\pm}$  superconductor, and the shape of the Wannier function, displaying Se tails.

### 3.3 Homogeneous Superconducting State

The symmetry and structure of superconducting gap in FeSe is not well established. Earlier STM experiments on FeSe thin films [63, 84] and recent measurements on FeSe single crystals [85] shows that the superconducting gap has a V-shape at low energies indicating presence of nodes or deep minima. Here, we will not attempt to obtain a gap structure that yields the correct tunneling LDOS, instead, we assume an  $s_{\pm}$  pairing symmetry, which is widely believed to be the correct symmetry for many of FeSCs [98–100], and focus on a qualitative understanding of the coupling between the in-gap bound states localized at the impurity site in the Fe layer, and the neighboring Se atoms in the top-most layer exposed to the STM tip. Since, the geometric dimer states have been seen in a variety of FeSCs, it is very likely that these states are insensitive to the details of the gap structure such as presence or absence of nodes.

In the simplest scenario, the  $s_{\pm}$  superconducting state in FeSCs can be understood as a consequence of the near-nesting between electron and hole pockets augmented with stronger inter-band electron-electron interaction [99, 101]. It is easy to see from the schematic of the generic Fermi surface shown in Figure 1-4(c) that a translation by  $\mathbf{Q} = [\pi, 0]$  or  $[0, \pi]$  (in 1-Fe Brillouin zone) nearly superposes the hole pocket on the electron pockets. This "nesting" is not perfect due to the difference in size and shape of the pockets, however, it is sufficient to cause a peak in the transverse spin susceptibility  $\chi(\mathbf{q}, \omega \rightarrow 0)$  at the momentum transfer  $\mathbf{q} = \mathbf{Q}$ , pushing the material close to a possible antiferromagnetic (AFM) transition. If the inter-band Coulomb repulsion is larger than

the intra-band repulsion then it turns out that the strong AFM spin-fluctuations at  $\mathbf{q} = \mathbf{Q}$  lead to an effective electron-electron interaction (repulsive) in the Cooper channel ( $V_{\mathbf{k}\mathbf{k}'}$ ) which peaks at  $\mathbf{k} - \mathbf{k}' = \mathbf{Q}$  [99]. For such interaction, BCS gap equation (Equation 1–5) admits a non-trivial solution only if the gap changes sign between electron and hole pockets, thus yielding an  $s_{\pm}$  state. However, this simplistic scenario excludes the effects of orbital content of the Fermi surface that plays a crucial role in determining the anisotropy of the superconducting gap on the Fermi surface [98, 102, 103]. A better alternative is to use the multi-orbital spin fluctuation theory with DFT-determined band structure [98, 102, 104, 105]. In following, we briefly describe the calculation of real-space pair potentials ( $V_{ij}^{\mu\nu}$ ) from spin-fluctuation theory within the random phase approximation (RPA). The details of calculation can be found in Refs. [92, 98, 102, 105].

We start with the following Hubbard-Hund Hamiltonian in conjunction with the non-interacting Hamiltonian  $H_0$  (Equation 2–2),

$$H_{\text{int}} = U \sum_{i,\mu} n_{i\mu\uparrow} n_{i\mu\downarrow} + U' \sum_{i,\nu < \mu} n_{i\mu} n_{i\nu} + J \sum_{i,\nu < \mu} \sum_{\sigma,\sigma'} c_{i\mu\sigma}^{\dagger} c_{i\nu\sigma'}^{\dagger} c_{i\mu\sigma'} c_{i\nu\sigma} + J' \sum_{i,\nu \neq \mu} c_{i\mu\uparrow}^{\dagger} c_{i\mu\downarrow}^{\dagger} c_{i\nu\downarrow} c_{i\nu\uparrow} \quad (3-1)$$

Here,  $i$  runs over unit cells, each containing two Fe atoms,  $U' = U - 2J$  and  $J' = J$  due to spin and orbital rotational invariance [104]. Moreover,  $\sum'$  signifies that only those values of  $\mu$  and  $\nu$  should be considered in the sum which label orbitals on the same Fe atom. We choose  $U = 0.9$  eV,  $J = U/4$  to yield a robust instability in the superconducting channel, and calculate pairing vertices in the momentum space using the following formula from spin fluctuation pairing theory [106].

$$\Gamma_{\mu_1\mu_2\mu_3\mu_4}(\mathbf{k}, \mathbf{k}') = \left[ \frac{3}{2} \bar{U}^s \chi_1^{\text{RPA}}(\mathbf{k} - \mathbf{k}') \bar{U}^s \frac{1}{2} \bar{U}^s - \frac{1}{2} \bar{U}^c \chi_0^{\text{RPA}}(\mathbf{k} - \mathbf{k}') \bar{U}^c + \frac{1}{2} \bar{U}^c \right]_{\mu_1\mu_2\mu_3\mu_4} \quad (3-2)$$

The definitions of matrices  $\bar{U}^s$  and  $\bar{U}^c$  can be found in Ref. [102]. Within RPA, the charge and spin susceptibilities are given as

$$\begin{aligned} [\chi_1^{\text{RPA}}(\mathbf{q})]_{\mu_1\mu_2\mu_3\mu_4} &= \left\{ \chi^0(\mathbf{q}) [1 - \bar{U}^s \chi^0(\mathbf{q})]^{-1} \right\}_{\mu_1\mu_2\mu_3\mu_4}, \\ [\chi_0^{\text{RPA}}(\mathbf{q})]_{\mu_1\mu_2\mu_3\mu_4} &= \left\{ \chi^0(\mathbf{q}) [1 + \bar{U}^c \chi^0(\mathbf{q})]^{-1} \right\}_{\mu_1\mu_2\mu_3\mu_4}, \end{aligned} \quad (3-3)$$

where  $\chi^0(\mathbf{q})$  is the bare susceptibility defined explicitly in Ref. [102]. The real-space pair potentials can be calculated by projecting the momentum-space vertices to the spin-singlet channel followed by a Fourier transform to real space.

$$V_{ij}^{\mu\nu} = \frac{1}{2} \sum_{\mathbf{k}} [\Gamma_{\mu\nu\nu\mu}(\mathbf{k}, -\mathbf{k}) + \Gamma_{\mu\nu\nu\mu}(\mathbf{k}, \mathbf{k})] e^{-i\mathbf{k}\cdot(\mathbf{R}_i - \mathbf{R}_j)}, \quad (3-4)$$

As shown in Figure 3-4(a), the pair potentials thus obtained form a checkerboard pattern and show a rapid spatial decay. The pattern is dominated by the on-site intra-orbital ( $V_{ii}^{\mu\mu}$ ) repulsion varying in a range of 1.2 eV to 4 eV. The largest values of the attractive pair potential occur at nearest neighbor (NN) and next-nearest neighbor (NNN) sites with  $V_{NN}^{\mu\nu} > V_{NNN}^{\mu\nu}$ .

Using  $V_{ij}^{\mu\nu}$  as an input, we solve 10-orbital BdG equations on a square lattice with  $15 \times 15$  unit cells using the self-consistency scheme described in Section 2.4. The resulting superconducting gap parameter  $\Delta_{ij}^{\mu\nu}$  is rather short-ranged, and has largest values in the subspace spanned by the orbitals  $\mu, \nu = (d_{xy}, d_{xz}, d_{yz})$  as shown in Figure 3-4(b). Its origin can be traced back to the fact that these three orbitals have the largest DOS at the Fermi level. Moreover, the spatial pattern of  $\Delta_{ij}^{\mu\nu}$  reflects the symmetries of the underlying orbitals. For example,  $\Delta_{ij}^{\mu\mu}$  for  $\mu = d_{xy}$  displays a  $C_4$  symmetry whereas for  $\mu = d_{xz}, d_{yz}$  it shows a  $C_2$  symmetry. Furthermore, due to degeneracy of  $d_{xz}$  and  $d_{yz}$  DOS at the Fermi surface, the corresponding gap values are related to each other by a  $\pi/2$  rotation. The momentum space structure of the gap can be found by the Fourier transforming the real-space gap followed by an orbital-to-band basis transformation using the normal state eigenvectors. The resulting  $\Delta(\mathbf{k})$  is displayed in Figure 3-4(c). Clearly,  $\Delta(\mathbf{k})$  preserves

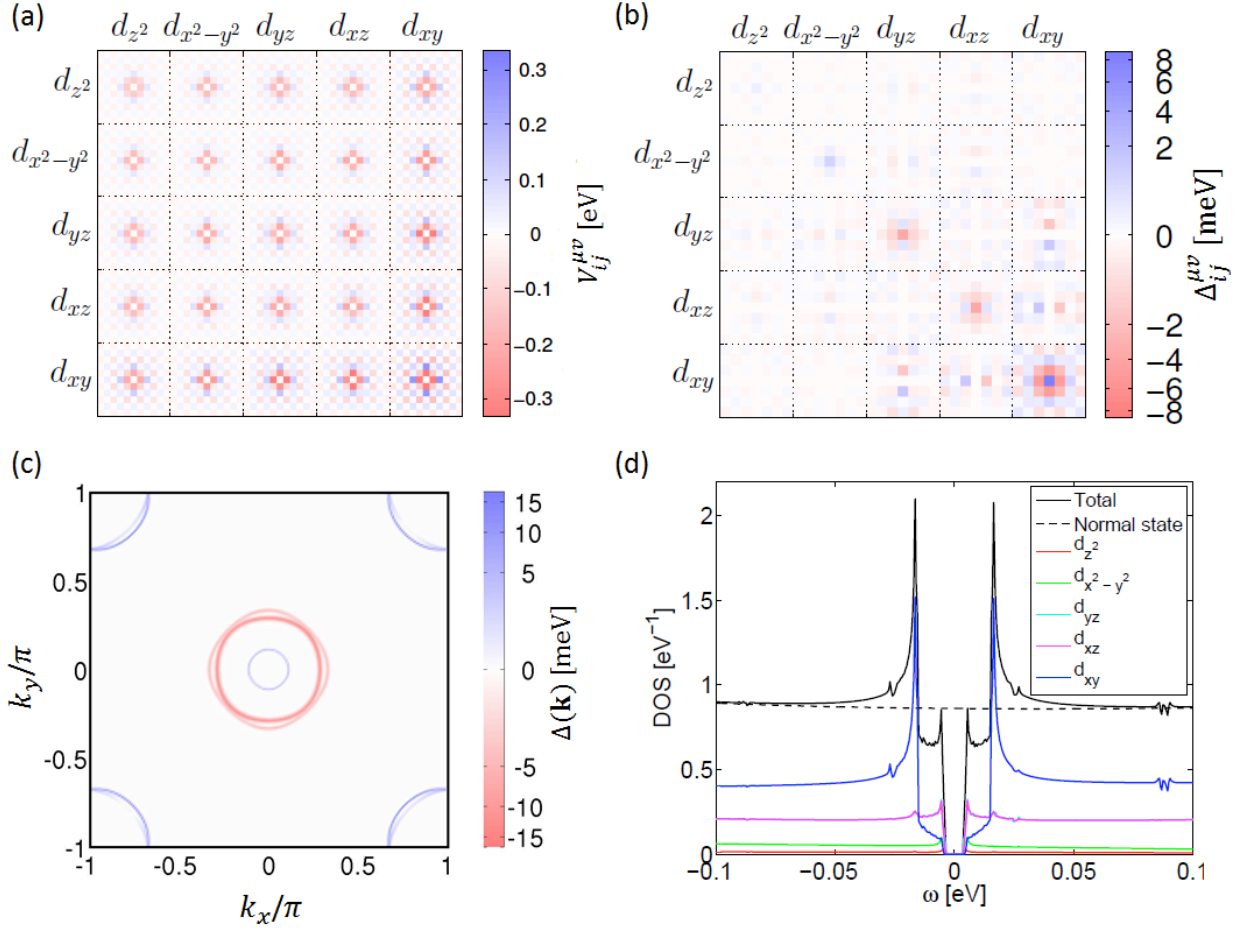


Figure 3-4. (a) Pair potentials ( $V_{ij}^{\mu\nu}$ ) in real- and orbital-space. Each pixel represents an Fe site. Diagonal terms  $V_{ii}^{\mu\mu}$ , varying in a range of 1.2 eV - 4 eV, are not shown here to emphasize smaller, off-diagonal pair potentials. (b) Superconducting gap  $\Delta_{ij}^{\mu\nu}$  obtained from the self-consistent solution of BdG equations. (c) Superconducting gap ( $\Delta(\mathbf{k})$ ) in momentum-space. (b) and (c) have been plotted on a square-root scale to emphasize smaller values. (d) Orbitaly resolved density of states in the superconducting state.

all symmetries of a square lattice, but changes sign between outer hole pockets centered at the Brillouin zone center ( $\Gamma$  point) and electron pockets centered at the Brillouin zone corner ( $M$  point), yielding an  $s_{\pm}$  symmetry. Note that the gap on the inner hole pocket also changes sign with respect to the outer hole pockets. The occurrence of the largest gap values on the middle hole pocket and the outer electron pocket can be traced back to their dominant  $d_{xy}$  character. Figure 3-4(d) shows the low-energy orbital-resolved DOS in the superconducting state compared with the normal state DOS. The total DOS in

superconducting state shows two-gap like features with inner coherence peaks at  $\omega = \pm 5.5$  meV and outer coherence peaks at  $\omega = \pm 16.5$  meV. The inner coherence peaks have dominant contribution from degenerate  $d_{xz}$  and  $d_{yz}$  orbitals whereas the outer peaks is mainly contributed from  $d_{xy}$  orbitals. We deliberately chose the interaction parameters to yield a larger gap magnitude (16.5 meV) compared to the much smaller value ( $\approx 3$  meV) observed in the STM experiments [84] in order to clearly visualize the impurity bound state within our numerical resolution.

### 3.4 Effects of an Impurity

As discussed in Section 2.2.1, we can model a non-magnetic impurity in the simplest possible way by an on-site potential  $V_{\text{imp}}$  which is diagonal and identical for all orbital channels. This approximation is supported by the first-principles studies of the impurity potentials in several Fe-based materials finding a very small orbital dependence [107–109]. The existence of a non-magnetic impurity-induced in-gap bound state in an  $s_{\pm}$  superconductor has been found to be very sensitive to the sign and magnitude of the impurity potential, details of the underlying band structure, and the gap function [91, 92, 98]. We choose a repulsive impurity potential  $V_{\text{imp}} = 5$  eV to realize an in-gap bound state at  $\Omega = \pm 2$  meV. We stress that the numerical value of the impurity potential used here has no special significance beyond the fact that it induces an in-gap bound state. We are just interested in examining the spatial form of the bound state; any value of impurity potential which induces such state at any in-gap energy is an equally good choice, and qualitative conclusions drawn in following paragraphs will stay the same. As in the case of homogeneous system described in Section 3.3, we work with a  $15 \times 15$  unit-cells lattice and replace one Fe atom in the the unit cell [8,8] by an impurity. After solving the 10-orbital BdG equations self-consistently, we construct the lattice Green's function using  $20 \times 20$  supercells which yield a spectral resolution of order  $\sim 0.5$  meV.

Figure 3-5(a) shows the lattice LDOS ( $N_i(\omega)$ ) spectrum (calculated using Equation 2-13) far from the impurity, at the impurity site, on the NN site, and on the NNN site.

Since the impurity potential is comparable to the band width, it acts as a strong repulsive potential scatterer, heavily suppressing the LDOS at the impurity site. The impurity induced in-gap bound states at  $\Omega = \pm 2$  meV are clearly observed in the LDOS spectrum at the NN and NNN sites. Figure 3-5(b) and (c) show the lattice LDOS map around the impurity site at the resonance energies. We find that the spatial pattern around the impurity preserves the  $C_4$  symmetry of the underlying square lattice, as it should, and is very different from the  $C_2$  symmetric dimer-like patterns observed in the STM experiments [63]. It is necessary to take into account Se states that breaks the  $C_4$  symmetry in a manner consistent with the orientation of the experimentally observed geometric dimers. This can be achieved by the calculating continuum LDOS above the Se surface, exposed to the STM tip, using Wannier orbitals as described in Section 2.3.2.

Figure 3-6 shows the continuum LDOS  $\rho(\mathbf{r} = (x, y, z), \omega)$  maps computed from Equations 2-14 and 2-18 at various heights  $z$  measured from Fe-plane, at various biases. The resonance pattern is  $C_4$  symmetric in the Fe-plane ( $z = 0$ ), as shown in Figure 3-6(d). Moreover, it resembles closely the corresponding lattice LDOS map plotted in Figure ??(c). Moving above the Fe-plane lowers the local symmetry to  $C_2$  due to placement of the Se atoms. Consequently, the LDOS maps taken right above the Fe-plane (Figure 3-6(f)), and above the Se-plane (Figure 3-6(a)-(c)) are  $C_2$  symmetric. More importantly, the LDOS maps above the Se-plane exhibit a geometric dimer-like structure with bright lobes positioned at the two NN (up) Se atoms as shown in Figure 3-6(a)-(c). Such a pattern is visible at all energies, however, with a variation in the intensity at NNN (up) Se positions. The origin of these dimer-like patterns can be understood as a consequence of the particular shape of the Wannier orbitals above the Se-layer, and the spatial pattern of the lattice LDOS. Using Equations 2-13, 2-14, and 2-18, we can write

$$\rho(\mathbf{r}, \omega) = \sum_{i, \mu} N_{i\mu}(\omega) |w_{i\mu}(\mathbf{r})|^2 + \text{off-diagonal terms } (i \neq j, \mu \neq \nu) \quad (3-5)$$

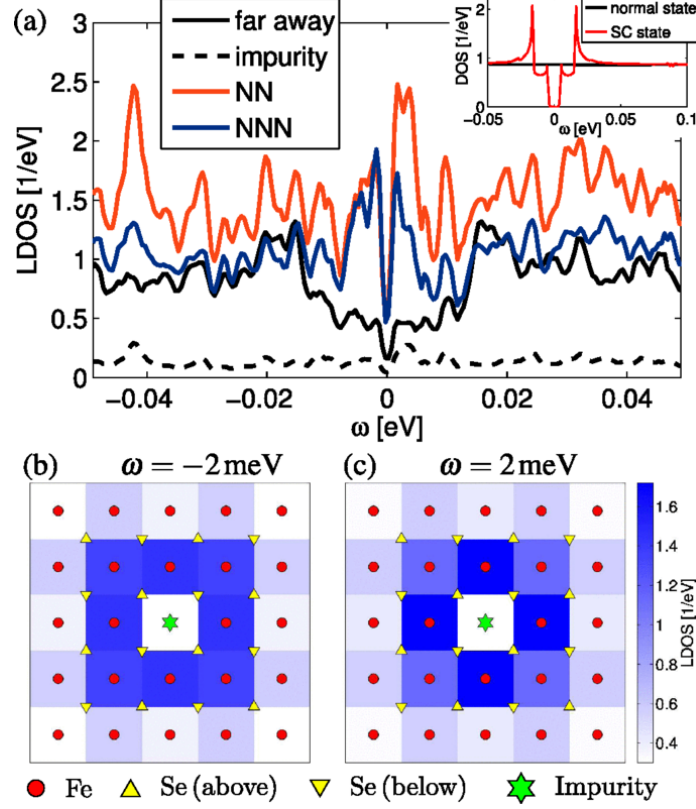


Figure 3-5. (a) Lattice LDOS spectrum in the superconducting state, far from the impurity, at the impurity site, on the NN site, and on the NNN site. Inset shows density of states in the homogeneous superconducting and normal states. (b) Real-space pattern of lattice LDOS at the bound state energy  $\Omega = 2$  meV and (c)  $\Omega = -2$  meV. Each square pixel represents an Fe site.

Now, Figure 3-2 shows that for the heights we are considering, the Wannier orbitals  $w_{i\mu}(\mathbf{r})$  have significant weights only around the up-Se atoms. Moreover, the lattice LDOS, shown as a cartoon in Figure 3-6(a)-(b), is largest at the NN and NNN sites. Thus, ignoring off-diagonal terms in Equation 3-5, we find that the LDOS has the largest values at (up) NN and (up) NNN Se-atoms leading to the observed patterns. The off-diagonal terms involve the product of exponentially localized Wannier functions at different sites and/or with different orbital symmetries, and their sign is not fixed, hence their contribution is usually smaller than the diagonal terms. This is particularly true in the case of the LDOS maps shown in Figure 3-6(a)-(c). However, neglecting these terms can lead to wrong results as illustrated in Figure 3-6(e) and (f). The former shows that ignoring

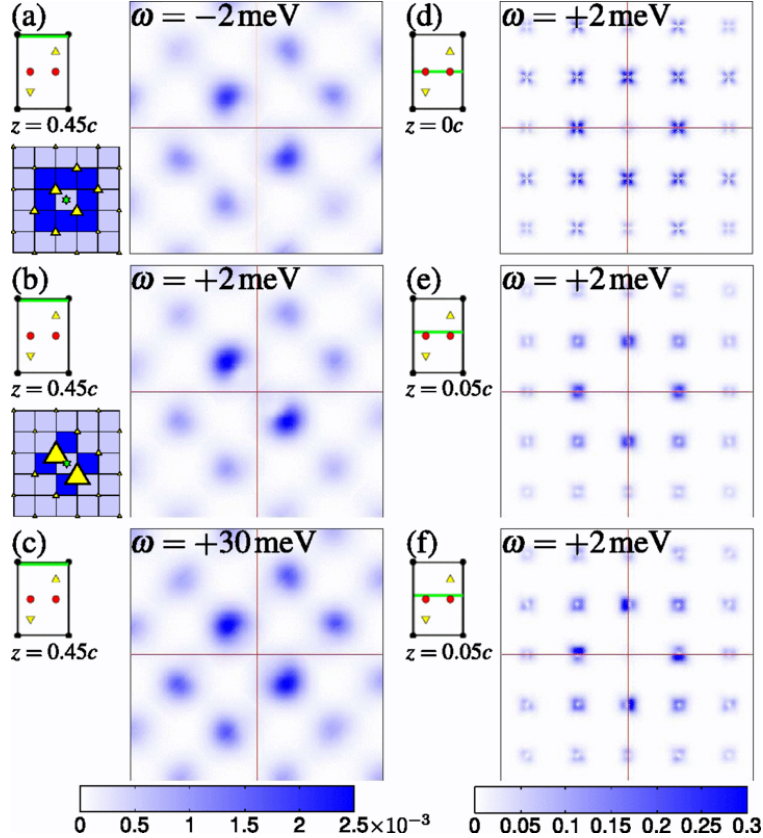


Figure 3-6. Continuum LDOS maps at height  $z = 0.045c$  (above Se-plane), and energies (a)  $\omega = -2$  meV, (b) 2 meV, and (c) 30 meV, and at height  $z = 0c$  (at the Fe-plane) (d),  $z = 0.5c$  (close to the Fe-plane) [(e), (f)] and the same energy  $\omega = 2$  meV. All maps are obtained from Equation 2-18 except (e) which includes only local and diagonal ( $i = j, \mu = \nu$ ) terms. Colorbar values are in the units of  $\text{eV}^{-1}\text{bohr}^{-3}$ . The position of  $z$ -cuts relative to the unit-cell is visualized by a green line in the schematic of the side-view of FeSe unit cell. Red circles and yellow triangles represent Fe and Se atoms respectively. The cartoon of lattice LDOS patterns at  $\omega = \pm 2$  meV (compare Figure 3-5(b) and (c)) is shown in (b) and (c) to explain the particular shape of continuum LDOS patterns.

the off-diagonal terms leads to a  $C_4$  symmetric LDOS map just above the Fe-plane. The correct  $C_2$  symmetry is recovered only if these terms are included as shown in Figure 3-6(f).

At the time this work was done, the experimental results for the bias dependence of the tunneling conductance maps around the impurity were not published. Instead, Ref. [63] reported the topography of the FeSe surface as described in Section 3.1. To

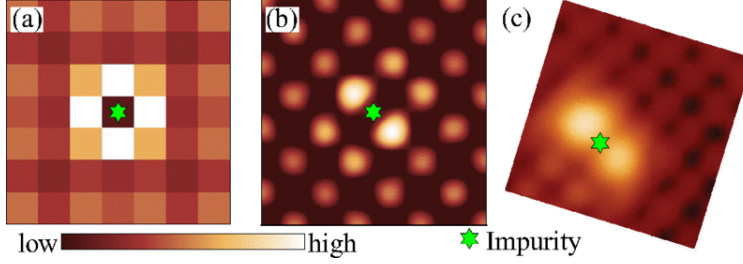


Figure 3-7. Theoretical topograph of impurity states at 6 meV obtained from (a) BdG calculations (b) BdG+W method. In (a) each pixel represents an Fe site. (c) Experimental topograph of impurity states, reproduced from [63], rotated to match orientation of lattice vectors in (a) and (b). Reprinted with permission from [63], copyright 2014 by the American Physical Society.

compare with the experimental result, we calculate the topographic map using the energy integrated continuum LDOS. The STM tunneling current at a given bias  $V$  can be approximated as [56]

$$I(x, y, z; V) = -\frac{4\pi e}{\hbar} \rho_t(0) |M|^2 \int_0^{eV} \rho(x, y, z; \epsilon) d\epsilon, \quad (3-6)$$

Here,  $\rho$  is the continuum LDOS,  $(x, y, z)$  is the STM tip position,  $\rho_t(0)$  is the density of states of the tip at the Fermi energy, and  $M$  is the tunneling matrix element. A topograph at bias  $V$  and set-point current  $I_0$  is defined by the condition  $I(x, y, z; V) = I_0$  which is equivalent to  $\int_0^{eV} \rho(x, y, z; \epsilon) d\epsilon = \text{constant}$ . We obtain the height  $z(x, y)$  satisfying this condition, with energy integrated LDOS and bias set to  $3.45 \times 10^{-7} \text{ eV}^{-1} \text{ bohr}^{-3}$  and 6 mV, respectively. The result is shown in Figure 3-7. Clearly, a BdG-only lattice calculation (Figure 3-7(a)) yields a  $C_4$  symmetric topograph which is very different from the experimental result shown in Figure 3-7(c). However, the topograph calculated using BdG+W approach yields result very similar to the experimental observation.

### 3.5 Conclusion

As the first application of the BdG+W method introduced in Chapter 2, we studied the response of the superconductor FeSe to a single point-like impurity on a Fe site. We started with a DFT derived 10-orbital tight-binding model of the FeSe normal state and corresponding Wannier basis. The  $s_{\pm}$  superconducting state is introduced through

the real-space pair potentials obtained from the spin-fluctuation theory calculation performed within random phase approximation. By solving the 10-orbital BdG equations self-consistently, we found that a strong non-magnetic impurity, modeled simply as an on-site repulsive potential, induces bound states in the  $s_{\pm}$  superconducting gap. Using Wannier functions, we obtained high-resolution continuum LDOS maps at various biases and heights from the Fe-plane, and demonstrated that the BdG+Wannier method yields a qualitative improvement over the conventional BdG results by capturing the local symmetry internal to the unit cell. Moreover, we showed that the geometrical dimer states observed in STM experiments on FeSe and several other FeSC originate from the hybridization of impurities, located at Fe sites, with the Se (As) states. Finally, we showed that the topographic map calculated using continuum LDOS compared very well with the STM topograph obtained at the same bias.

## CHAPTER 4 IMPURITY INDUCED STATES IN CUPRATES

In this chapter, I will discuss the effects of single non-magnetic as well as magnetic impurity in a cuprate superconductor  $\text{Bi}_2\text{Sr}_2\text{CaCu}_2\text{O}_{8+\delta}$  (BSCCO). Some of the material presented here is based on a published paper [110]. All the published contents (excerpts and figures) are reprinted with permission from [A. Kreisel, Peayush Choubey, T. Berlijn, W. Ku, B.M. Andersen, and P.J. Hirschfeld, Phys. Rev. Lett. 114, 217002 \(2015\)](#), copyright 2015 by the American Physical Society. I contributed to all of the following sections except Section 4.6.

### 4.1 Motivation

The experimental observation of Zn impurity-induced resonance states in the cuprate compound BSCCO [60, 111–113] was a strong indicator of unconventional pairing in this class of superconductors. Simple theoretical calculations treating impurities as point-like potential scatterers in a  $d$ -wave superconductor had already predicted the existence of such states [61]. However, the details of the STM conductance spectra displayed two important deviations from the theoretical predictions [60, 68, 75]. First, the conductance maximum was found at the impurity site where theory had predicted a conductance minimum. Second, the long-range intensity tails were found to be oriented along Cu-O bond directions,  $45^\circ$  rotated from the theoretically predicted Cu-Cu bond direction along which low-energy nodal quasiparticles exist, and can lead to such long range tails [75]. Similar discrepancies also occurred in case of Ni (a magnetic impurity) doped BSCCO [64, 68, 75]. Several remedies were proposed to reconcile with the experiments, including extended impurity potentials [114–116], Kondo-like effects [117], Andreev scattering at impurities [118], and "filter" effects [62, 119]. The last postulated that the intervening layers between STM tip and CuO layer provide an alternate tunneling path making the tip sensitive to the nearest-neighbor Cu sites instead of the impurity site beneath it. First-principles calculations of the impurity induced states in the normal state of

BSCCO [120], and an analysis based on several atomic-like orbitals [121] supported the phenomenological filter theories, but it was not clear how to include superconductivity as well as effect of intervening layers together in presence of disorder.

Here, we show that the continuum LDOS obtained in the vicinity of a strong non-magnetic impurity and a magnetic impurity using the BdG+W framework shows excellent agreement with the corresponding STM results for Zn [60] and Ni [64] doped BSCCO. We find that the STM conductance patterns can be easily explained by accounting for the Cu- $d_{x^2-y^2}$  Wannier function tails with significant weight coming from the apical oxygen atoms in the nearest neighbor unit cells, putting the crude filter theories on a firm microscopic footing.

In the following sections, we first describe the properties of the normal and superconducting state of BSCCO using a DFT derived tight-binding Hamiltonian and nearest-neighbor pair potential put in "by hand" to yield a  $d$ -wave gap with magnitude similar to that observed in the STM experiments [60]. Then we study the Zn impurity problem by treating it as a strong point-like potential scatterer in a  $d$ -wave superconductor, and compute continuum LDOS at a typical STM tip height, demonstrating an excellent agreement between theory and the experiment [60]. Finally, we study the Ni impurity problem using a very simple model of a magnetic impurity [68, 75, 122] and show that it induces two spin polarized in-gap resonance states as predicted [122]. Moreover, the continuum LDOS patterns at the resonance energies and at a typical STM tip height agrees very well with the experiment [64]. However, the relative weights of the two resonance states are found to be reversed compared to the experimental result. We show that including nearest neighbor potential and magnetic scattering yields the correct relative weights of the resonance peaks, however, the microscopic origin of such an impurity model is not clear yet.

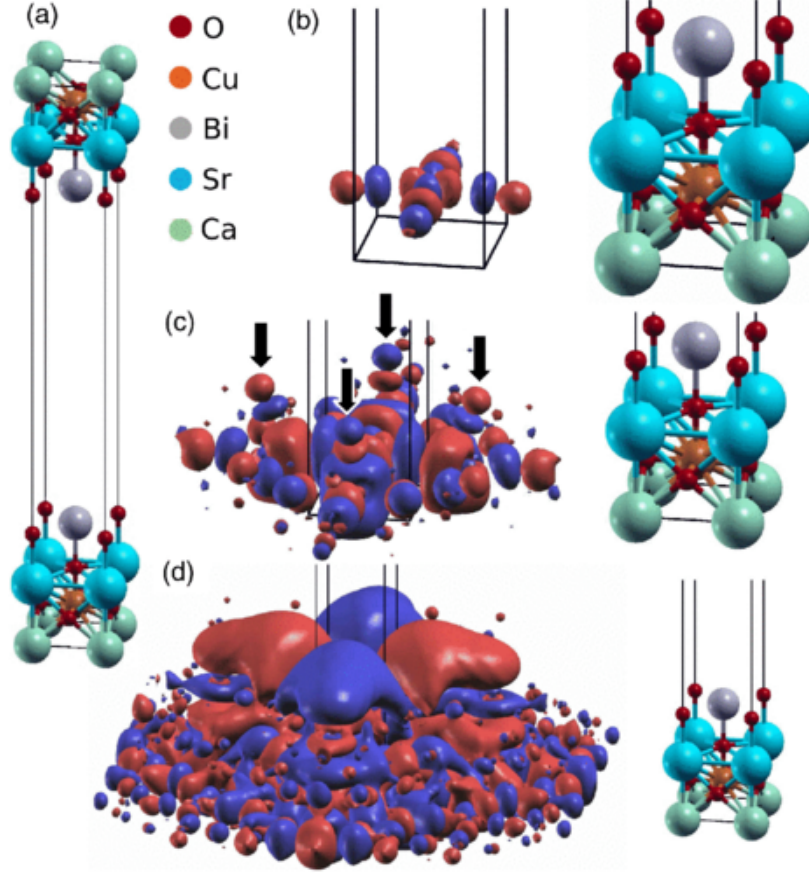


Figure 4-1. (a) Elementary cell used in the DFT calculation to obtain electronic structure of BSCCO. Isosurface plots of Cu- $d_{x^2-y^2}$  Wannier function in BSCCO at isovalue (b) 0.05 (b) 0.005 (c) 0.0002 bohr $^{-3/2}$ . Arrows point to the apical oxygen tails in the nearest-neighbor unit cells. Red and blue represent the sign of the Wannier function.

## 4.2 Normal State

We first obtain a one-band tight-binding model and the corresponding Wannier functions for BSCCO using first principles calculations. The elementary cell used in band structure calculations is shown in Figure 4-1(a). The BSCCO crystal used in experiments like STM [57] and ARPES [27] cleaves at the BiO layer. Hence, it is more appropriate to obtain the BSCCO Wannier functions for the BiO terminated surface instead of the bulk. Accordingly, we take a body-centered tetragonal unit-cell terminated at the BiO layer with a  $\approx 18.5$  Å vacuum slab as shown in Figure 4-1(a), and perform electronic structure calculations using the WIEN2K package [95]. The crystal structure parameters were

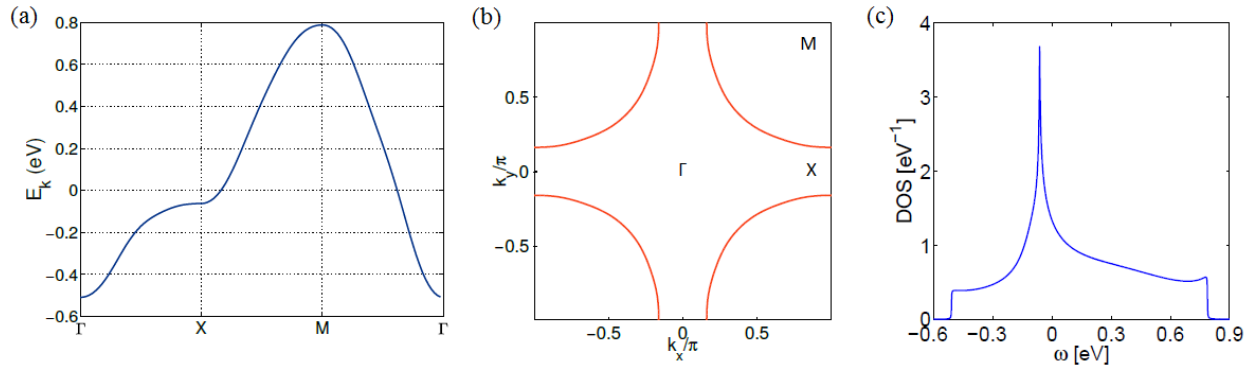


Figure 4-2. (a) Band structure and (b) Fermi surface corresponding to the renormalized 1-band tight-binding model of BSCCO. (c) Density of states in the normal state.

adopted from the Ref. [123]. Subsequently, the Wannier function was constructed, using a projected Wannier method [82], by projecting Cu- $d_{x^2-y^2}$  orbital on DFT wavefunctions in an energy window of [-3, 3] eV. The isosurface plots of the resulting Wannier function are shown in Figure 4-1(b)-(d). For the large isovalues the Wannier function is localized in CuO plane and reflects a strong hybridization between Cu- $d_{x^2-y^2}$  states and in-plane O- $p$  states as shown in Figure 4-1(b). The contributions of other atoms, especially the apical O atoms from the neighboring unit cells, becomes apparent with decreasing isovalues. The lobes associated with apical O- $p$  states (marked with arrows in Figure 4-1(c)) are the main source of the peculiar structure of this particular Wannier function (Figure 4-1(d)) at the heights few Å above the BiO layer where STM tip will typically reside. At these heights, Wannier function has zero weight directly above the center Cu and largest weight above the nearest-neighbor (NN) Cu atoms.

The tight-binding parameters obtained in the Wannier basis described above yield a band structure with much larger Fermi velocity compared to that observed in the ARPES experiments [27, 124], a consequence of the inadequate treatment of correlations in the DFT calculations. On a crude level, we can account for the correlation effects by using an overall renormalization of tight-binding parameters by a factor  $1/Z$ . We divide all tight-binding parameters by  $Z = 3$  to approximately match the experimentally

observed Fermi velocity [27]. Also, we fix the electron filling per Cu site to be  $n = 0.85$  corresponding to optimal doping. The band structure, Fermi surface, and DOS corresponding to the renormalized tight-binding parameters and aforementioned filling are shown in Figure 4-2(a), (b), and (c), respectively. A van-Hove peak at  $\omega = -63$  meV, arising as a consequence the flat band near the X point, is easily observed in the spectrum.

### 4.3 Homogeneous Superconducting State

The superconducting state with  $d$ -wave symmetry is obtained by putting in attractive pair-potentials ( $V_{ij}$ ) "by hand" such that  $V_{ij} = V_0$ , with if sites  $i$  and  $j$  are nearest neighbors and zero otherwise. Choosing  $V_0 = 150$  meV and solving 1-orbital BdG equations on a  $35 \times 35$  square lattice yields a  $d$ -wave superconducting gap that can be represented in the momentum space as  $\Delta(\mathbf{k}) = \frac{\Delta_0}{2}(\cos k_x - \cos k_y)$  with  $\Delta_0 \approx 33$  meV. The value of the spectral gap thus obtained is very similar to the experimentally observed value [57, 60]. The density of states in the superconducting state is compared to the normal state in Figure 4-3(a). At low energies ( $\omega \rightarrow 0$ ), the DOS varies linearly with  $|\omega|$ , resulting in a V-shape spectrum. This linear variation is a result of the excitations at the four nodal points on the Fermi surface along the Brillouin zone diagonals, where superconducting gap order parameter vanishes (see Appendix C for the derivation).

In Figure 4-3(b), we plot the continuum LDOS above a Cu site at a height  $z \approx 5$  Å above the BiO plane. The prominent difference from the lattice LDOS (Figure 4-3(a)) is the U-shaped spectrum at low energies. The change in the low energy spectral features can be understood from both real-space and  $k$ -space perspectives. In the lattice LDOS, only diagonal Green's functions appear, for which the sign of imaginary part is fixed by causality requirements. However, in case of the continuum Greens function, off-diagonal lattice Green's function contributions to Equation 2-18, for which the sign of imaginary part is not fixed, can give rise to a suppressed LDOS at certain energies. Thus the spectral properties of lattice and continuum LDOS can differ. This is explicitly shown in the Figure 4-3(c), where we plot the lattice LDOS (same as in Figure 4-3(a)), the

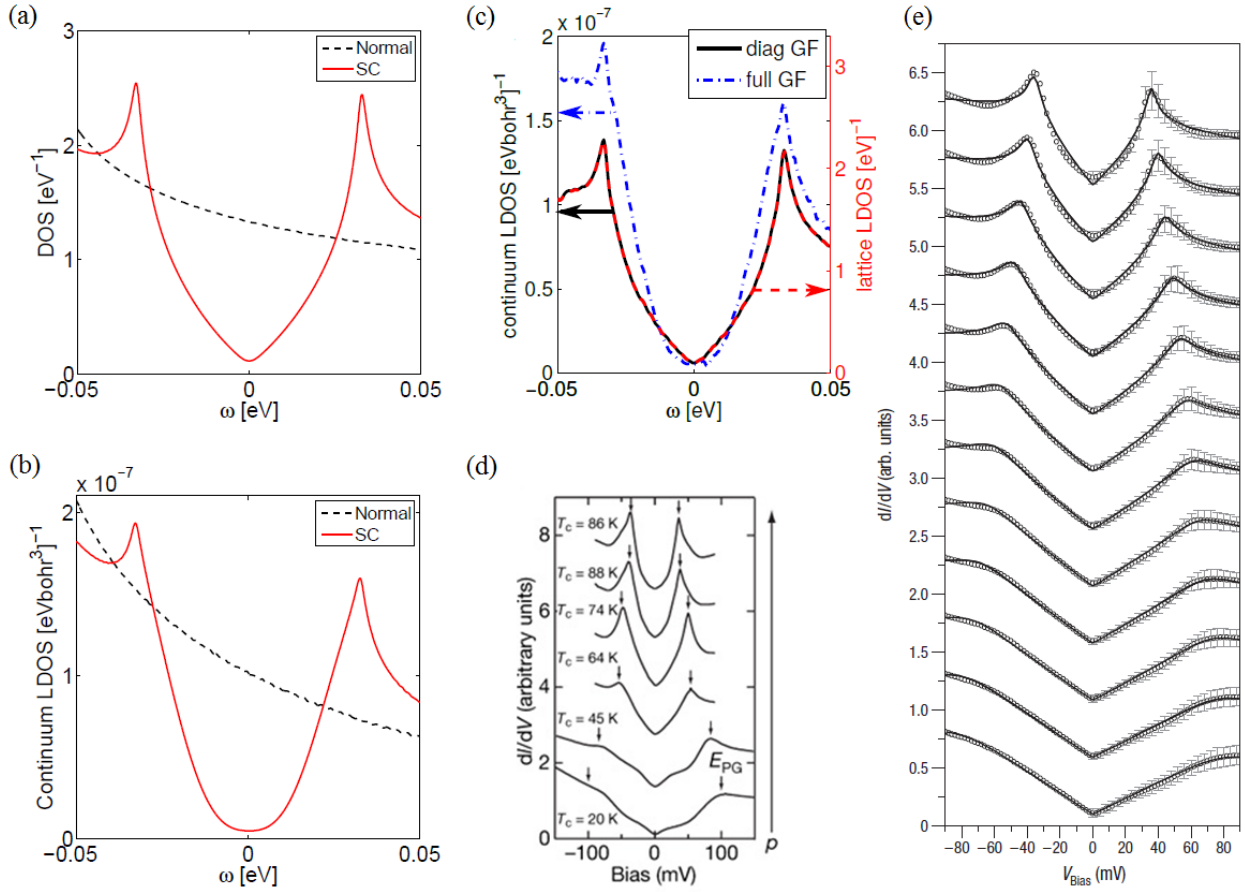


Figure 4-3. (a) Lattice DOS (red solid line) in the homogeneous superconducting state with  $d$ -wave gap compared with the normal state DOS (black dashed line). (b) Continuum LDOS spectrum above a Cu site at height  $z \approx 5 \text{ \AA}$  above the BiO plane in the homogeneous superconducting state (red solid line) and normal state (black dashed line). (c) Lattice DOS (red dashed line), continuum LDOS obtained using full Greens function matrix in Equation 2–18 (blue dashed line), compared with the continuum LDOS calculated using only diagonal Greens function in Equation 2–18 (black solid line). (d) The average conductance spectra in six BSCCO samples with hole doping ranging from under to overdoped regime. Reprinted by permission from Macmillan Publishers Ltd: Nature [125], copyright 2008. (e) Average tunneling conductance spectra in a BSCCO sample in regions with different gap sizes (black circles) and corresponding fits (black solid lines) to a model with  $d$ -wave superconducting gap and a quasiparticle scattering rate varying linearly with energy. Reprinted by permission from Macmillan Publishers Ltd: Nature [126], copyright 2008.

continuum LDOS (same as in Figure 4-3(b)), and also the continuum LDOS where only the diagonal terms of the lattice Greens function have been taken into account. The latter is not a physical quantity, but shows nicely that the resulting continuum LDOS has the same spectral shape as the lattice LDOS because it is just multiplied with the Wannier functions which does not depend on energy. Clearly, the continuum LDOS, with contributions from both diagonal and off-diagonal Greens functions, shows a suppression of the LDOS at  $\omega \rightarrow 0$  when compared with the LDOS with contributions only from the diagonal Greens functions.

A more concrete explanation of the U-shape in the continuum LDOS can be given from the  $k$ -space calculations. The detailed derivation is provided in the Appendix C; here, we will summarize the argument in short. Transforming the basis to momentum space in Equation 2-18, it can be easily shown that the continuum LDOS for a homogeneous system will be given by

$$\rho_\sigma(\mathbf{r}, \omega) = \sum_{\mathbf{k}} A_\sigma(\mathbf{k}, \omega) |W_{\mathbf{k}}(\mathbf{r})|^2. \quad (4-1)$$

Here,  $W_{\mathbf{k}}(\mathbf{r}) = \sum_i w_i(\mathbf{r}) e^{i\mathbf{k} \cdot \mathbf{R}_i}$  is the Fourier transform of the Wannier function, and  $A_\sigma(\mathbf{k}, \omega)$  is the spectral function. If we set  $W_{\mathbf{k}}(\mathbf{r}) = 1$ , then Equation 4-1 will yield the lattice LDOS  $N(\omega)$  which can be shown to vary linearly with  $|\omega|$  as  $\omega \rightarrow 0$  (see Appendix C for a derivation), resulting into the well-known V-shaped spectrum. In case of the continuum LDOS the non-trivial momentum dependence of  $W_{\mathbf{k}}(\mathbf{r})$  changes the low energy shape of the spectrum. At heights several Å above the BiO layer where STM tip would typically reside, the Wannier function above a Cu site is shown in the Figure 4-4. Clearly, the the Wannier function above the central Cu site ( $w_0$ ) is zero, as dictated by the  $d_{x^2-y^2}$ -wave symmetry, and has largest magnitude  $w_1$  above NN sites. Thus, for the continuum position above the Cu site,  $\mathbf{r}_0 = [0, 0, z]$ , at heights  $z$  several Å above the BiO plane,  $\mathbf{k}$ -space Wannier function can be approximated as  $W_{\mathbf{k}}(\mathbf{r}_0) \approx w_0 + 2w_1(\cos k_x - \cos k_y)$ . Although  $w_0 = 0$ , we still keep it to facilitate discussions in the next paragraphs. Now, for

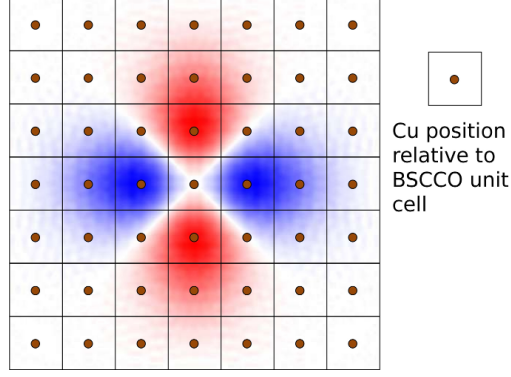


Figure 4-4. Cu- $d_{x^2-y^2}$  BSCCO Wannier function at height  $\approx 5 \text{ \AA}$  above the BiO plane plotted in a  $7 \times 7$   $\text{CuO}_2$  unit cell area. Blue (red) represents positive (negative) sign of the Wannier function value.

$\omega \rightarrow 0$ , performing the momentum space integral results into (see Appendix C for details)

$$\rho_{\sigma}(\mathbf{r}_0, \omega) = a_0|\omega| + a_1|\omega|^3, \quad (4-2)$$

where  $a_0 \propto w_0^2$  and  $a_1 \propto w_1^2$ . Thus, the  $d_{x^2-y^2}$ -wave symmetry results into vanishing linear in  $\omega$  contribution, and a U-shaped spectrum arising from  $\omega^3$  term.

Although it has been never addressed explicitly as far as we know, after doing an extensive literature search, we found that the spectral shape of the measured tunneling current indeed shows some variation, from more V-shape in the optimal-to-underdoped samples to a more U-shape in overdoped samples. In addition, U-shaped spectra have been measured with the same STM tip on samples that show a distribution of gap magnitudes, attributed to local doping concentration [126, 127]. Similar observations have been made in [125, 128–130], but so far not completely understood theoretically. Figure 4-3(d)-(e) show the transition from more V-shaped tunneling conductance to U-shaped spectral dependence when moving from optimally doped samples (sample areas) to overdoped samples where our theory should be applicable. Figure 4-3(d), showing optimal to underdoped samples, is compiled from [125], while Figure 4-3(e) is taken from [126], where the black curve represent a fit of the measured spectra (black circles) to a model with  $d$ -wave superconducting gap and additional quasiparticle scattering rate, and

the different data sets correspond to regions in one sample with different gap sizes. Note that the small-gap (“overdoped”) regions have the more U-shaped curves.

The theoretical picture presented above should be valid only for the weakly-correlated overdoped cuprates where we can safely justify the use of Wannier function obtained from DFT calculations. For optimal-to-underdoped cuprates, the Wannier function shape might change resulting into a V-shaped spectra. In fact, from Equation 4–2 we can easily see that if the Wannier function has non-vanishing weight above the central Cu site, then continuum LDOS has a linear-in- $\omega$  term yielding a V-shaped spectra. Such a scenario will arise when electronic correlations result into a Cu- $d_{z^2}$  contribution to the Fermi surface, a possibility which has been discussed extensively in the literature [131–135], and recently used to explain the variation of  $T_c$  among various cuprate families [136, 137]. However, to make a more concrete statement about the continuum LDOS in underdoped cuprates, we must systematically study the evolution of the Wannier function with increasing electronic correlations [138–140] which we leave for a future project. Another promising scenario which can explain the V-shaped continuum LDOS spectra in underdoped cuprates is the coexistence of charge order. In Section 5.3.2, we show that a particular charge ordered phase coexisting with superconductivity results into a V-shaped continuum LDOS spectra, very similar to that observed in the STM experiments on underdoped cuprates.

#### 4.4 Effects of a Strong Non-Magnetic Impurity

We model the Zn impurity replacing the Cu atom as a strong point-like potential scatterer with  $V_{\text{imp}} = -5$  eV, very similar to the value found in our first-principles calculations. BdG equations (Equation 2–9 and 2–10) were solved self-consistently on a  $35 \times 35$  square lattice with impurity in the middle. Subsequently, the lattice Green’s function matrix was constructed using  $20 \times 20$  supercells. Figure 4-5(a) shows the lattice LDOS spectrum at a far away site, at the impurity site, and the NN site, calculated using Equation 2–13. The LDOS is heavily suppressed at the impurity site as expected given that the impurity potential is much larger than the bandwidth. A sharp in-gap resonance

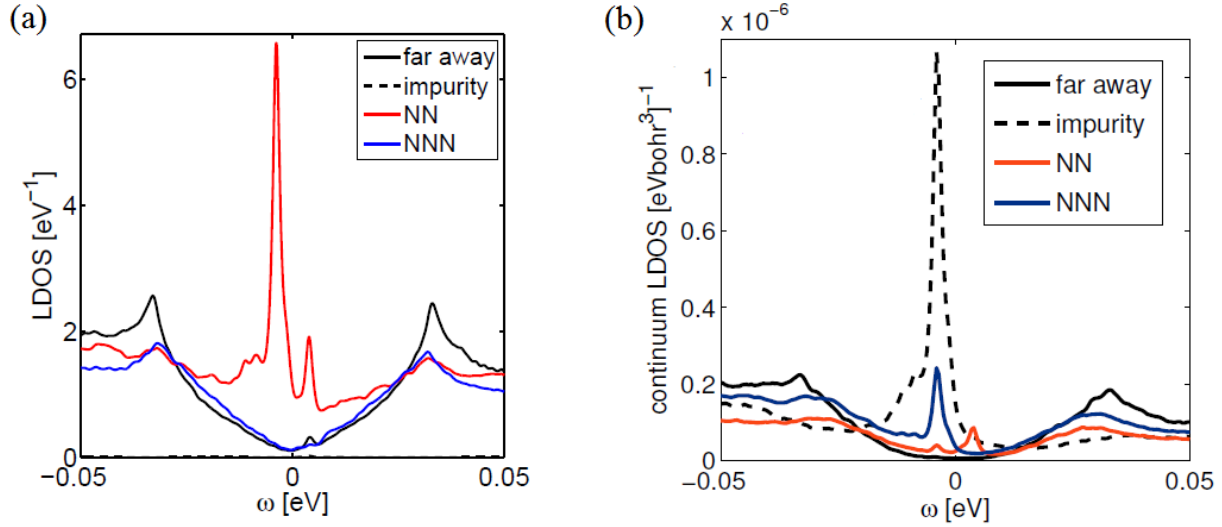


Figure 4-5. (a) Lattice LDOS spectrum around Zn impurity modeled by a strong on-site potential  $V_{\text{imp}} = -5$  eV. Spectrum calculated using  $20 \times 20$  supercells with artificial broadening of 1 meV, at the impurity site, nearest neighbor site, next nearest neighbor site, and a site far away from the impurity, are shown in dashed black, red, blue, and solid black, respectively. (b) Continuum LDOS spectrum at a height  $z \approx 5$  Å above the BiO surface. Shown are positions directly above a Cu atom far from impurity (black, solid line), at the impurity (black, dashed line), on the nearest neighbor position (red, solid line), and on the next-nearest neighbor position (blue, solid line). Results are to be compared with the experimental result of Ref. [60], shown in Figure 1-7(a).

state at  $\Omega = \pm 3.6$  meV is clearly observed in the LDOS spectrum at the NN site with strongly electron-hole asymmetric weights. This is in contrast with the experimental observation [60] of resonance peak right above the impurity site. The spatial pattern of the resonance state is more clear in the lattice LDOS map at  $\Omega = -3.6$  meV shown in Figure 4-6(a). This discrepancy between theory and the experiment has arisen because we are comparing lattice LDOS evaluated at the Cu sites with the STM conductance map obtained few Å above the exposed BiO layer. As explained in Section 2.3, the right quantity to compare with the STM result is the continuum LDOS  $\rho(\mathbf{r}, \omega)$  evaluated at the STM tip position. Indeed, we find that the continuum LDOS computed at a height  $z \approx 5$  Å from BiO plane, where STM tip would be typically placed, displays excellent agreement with the experiment as evident from comparing Figure 4-6(b) and (c). In addition to

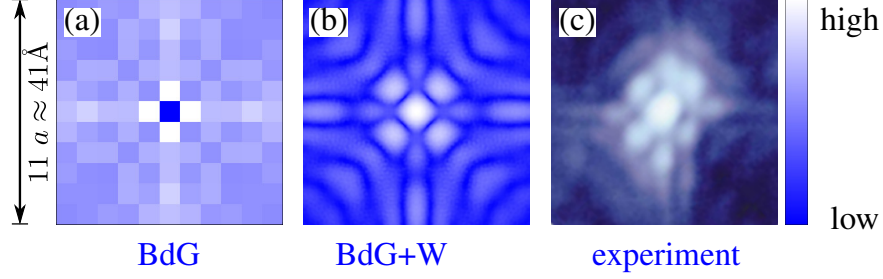


Figure 4-6. (a) Lattice LDOS map at the resonant energy  $\Omega = -3.6$  meV computed from BdG solutions using Equation 2-13. Each pixel represent a Cu site. (b) Continuum LDOS map at the same energy, and at a height  $z \approx 5$  Å above BiO plane computed using Equation 2-14. (c) STM conductance map at the impurity resonance energy rotated to match the orientation in (b) and (c), and cropped to  $11 \times 11$  unit cells. Impurity is located at the center. Reprinted by permission from Macmillan Publishers Ltd: Nature [60], copyright 2000.

the LDOS maximum above the impurity site and sub-maximum above the NNN site (see also Figure 4-5(b)), the continuum LDOS map at  $\Omega = -3.6$  meV also captures the long-range intensity tails oriented along Cu-O direction as seen in the experiment [60]. Thus, BdG+W approach captures all qualitative features of the Zn-impurity induced states in BSCCO as seen in the STM experiments. In Appendix D, we show that the phenomenological "filter" theory [62], described in Section 4.1, can be obtained as a first-order approximation of the BdG+W equations.

#### 4.5 Effects of a Magnetic Impurity

As shown in the Figure 4-7(a), the STM experiments on Ni-doped BSCCO [64] found two spin-resolved in-gap virtual bound states at energies  $\pm\Omega_{1,2}$  in the vicinity of the Ni atoms substituting Cu atoms. Impurity-induced resonance peaks were observed to be particle-like at the impurity site and next nearest neighbor sites, and hole like at the nearest neighbor sites. The spatial patterns at  $+\Omega_{1,2}$  resembled cross-shaped and X shaped at  $-\Omega_{1,2}$ . Observation of these resonance states is consistent with the models of combined potential and magnetic scattering of quasiparticles in a *d*-wave superconductor [122]. However, like the case of Zn, spatial patterns deviate from the predictions.

A magnetic impurity acts as the source of potential as well as magnetic scattering, and can be simply modeled by following Hamiltonian [68, 75].

$$H_{\text{imp}} = \sum_{j\sigma} U_{i^*j} c_{i^*\sigma}^\dagger c_{j\sigma} + \sum_{j\sigma} \sigma J_{i^*j} c_{i^*\sigma}^\dagger c_{j\sigma} + \text{H.c.}, \quad (4-3)$$

where  $\sigma = \pm 1$ , and H.c. refers to the Hermitian conjugate. The first term in the above Hamiltonian accounts for the potential scattering at the impurity site  $i^*$  and  $U_{i^*j}$  is the impurity potential which can be written as  $U_0 \delta_{i^*j}$ , where  $\delta$  represents the Kronecker delta function, for a completely local impurity model. The second term in the above Hamiltonian accounts for the magnetic scattering due to exchange interaction between impurity magnetic moment, approximated as a classical object, and conduction electrons.  $J_{i^*j}$  represents the extended exchange coupling which can be expressed as  $J_0 \delta_{i^*j}$  for the special case of completely local exchange interaction. The BdG equations described in Section 2.2.2 can be easily generalized to study the magnetic impurity modeled by Equation 4-3 by making following modifications to the BdG matrix elements

$$\begin{aligned} \xi_{ij\uparrow} &= t_{ij} - \mu_0 \delta_{ij} - (U_0 + J_0) \delta_{i^*j} \delta_{ij}, \\ \xi_{ij\downarrow} &= t_{ij} - \mu_0 \delta_{ij} - (U_0 - J_0) \delta_{i^*j} \delta_{ij} \end{aligned} \quad (4-4)$$

Ni is known to be a weaker impurity than Zn as it does not disrupt superconductivity in its vicinity, and the pure magnetic scattering is thought to be sub-dominant to the pure potential scattering [64]. Accordingly, in the simplest scenario, we model Ni as completely local impurity, with on-site potential  $U_0 = 0.6$  eV and exchange coupling  $J_0 = 0.3U_0$ , and solve the BdG equations on a  $35 \times 35$  lattice. The values of  $U_0$  and  $J_0$  have been chosen just to clearly demonstrate the spin-splitting of impurity-induced resonance peaks due to on-site magnetic scattering. We note that in this simple model, it is not possible to obtain sharp resonance peaks close to the gap edge as seen in the experiment (Figure 4-7(a)) [75]. Figure 4-7(b) shows the lattice LDOS spectrum, computed with  $20 \times 20$  supercells, at different sites around such impurity. Resonance peaks at  $\pm\Omega'_1 = 2.6$  meV

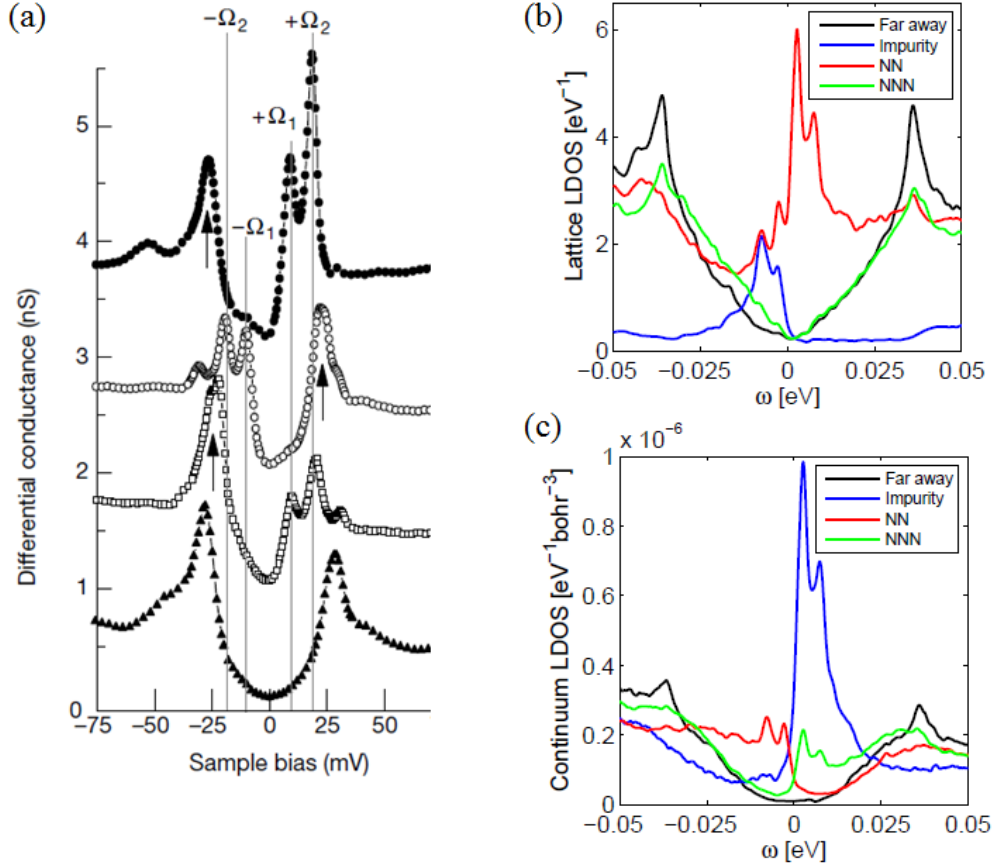


Figure 4-7. (a) Differential tunneling conductance spectra above the Ni atom site substituting for a Cu site in BSCCO (solid circles), above the first nearest neighbor Cu atom position (open circles), above the second nearest neighbor Cu atom (squares), and a typical spectrum far from the Ni atom (triangles). Impurity induced resonance peaks are observed at  $\pm\Omega_1 = 9$  meV and  $\pm\Omega_2 = 19$  meV. Reprinted by permission from Macmillan Publishers Ltd: Nature [64], copyright 2001. (b) Lattice LDOS spectrum around a magnetic impurity with on-site potential  $U_0 = 0.6$  eV and on-site exchange coupling  $J_0 = 0.3U_0$ . Spectrum calculated using  $20 \times 20$  supercells with artificial broadening of 1 meV, at the impurity site, nearest neighbor site, next-nearest neighbor site, and a site far away from the impurity, are shown in blue, red, green and black, respectively. (c) Continuum LDOS spectrum at a height  $z \approx 5$  Å above the BiO surface. Shown are positions directly above a Cu atom far from impurity (black), at the impurity (blue), on the nearest neighbor position (red), and on the next-nearest neighbor position (green).

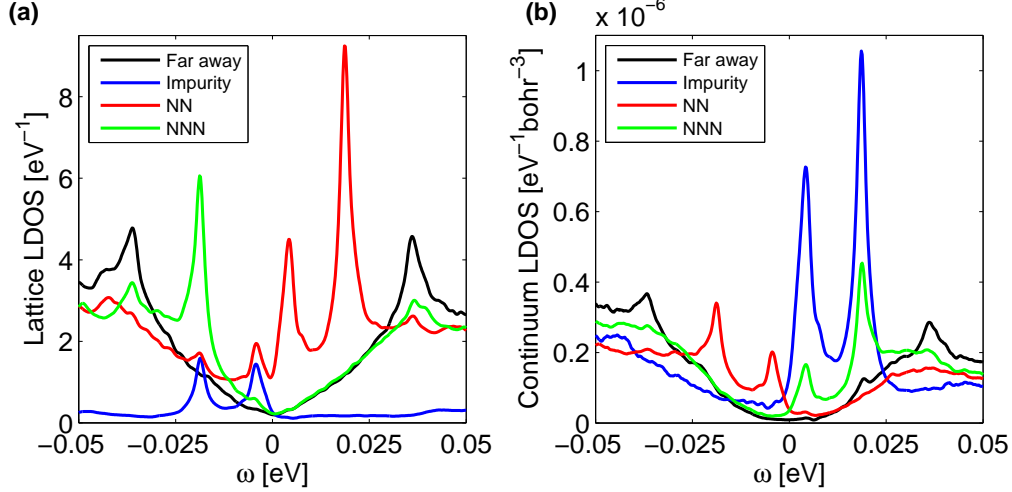


Figure 4-8. (a) Lattice LDOS spectrum around a magnetic impurity with on-site potential  $U_0 = 0.6$  eV, nearest-neighbor potential  $U_{NN} = 0.3$  eV, and nearest-neighbor exchange coupling  $J_{NN} = U_{NN}$ . Spectrum calculated using  $20 \times 20$  supercells with artificial broadening of 1 meV, at the impurity site, nearest neighbor site, next-nearest neighbor site, and a site far away from the impurity, are shown in blue, red, green and black, respectively. (b) Continuum LDOS spectrum at a height  $z \approx 5$  Å above the BiO surface. Shown are positions directly above a Cu atom far from impurity (black), at the impurity (blue), on the nearest neighbor position (red), and on the next-nearest neighbor position (green).

and  $\pm\Omega'_1 = 7.6$  meV are easily observed in the LDOS spectrum at the impurity site and its nearest neighbor (NN); however, spectrum at the next nearest neighbor (NNN) site simply follows the bulk LDOS spectrum. Resonance peaks at  $+\Omega'_1$  and  $-\Omega'_2$  have down-spin polarization whereas those at  $+\Omega'_2$  and  $-\Omega'_1$  have up-spin polarization. In absence of magnetic scattering, resonance peaks are spin degenerate. A small on-site exchange coupling  $J_0$  lifts this degeneracy as the effective impurity potential experienced by electrons becomes spin dependent,  $V_{\text{imp}}^{\text{eff}} = U_0 + \sigma J_0$ , and leads to two spin polarized in-gap resonance states.

Figure 4-7(c) shows the continuum LDOS spectrum in a plane located at  $z \approx 5$  Å above BiO plane, at positions which are directly above the impurity, NN site, NNN site, and a distant site. Similar to the STM results [64] continuum LDOS shows double peak structure at negative (positive) energies at the positions directly above NN site (impurity and NN sites). Note that this trend is completely missing in the lattice LDOS spectrum

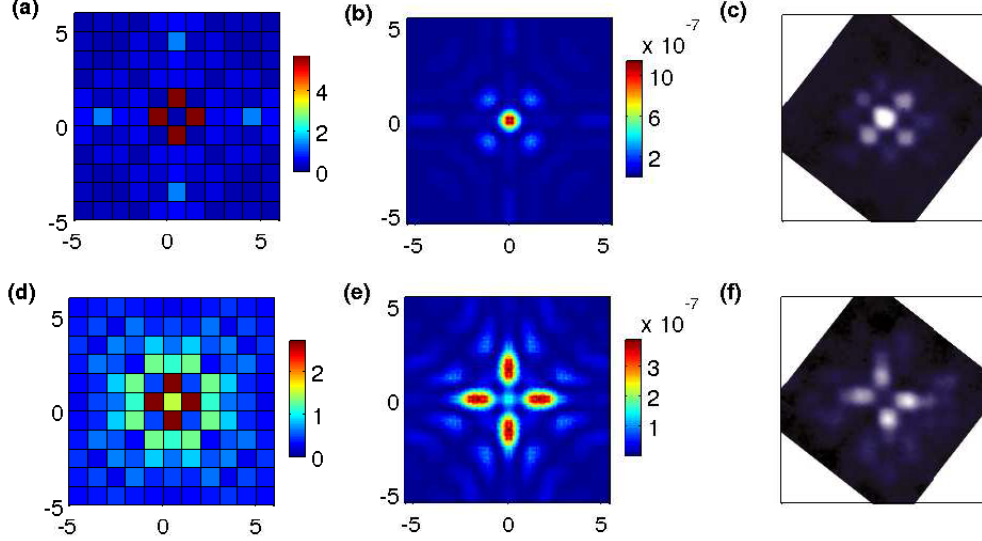


Figure 4-9. (a), (d) Lattice LDOS map around the magnetic impurity in a region comprising  $11 \times 11$  unit cells, at the resonant energies  $\pm\Omega'_1 = 2.6$  meV. Colorbar values are in the units of  $\text{eV}^{-1}$ . (b), (e) Continuum LDOS maps at  $\pm\Omega'_1$  and  $z \approx 5$  Å above BiO plane with same area as in (a) and (d). Colorbar values are in the units of  $\text{eV}^{-1}\text{bohr}^{-3}$ . (c), (f) STM conductance maps at  $\pm\Omega_1 = 9$  meV rotated to match the orientation in (b) and (c), and cropped to  $11 \times 11$  unit cells with the impurity located at center. Reprinted by permission from Macmillan Publishers Ltd: Nature [64], copyright 2001.

(Figure 4-7(b)). Although the splitting of peaks due to magnetic scattering is captured in this simple model of a point-like impurity, a careful comparison with the experimental conductance spectrum shown in the Figure 4-7(a) shows that the relative heights of the peaks are reversed. In the simple on-site impurity model, the height of the resonance peak decreases and width increases as it moves away from the mid-gap due to increasing hybridization between bulk and impurity states [75]. Thus the experimentally observed relative peak heights can not be explained by such model. To this end, we find that an extended impurity model with on-site potential  $U_0 = 0.6$  eV, NN potential  $U_{NN} = 0.3$  eV, and NN exchange coupling  $J_{NN} = U_{NN}$  can lead to the desired trend. This impurity model yields sharp resonance peaks at  $\pm\Omega''_1 = 4.2$  meV and  $\pm\Omega''_2 = 18.6$  meV in the lattice and continuum LDOS spectrum as shown in Figure 4-8(a) and (b), respectively. Resonance peaks at  $+\Omega''_1$  and  $-\Omega''_2$  ( $+\Omega''_2$  and  $-\Omega''_1$ ) are found to have up (down) spin

polarization. Clearly, resonance peaks at  $\pm\Omega_2''$  are higher than those at  $\pm\Omega_1''$ . Moreover, similar to the experiment and also to the case of on-site impurity model, continuum LDOS shown in Figure 4-8(b) displays switching of resonance peaks from positive to negative biases and then back to positive biases as one moves from impurity to NN and then to NNN sites. Thus, the extended impurity model captures most of the features of STM results [64]; however, the microscopic origin of such a model still needs to be investigated.

Now, we turn to the spatial LDOS maps at the resonance energies for the point-impurity model. The LDOS maps for the extended impurity model is found to be qualitatively the same. Figure 4-9(a) shows the lattice LDOS map at  $\omega = +\Omega_1'$  around an impurity in a region comprising  $11 \times 11$  unit cells. The vanishing LDOS at the impurity site and maximum at the NN site observed here is completely opposite to the experimental conductance map at  $\omega = +\Omega_1$  reproduced in Figure 4-9(c). However, the continuum LDOS map  $\rho(\mathbf{r}, +\Omega_1')$ , at a height  $z \approx 5 \text{ \AA}$  above BiO plane, shown in Figure 4-9(b) compares very well with the experiment. A similar trend holds at the negative energy resonance peak. The continuum LDOS map at  $\omega = -\Omega_1'$  shown in Figure 4-9(e) shows excellent agreement with the experimental conductance map at  $\omega = -\Omega_1$  reproduced in Figure 4-9(f). The continuum LDOS maps at  $\omega = +\Omega_2'$  ( $-\Omega_2'$ ) is found to be very similar to that at  $\omega = +\Omega_1'$  ( $-\Omega_1'$ ).

## 4.6 Quasiparticle Interference

The STM experiments can provide momentum-space information about the energy dispersion in a material via the Fourier transform spectroscopy or quasiparticle interference (QPI). The basic concept behind QPI is the Friedel oscillation: A defect in otherwise homogeneous metal scatters electrons elastically from the Bloch state  $\mathbf{k}_1$  to  $\mathbf{k}_2$  resulting into oscillations in the local density with wavevector  $\mathbf{q} = \mathbf{k}_1 - \mathbf{k}_2$ ;  $q = 2k_F$  where  $k_F$  is the Fermi momentum. Such oscillations can be observed in the STM tunneling conductance in an energy-resolved way, and Fourier transformation of real-space

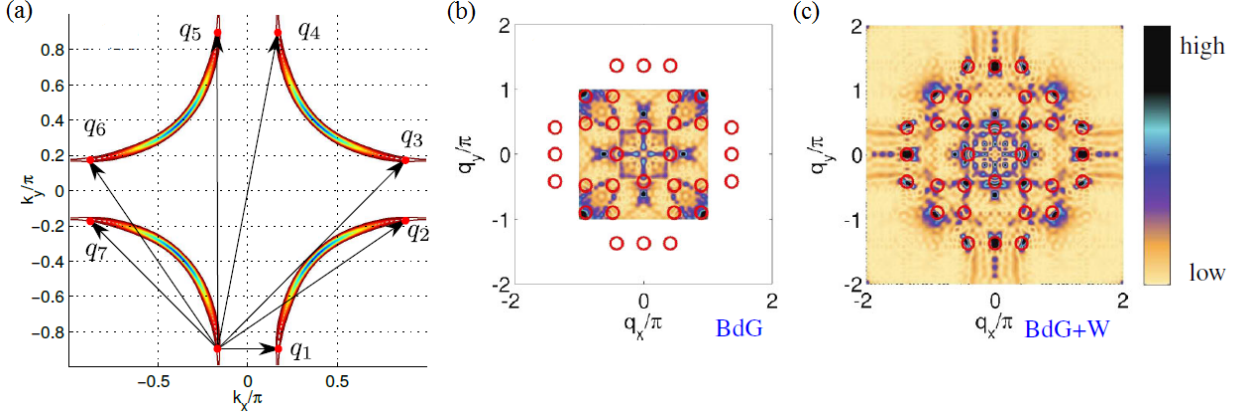


Figure 4-10. (a) Isoenergy contours for quasiparticle energy  $E_{\mathbf{k}}$  in the  $d$ -wave homogeneous superconducting state obtained within our model. QPI patterns obtained by Fourier transform of the (b) lattice DOS (BdG) (c) continuum LDOS (BdG+W) obtained at  $\omega = 24$  meV for a weak impurity modeled with on-site potential  $V_{\text{imp}} = 0.3$  eV.

conductance maps yield the dispersion  $\mathbf{q}(\omega)$  from which important information about the homogeneous system can be extracted [141, 142].

In the cuprate superconducting state where the quasiparticle band structure is highly anisotropic, QPI patterns have been understood in terms of the so called 'octet model' [93]. Due to elastic scattering at defects, the wavevectors which appear in QPI pattern at a bias  $V = \omega/e$  must correspond to the vectors connecting two points on the isoenergy contour  $\mathbf{k}(\omega)$ . For superconducting cuprates with a dispersion  $E_{\mathbf{k}} = \sqrt{\xi_{\mathbf{k}}^2 + \Delta_{\mathbf{k}}^2}$  where  $\xi_{\mathbf{k}}$  is the band energy relative to the Fermi energy and  $\Delta_{\mathbf{k}}$  is the  $d$ -wave superconducting gap order parameter, the isoenergy contours form "banana-like" shapes as shown in Figure 4-10(a). Moreover, the eight points corresponding to the tips of the bananas at a given bias have largest DOS, hence the scattering processes connecting these tips should have largest probability resulting into large QPI signals at the corresponding wavevectors. The seven wavevectors  $\mathbf{q}_1$  to  $\mathbf{q}_7$  from one of the eight points are shown in Figure 4-10(a).

The impurities which cause QPI in BSCCO are believed to be the native defects like out-of-plane oxygen interstitials, and Bi-Sr site-switching. We model such defects by weak point-like impurities with on-site potential  $V_{\text{imp}} = 0.3$  eV and obtain lattice

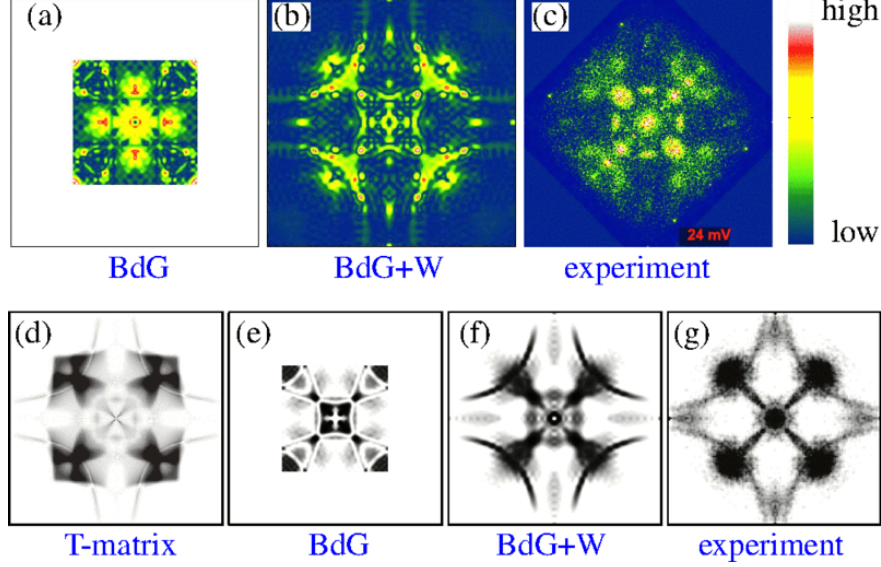


Figure 4-11. QPI Z-maps obtained at  $\omega = 24$  meV using (a) lattice DOS (BdG) (b) continuum LDOS (BdG+W) (c) STM experiment [143]. Energy integrated  $\Lambda$ -maps obtained from (d) lattice LDOS using T-matrix method [143], (e) lattice LDOS using BdG calculation, (f) continuum LDOS using BdG+W approach, and (g) STM experiment. (c), (d), and (g) are reproduced from [143]. Reprinted with permission from AAAS.

and continuum LDOS following a procedure very similar to that outlined in Section 4.4. Subsequently, we Fourier transform the lattice and continuum LDOS maps to find the QPI patterns. Corresponding results for bias  $\omega = 24$  meV are shown in Figure 4-10(b) and (c), respectively. Since the lattice LDOS information is available only for lengths larger than the lattice constant  $a$ , the QPI pattern obtained from lattice LDOS shows wavevectors only in the first Brillouin zone  $[-\pi/a, \pi/a]$ , thus, when compared with the octet model predictions (shown by red circles) only few wavevectors are reproduced. However, the experimental patterns have no such restrictions, and QPI signals are observed in higher Brillouin zones too. The QPI pattern obtained from the continuum LDOS show a much better agreement with the octet model where all  $\mathbf{q}$  vectors are captured due to availability of the intra-unit cell LDOS information.

For a closer comparison with the experimental QPI patterns we follow [143], and compute the Fourier transform of Z-maps  $Z(\mathbf{q}, \omega)$  and the energy integrated map  $\Lambda(\mathbf{q})$

defined as

$$Z(\mathbf{q}, \omega) = FT[Z(\mathbf{r}, \omega)] = FT \left[ \frac{\rho(\mathbf{r}, \omega)}{\rho(\mathbf{r}, -\omega)} \right] \quad (4-5)$$

$$\Lambda(\mathbf{q}) = \int_0^{\Delta_0} d\omega Z(\mathbf{q}, \omega), \quad (4-6)$$

where  $FT$  represents the Fourier transform. Figure 4-11(a) and (b) show the QPI Z-maps at  $\omega = 24$  meV obtained from lattice LDOS and continuum LDOS, respectively. Clearly, the latter shows a much better agreement with the experimental map at the same bias shown in Figure 4-11(c). Particularly, the arc-like feature (reminiscent of the Fermi surface) near  $\mathbf{q} = [\pm\pi, \pm\pi]$  and relative intensity at different  $\mathbf{q}$  vectors compare very well with the experimental plot. The  $\Lambda(\mathbf{q})$  map calculated from the lattice LDOS obtained using T-matrix method [143] and BdG method, continuum LDOS obtained from our BdG+W method, and the corresponding experimental result [143] are shown in figures 4-11(d),(e),(f), and (g), respectively. When compared with the experimental result, it can be easily observed that the BdG+W method demonstrates a qualitative improvement over the T-matrix and BdG-only methods used previously [144–151] to study the QPI patterns.

## 4.7 Conclusion

In this chapter, we used the BdG+W scheme to study the impurity induced states in Zn- and Ni- doped BSCCO, a cuprate superconductor that has been widely studied in STM and ARPES experiments. We started with a 1-band tight-binding model and corresponding Cu- $d_{x^2-y^2}$  Wannier function derived from the first principles calculations. Subsequently,  $d$ -wave superconductivity was introduced "by hand" via NN pair-potentials with magnitude chosen to yield the spectral gap observed in STM experiments [57, 60] on optimally-doped BSCCO. We showed that the continuum LDOS spectrum above a Cu site obtained at a height  $z \approx 5 \text{ \AA}$  above the BiO plane, where an STM tip would be typically placed, shows a more U-shape like feature at low energies in contrast to the well-known V-shaped spectrum of the lattice DOS. We showed that this change in the low energy spectral features is a direct consequence of the  $d_{x^2-y^2}$ -symmetry of the Wannier

function. Furthermore, we mentioned few experimental evidences of U-shaped spectra in the overdoped region of the cuprate phase diagram where our theory should be valid and presented some scenarios which can lead to the transition to a V-shaped spectra going from over-to-underdoped regime. Then we studied the Zn impurity problem in BSCCO by modeling Zn, based on ab initio calculations, as a strong, attractive, point-like potential scatterer substituting a Cu atom. By solving the BdG equations on a large square lattice, we found that it induces sharp in-gap bound states as expected from previous theoretical and numerical works [68, 75]. More importantly, by calculating the continuum LDOS within BdG+W framework, we resolved the long-standing discrepancy between theoretical predictions of the impurity induced spatial patterns [61] of the LDOS and corresponding STM observations [60]. We showed that the continuum LDOS obtained at a typical STM tip height above the BiO plane displays excellent agreement with the experiment [60], and the intensity maximum above the impurity sight can be easily explained by accounting for the tails of Cu  $d_{x^2-y^2}$  Wannier function tails with significant weight coming from the apical oxygen atoms in the nearest neighbor unit cells. Next, we studied the Ni impurity problem in BSCCO by using a simple model of magnetic impurity with weak on-site potential and exchange scattering, and showed that such an impurity induced two spin-polarized in-gap resonance states as predicted by earlier theories [122]. Moreover, the continuum LDOS maps at the resonance energies, computed at typical STM tip height displays excellent agreement with the corresponding STM results [64]. Furthermore, we proposed an extended impurity model to explain the relative resonance peak heights as observed in the experiment. Finally, we showed that the QPI patterns obtained using the Fourier transform of the continuum LDOS maps demonstrated a qualitative improvement over the T-matrix or BdG results, capturing nearly all wavevectors predicted by the octet model, and showed an excellent agreement with the STM experiments [143].

## CHAPTER 5 CHARGE ORDER IN CUPRATES

In this chapter, I will discuss the charge ordered states in the extended  $t - J$  model for underdoped cuprates. Most of the material presented here is based on a published paper [152]. All the published contents (excerpts and figures) are reprinted with permission from Peayush Choubey, Wei-Lin Tu, T. K. Lee, and P. J. Hirschfeld, *New J. Phys.* **90**, 013028 (2017), copyright 2017 by the Institute of Physics Publishing.

### 5.1 Motivation

The charge order (CO) or charge density wave (CDW) state refers to a translational symmetry broken phase where the electronic charge density forms a modulating structure with a periodicity different from the underlying lattice. First predicted by Rudolf Peierls [153] as an instability of one-dimensional (1D) metals, CO has been observed in variety of materials such as quasi 1D [154, 155] and 2D [156] organic compounds, transition-metal chalcogenides [155] and oxides [157–159]. The Fermi surface driven mechanism of CDW formation in quasi 1D metals is explained in Figure 5-1. The perfect Fermi surface nesting at the wavevector  $q = 2k_F$  leads to a diverging charge susceptibility at the same wavevector, which in turn makes the electron gas unstable with respect to formation of a modulating electron density with periodicity  $\lambda_0 = \frac{\pi}{k_F}$ . The cost of Coulomb repulsion can be overcome by the opening of a gap at the Fermi level. If the periodicity of the charge density happens (not) to be an integer multiple of the lattice constant then the CDW state is called commensurate (incommensurate).

In cuprates, the first observation of charge order occurred in the form of "stripe order" [37, 161–163] through neutron scattering experiments on the La-based cuprates  $\text{La}_{2-x}\text{Ba}_x\text{CuO}_4$  and  $\text{La}_{2-x-y}\text{Nd}_y\text{Sr}_x\text{CuO}_4$  [164, 165]. Stripe order refers to a state characterized by a combination of a unidirectional, incommensurate CDW and a spin density wave (SDW), where the wavelength of the latter is twice of the former, i.e.  $\lambda_{SDW} = 2\lambda_{CDW}$ . The most prominent effects of the stripe order are observed around

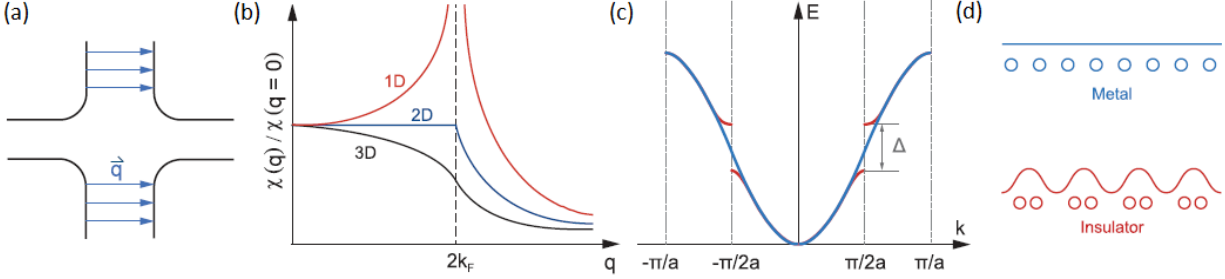


Figure 5-1. (a) Schematic of the Fermi surface of a quasi 1D metal, illustrating nesting at the wavevector  $\mathbf{q}$ . (b) The charge susceptibility  $\chi(\mathbf{q})$  of the free electron gas in one, two, and three dimensions as a function of  $\mathbf{q}$ . In 1D  $\chi(q)$  diverges at  $q = 2k_F$ , where  $k_F$  is the Fermi momentum, making the system susceptible to charge ordering. (c) Dispersion of 1D electron gas before (after) the Peierls transition shown in blue (red). Energy gap  $\Delta$  opens up at  $q = 2k_F$ . (d) Uniform (modulating) electron density before (after) the Peierls transition. Reprinted from [160]. Copyright IOP Publishing. Reproduced with permission.

hole doping of  $x = 1/8$ , where stripes show a commensurate nature with  $\lambda_{CDW} = 4a_0$  [164],  $a_0$  being the in-plane lattice constant. The  $T_c$  is observed to be strongly suppressed, indicating a competition between the stripe phase and  $d$ -wave superconductivity [166]. Moreover, the stripe wavevector is observed to increase with increasing hole doping [36]. Apart from the La-based family, there is little evidence of similar stripe order in other cuprates. Instead, a unidirectional incommensurate charge order, without any accompanying magnetic order, is observed in variety of cuprates such as  $\text{YBa}_2\text{Cu}_3\text{O}_{6+x}$  (YBCO) [34, 167, 168],  $\text{Bi}_2\text{Sr}_2\text{CaCu}_2\text{O}_{8+x}$  (BSCCO) [35, 142],  $\text{Bi}_2\text{Sr}_{2-x}\text{La}_x\text{CuO}_{6+\delta}$  (LaBSCCO) [169],  $\text{HgBa}_2\text{CuO}_{4+\delta}$  (HBCO) [170, 171], and  $\text{Na}_x\text{Ca}_{2-x}\text{CuO}_2\text{Cl}_2$  (NaCCOC) [35], using a range of experimental techniques like nuclear magnetic resonance (NMR) [34, 172], STM [35, 169, 173–175], X-ray diffraction [168, 176], and resonant X-ray scattering [36, 167, 177, 178]. In most of these compounds, the charge ordering wavevector is found to decrease with increasing hole doping [36], a trend opposite to that in stripe ordered cuprates. In STM experiments, charge order appears as domains of unidirectional conductance modulations with short coherence lengths ( $\approx 30 \text{ \AA}$  [36]) as shown in Figure 5-2(a). The modulations are most prominent on O sites, as reflected in Figure 5-2(b). In

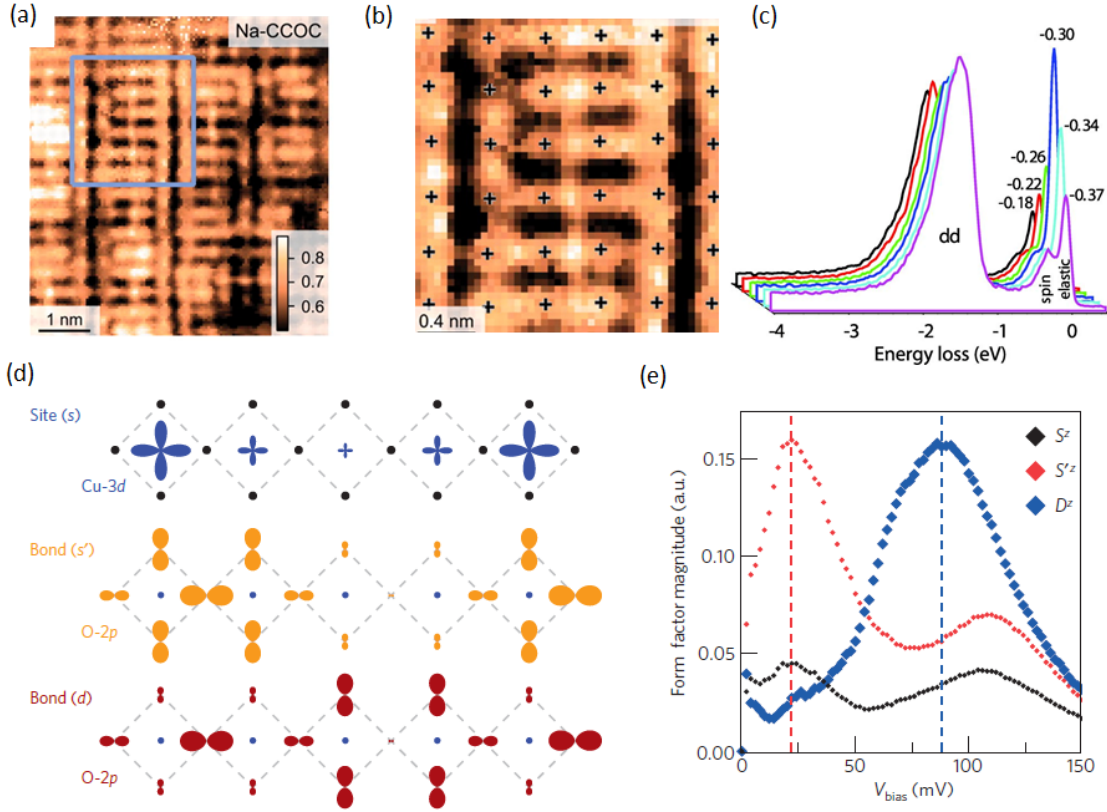


Figure 5-2. (a) The STM R-map (ratio of tunneling current maps at bias  $\pm V$ ) of 12% hole-doped NaCCOC taken at  $V = 150$  mV and  $T = 4.2$  K. (b) Zoomed-in view of the R-map in the area bounded by the blue square in (a). The locations of Cu atoms are marked by cross. Density modulations are very weak on Cu sites and strong on O sites. Both figures are from [35]. Reprinted with permission from AAAS. (c) Resonant X-ray scattering measurements in underdoped  $\text{Nd}_{1.2}\text{Ba}_{1.28}\text{Cu}_3\text{O}_7$  showing quasi-elastic peak at  $\mathbf{q} \sim [-0.31, 0]$  in reciprocal lattice units, as a signature of the unidirectional charge order at the same wavevector  $\mathbf{q}$ . Reprinted from [167] with permission from AAAS. (d) Schematic representation of charge density modulations on Cu and O sites in the charge ordered states with pure  $s$ -,  $s'$ -, and  $d$ -form factor, respectively. Reprinted by permission from Macmillan Publishers Ltd: Nature [179], copyright 2015. (e) STM determined bias dependence of form factors in 8% hole-doped BSCCO at  $T = 4.2$  K. Reprinted by permission from Macmillan Publishers Ltd: Nature [66], copyright 2015.

resonant X-ray scattering experiments, charge order is identified by the appearance of a quasi-elastic peak in the photon energy loss spectrum at a particular momentum  $\mathbf{q}$  parallel to the Cu-O bond direction [36]. For example, in  $\text{Nd}_{1.2}\text{Ba}_{1.28}\text{Cu}_3\text{O}_7$  [167], such a peak is observed at  $\mathbf{q} \sim [-0.31, 0]$  (in reciprocal lattice units) as shown in Figure 5-2(c).

Another intriguing property of the aforementioned charge order is its intra-unit cell symmetry. By taking the intra-unit cell degrees of freedom corresponding to the O- $p_x$ , O- $p_y$ , and Cu- $d_{x^2-y^2}$  orbitals into account, the CDW order parameter  $\Delta_{CDW}(\mathbf{k}, \mathbf{Q}) = \langle c_{\mathbf{k}+\mathbf{Q}/2}^\dagger c_{\mathbf{k}-\mathbf{Q}/2} \rangle$ , with  $\mathbf{Q}$  being the ordering wavevector, can be represented as a linear combination of three components [36, 179, 180]

$$\Delta_{CDW}(\mathbf{k}, \mathbf{Q}) = \Delta_s + \Delta_{s'}(\cos k_x + \cos k_y) + \Delta_d(\cos k_x - \cos k_y) \quad (5-1)$$

The first term corresponds to a pure  $s$ -form factor CDW with amplitude  $\Delta_s$  where charge modulation occurs only at the Cu- $d_{x^2-y^2}$  orbital. The second and third terms correspond to  $s'$ - and  $d$ -form factor CDW states, respectively, where charge modulation occurs only at the O- $p_x, p_y$  orbitals. In former (latter) the modulations on O- $p_x$  and O- $p_y$  orbitals are in-phase (out of phase). The schematic representation of these form factors is shown in the Figure 5-2(d). The STM experiments on the superconducting underdoped BSCCO [35, 65, 175] and NaCCOC [35, 65] reveal that the dominant charge modulation occurs at the O sites with a  $\pi$  phase difference between the two inequivalent O atoms resulting into a dominant  $d$ -form factor (see Figure 5-2(b)). Moreover, the resonant x-ray scattering experiments [179] on LaBSCCO and YBCO conclude the same. Taking a step further, Hamidian et al [66] mapped the bias dependence of form factors using a phase-resolved Fourier analysis [65] of real-space STM data with intra-unit cell resolution. The result is reproduced in Figure 5-2(e). At low energies, the  $s'$ -form factor dominates, whereas at higher energies the  $d$ -form factor has the largest weight with peak around the pseudogap energy scale. Moreover, in the range where the  $d$ -form factor dominates, the conductance maps above and below Fermi energy display a spatial phase difference of  $\pi$ . Furthermore, using Josephson tunneling spectroscopy [181], the same group has reported the observation of pair density waves - a state with spatially modulating superconducting gap order parameter [182].

Theoretically, charge order in cuprates has been studied from both the itinerant and localized perspectives. In the weak-coupling treatment of the itinerant spin-fermion model [183], a  $d$ -form factor charge order arises as consequence of the instability in the charge channel caused by strong antiferromagnetic spin-fluctuations at the wavevectors connecting the hot-spots on the Fermi surface [180, 184–187]. All such calculations except [185] find the ordering wavevector to be oriented along the Brillouin zone diagonal,  $45^\circ$  away from the experimentally observed direction [36]. Wang et al. [185] found the correct orientation of the wavevector but a strong-coupling Eliashberg like treatment of their model resulted in a strong suppression of the charge order along these wavevectors [188].

From the localized perspective of "doping a Mott insulator" [24], the charge order in cuprates has been extensively studied using  $t - J$  type models [24, 29, 30] through a variety of techniques such as Gutzwiller mean-field theory [189, 190], variational Monte Carlo [191–194], and tensor network methods [195]. Most of these studies, with an exception of [189] and [190], were focused on the stripe order, appropriate for the La-based cuprate family. The authors of [190] considered charge order with and without any accompanying magnetic order and showed that the  $t - J$  model, within Gutzwiller mean-field approximation, supports several unidirectional and bidirectional charge ordered states with nearly degenerate energies. Of these, the anti-phase charge density wave (APCDW), a unidirectional commensurate order with periodicity of 4 lattice constants, and nodal pair density wave (nPDW), an incommensurate order with wavevector  $[Q, 0]$  or  $[0, Q]$  with  $Q \approx 0.3$  in units of  $\frac{2\pi}{a_0}$ , exhibit a dominant  $d$ -form factor and exist in a doping range very similar to that in which charge order has been experimentally observed in cuprates. Moreover, the nPDW state, which intertwines uniform  $d$ -wave superconductivity, pair-density wave (PDW), and CDW order, shows a nodal structure in the LDOS spectrum at low energies, similar to the experimental observations [35, 66].

The STM experiments determine the intra-unit cell form factors by directly imaging the Cu and O sites, and the results thus obtained exhibit a significant bias dependence

as shown in the Figure 5-2(e). However, in most of the previous theoretical studies [15, 180, 186, 190, 196], the form factors have been determined from the renormalizations of the nearest-neighbor (NN) hoppings between the Cu lattice sites along the  $x$ - and  $y$ - directions. Such an approach disregards the O degrees of freedom and yields bias-independent form factors. These deficiencies can be alleviated using the calculations based on the three band model of cuprates [197]; however, treating the no-double occupancy criteria in such models is very difficult [198, 199]. Alternatively, we can use the Wannier function based approach described in the Section 2.3 to calculate the STM observables, avoiding the complications of a three band model but still including the O degrees of freedom.

In this chapter, we address the STM findings of Hamidian et al. [66] by calculating the bias dependence of form factors and spatial phase difference in the APCDW and nPDW states using the Wannier function based approach. We first solve the  $t - t' - J$  model within the renormalized mean-field theory (Gutzwiller approximation) and obtain the APCDW and nPDW states. Exploiting the unidirectional nature of the charge ordered states, we have employed a partial Fourier transform based approach to study large systems in a computationally efficient way. Next, we obtain continuum LDOS above Cu and O sites at a typical STM tip height using the Wannier function based approach described in the Section 2.3, and calculate the bias-dependent form factors and the spatial phase difference. We find that the results for the nPDW state compare very well with the experiment [66]. Finally, we show that the PDW character of the charge ordered states plays the key role in yielding the bias dependence of various quantities similar to the experimental observations.

## 5.2 Extended $t - J$ Model

### 5.2.1 Renormalized Mean-Field Theory

The extended  $t - J$  (or  $t - t' - J$ ) model, including next-nearest neighbor (NNN) hopping  $t' = -0.3t$  to appropriately model the Fermi surface of cuprates, is given on a 2D

lattice by

$$H_{tJ} = - \sum_{\langle i,j \rangle, \sigma} P_G \left( t_{ij} c_{i\sigma}^\dagger c_{j\sigma} + \text{H.c.} \right) P_G + J \sum_{\langle i,j \rangle} \mathbf{S}_i \cdot \mathbf{S}_j. \quad (5-2)$$

Here, H.c. refers to Hermitian conjugate,  $c_{i\sigma}^\dagger$  creates an electron at lattice site  $i$  with spin  $\sigma = \pm$ , and  $\mathbf{S}_i$  denotes the spin operator.  $\langle i, j \rangle$  represent NN sites, whereas  $(i, j)$  refers to both NN and NNN sites.  $P_G = \prod_i (1 - n_{i\uparrow} n_{i\downarrow})$ , with  $n_{i\sigma} = c_{i\sigma}^\dagger c_{i\sigma}$  the spin dependent number operator at site  $i$ , represents the Gutzwiller projection operator [200] which ensures that all states with double occupancy of any site are projected out from the Hilbert space. Thus, the first term in the  $t - t' - J$  Hamiltonian represents hopping of electrons in such a way that no doubly occupied site is created. The second term represents the antiferromagnetic exchange interaction between spins at the NN sites with  $J = 0.3t$ .

The projection operator can be treated exactly using the variational Monte-Carlo technique [30] and approximately using slave-boson methods [32, 33] or renormalized mean-field theory [30] within Gutzwiller approximation [201], where the projection operator is replaced by Gutzwiller factors determined from classical counting arguments [30, 201–203]. Application of the Gutzwiller approximation to the Hamiltonian in Equation 5–2 leads to the following renormalized Hamiltonian

$$H = - \sum_{\langle i,j \rangle, \sigma} g_{ij}^t t_{ij} (c_{i\sigma}^\dagger c_{j\sigma} + \text{H.c.}) + \sum_{\langle i,j \rangle} J \left[ g_{ij}^{s,z} S_i^z S_j^z + g_{ij}^{s,xy} \left( \frac{S_i^+ S_j^- + S_i^- S_j^+}{2} \right) \right]. \quad (5-3)$$

Here,  $S_i^z$  represents the  $z$ -component of the spin operator, and  $S_i^+$  ( $S_i^-$ ) represents the raising (lowering) spin operator. The Gutzwiller factors for hopping renormalization ( $g_{ij}^t$ ), longitudinal ( $g^{s,z}$ ), and transverse ( $g^{s,xy}$ ) super-exchange renormalization depend on the local values of hole density  $\delta_i$ , magnetization  $m_i$ , pair field  $\Delta_{ij\sigma}^v$ , and bond field  $\chi_{ij\sigma}^v$

defined by

$$\begin{aligned}
\delta_i &= 1 - \langle \Psi_0 | \sum_{\sigma} n_{i\sigma} | \Psi_0 \rangle \\
m_i &= \langle \Psi_0 | S_i^z | \Psi_0 \rangle \\
\Delta_{ij\sigma}^v &= \sigma \langle \Psi_0 | c_{i\sigma} c_{j\bar{\sigma}} | \Psi_0 \rangle \\
\chi_{ij\sigma}^v &= \langle \Psi_0 | c_{i\sigma}^\dagger c_{j\sigma} | \Psi_0 \rangle
\end{aligned} \tag{5-4}$$

where,  $\bar{\sigma} = -\sigma$  and  $|\Psi_0\rangle$  denotes the unprojected wavefunction. The superscript  $v$  in  $\Delta_{ij\sigma}^v$  and  $\chi_{ij\sigma}^v$  is used to emphasize that these quantities are not the physical order parameters.

The Gutzwiller factors are given as [189]

$$\begin{aligned}
g_{ij\sigma}^t &= g_{i\sigma}^t g_{j\sigma}^t, \quad g_{ij}^{s,xy} = g_i^{s,xy} g_j^{s,xy} \\
g_{i\sigma}^t &= \sqrt{\frac{2\delta_i(1-\delta_i)}{1-\delta_i^2+4m_i^2} \frac{1+\delta_i+2m_i\sigma}{1+\delta_i-2m_i\sigma}} \\
g_i^{s,xy} &= \frac{2(1-\delta_i)}{1-\delta_i^2+4m_i^2} \\
g_{ij}^{s,z} &= g_{ij}^{s,xy} \left[ \frac{2(\bar{\Delta}_{ij}^2 + \bar{\chi}_{ij}^2) - 4m_i m_j X_{ij}^2}{2(\bar{\Delta}_{ij}^2 + \bar{\chi}_{ij}^2) - 4m_i m_j} \right] \\
X_{ij} &= 1 + \frac{12(1-\delta_i)(1-\delta_j)(\bar{\Delta}_{ij}^2 + \bar{\chi}_{ij}^2)}{\sqrt{(1-\delta_i^2+4m_i^2)(1-\delta_j^2+4m_j^2)}},
\end{aligned} \tag{5-5}$$

where,  $\bar{\Delta}_{ij} = \frac{1}{2} \sum_{\sigma} \Delta_{ij\sigma}^v$  and  $\bar{\chi}_{ij} = \frac{1}{2} \sum_{\sigma} \chi_{ij\sigma}^v$ . Since we are interested in the charge ordered state, which does not accompany any magnetic order, we can simplify the Gutzwiller factors by putting  $m_i = 0$  as

$$\begin{aligned}
g_i^t &= \sqrt{\frac{2\delta_i}{1+\delta_i}} \\
g_i^{s,xy} &= \frac{2}{1+\delta_i} \\
g_{ij}^{s,z} &= g_{ij}^{s,xy} = g_{ij}^s.
\end{aligned} \tag{5-6}$$

By the mean-field decomposition of the quartic operators in the renormalized Hamiltonian (Equation 5-3) we can obtain a quadratic Hamiltonian  $H_{H-F}$ . However, due to the dependence of the renormalization factors on the mean-fields themselves, a direct mean-field decomposition does not yield the lowest ground state energy

$E_g = \langle \Psi_0 | H_{H-F} | \Psi_0 \rangle$ . Instead,  $E_g$  should be minimized with respect to  $|\Psi_0\rangle$  under the constraint of fixed electron filling  $N_e$  and normalization of the wavefunction. Equivalently, we can minimize following function

$$W = \langle \Psi_0 | H | \Psi_0 \rangle - \lambda (\langle \Psi_0 | \Psi_0 \rangle - 1) - \mu (\sum_i n_i - N_e), \quad (5-7)$$

where  $\lambda$  and  $\mu$  are the Lagrange multipliers. Enforcing  $\frac{\delta W}{\delta \langle \Psi_0 |} = 0$  leads to the following mean-field Hamiltonian [189, 190, 204]

$$H_{MF} = \sum_{(i,j),\sigma} \epsilon_{ij\sigma} c_{i\sigma}^\dagger c_{j\sigma} + h.c. + \sum_{(i,j),\sigma} \sigma D_{ij\sigma}^* c_{i\sigma} c_{j\bar{\sigma}} + h.c. - \sum_{i,\sigma} \mu_{i\sigma} n_{i\sigma}, \quad (5-8)$$

where

$$\begin{aligned} \epsilon_{ij\sigma} &= -g_{ij}^t t_{ij} - \delta_{ij,\langle ij \rangle} \frac{3}{4} J g_{ij}^s \chi_{ij\sigma}^{v*} \\ D_{ij\sigma}^* &= -\frac{3}{4} J g_{ij}^s \Delta_{ij\sigma}^{v*} \\ \mu_{i\sigma} &= \mu + \frac{3J}{4} \sum_{j\sigma'} \left( |\Delta_{ij\sigma'}^v|^2 + |\chi_{ij\sigma'}^v|^2 \right) \frac{dg_{ij}^s}{dn_{i\sigma}} + t_{ij} \sum_{j\sigma'} (\chi_{ij\sigma'}^v + \chi_{ij\sigma'}^{v*}) \frac{dg_{ij}^t}{dn_{i\sigma}} \\ \frac{dg_{ij}^s}{dn_{i\sigma}} &= -\frac{g_j^t}{(1 + \delta_i)^2}; \quad \frac{dg_{ij}^t}{dn_{i\sigma}} = \frac{2g_j^t}{\sqrt{2\delta_i}(1 + \delta_i)^{3/2}}. \end{aligned} \quad (5-9)$$

Here,  $\delta_{ij,\langle ij \rangle} = 1$  if  $i$  and  $j$  are NNs and 0 otherwise. Note that Equation 5–9 is true only for the non-magnetic state ( $m_i = 0$ ). For a magnetic state, the expressions for the parameters in Equation 5–8 are much more complicated and can be found in [190, 204]. The physical  $d$ -wave superconducting gap order parameter and the bond order along  $x(y)$  direction are given by

$$\Delta_i = \frac{1}{8} \sum_{\sigma} (g_{i,i+\hat{x}}^t \Delta_{i,i+\hat{x},\sigma}^v + g_{i,i-\hat{x}}^t \Delta_{i,i-\hat{x},\sigma}^v - g_{i,i+\hat{y}}^t \Delta_{i,i+\hat{y},\sigma}^v - g_{i,i-\hat{y}}^t \Delta_{i,i-\hat{y},\sigma}^v) \quad (5-10)$$

$$\chi_{i,i+\hat{x}(\hat{y})} = \frac{1}{2} \sum_{\sigma} (g_{i,i+\hat{x}(\hat{y})}^t \chi_{i,i+\hat{x}(\hat{y}),\sigma}^v + \text{H.c.}) \quad (5-11)$$

### 5.2.2 Quasi 1D BdG Equations

The charge order observed in various cuprates is unidirectional with modulations along either of the Cu-O bond directions [36]. Accordingly, we study only states of this

type, by assuming charge modulations along  $x$ -direction, and utilize the translational invariance along the  $y$ -direction to convert the 2D Hamiltonian in Equation 5–8 into a quasi-1D Hamiltonian, substantially reducing the computational cost of diagonalization. We change the basis  $(i_x, i_y)$  to  $(i_x, k)$  using the following transformation

$$c_{i\sigma}^\dagger = \frac{1}{\sqrt{N}} \sum_k c_{i_x\sigma}^\dagger(k) e^{-ikR_{i_y}}. \quad (5-12)$$

Here,  $c_{i_x\sigma}^\dagger(k)$  creates an electron at quasi-1D site  $i_x$  with transverse momentum  $k$  and spin  $\sigma$ ,  $N$  is the number of lattice sites in  $y$ -direction, and  $R_{i_y}$  is the  $y$ -component of the lattice vector corresponding to site  $i$ . Using this transformation, the mean-field Hamiltonian in Equation 5–8 becomes

$$\begin{aligned} H_{MF} = & \sum_{\langle i_x, j_x \rangle, k, \sigma} \epsilon_{i_x j_x \sigma}(k) c_{i_x \sigma}^\dagger(k) c_{j_x \sigma}(k) + \text{H.c.} \\ & + \sum_{\langle i_x, j_x \rangle, k, \sigma} \sigma D_{i_x j_x \sigma}^*(k) c_{i_x \sigma}(k) c_{j_x \bar{\sigma}}(-k) + \text{h.c.} - \sum_{i_x, k, \sigma} \mu_{i_x \sigma} n_{i_x \sigma}(k), \end{aligned} \quad (5-13)$$

where

$$\epsilon_{i_x j_x \sigma}(k) = \sum_{i_y} \epsilon_{i_x i_y j_x 0 \sigma} e^{-ikR_{i_y}}, \quad D_{i_x j_x \sigma}(k) = \sum_{i_y} D_{i_x i_y j_x 0 \sigma} e^{-ikR_{i_y}}, \quad \mu_{i_x \sigma} = \mu_{(i_x, 0) \sigma}. \quad (5-14)$$

$H_{MF}$  is quadratic in electron operators and can be diagonalized using the following spin-generalized Bogoliubov transformation,

$$\begin{aligned} c_{i_x \sigma}(k) &= \sum_n \left[ u_{i_x \sigma}^n(k) \gamma_{n\sigma}(k) + v_{i_x \sigma}^{n*}(k) \gamma_{n\bar{\sigma}}^\dagger(k) \right] \\ c_{i_x \bar{\sigma}}^\dagger(-k) &= \sum_n \left[ v_{i_x \bar{\sigma}}^n(k) \gamma_{n\sigma}(k) + u_{i_x \bar{\sigma}}^{n*}(k) \gamma_{n\bar{\sigma}}^\dagger(k) \right] \end{aligned} \quad (5-15)$$

Proceeding in a manner very similar to the derivation of BdG equations in Section 2.2.2, we obtain the following BdG equations for the mean-field Hamiltonian in Equation 5–13

$$\sum_{j_x} \begin{bmatrix} \xi_{i_x j_x \uparrow}(k) & -D_{i_x j_x \uparrow}(-k) \\ -D_{j_x i_x \uparrow}^*(k) & -\xi_{i_x j_x \downarrow}^*(-k) \end{bmatrix} \begin{bmatrix} u_{j_x \uparrow}^n(k) \\ v_{j_x \downarrow}^n(k) \end{bmatrix} = E_{n\uparrow}(k) \begin{bmatrix} u_{i_x \uparrow}^n(k) \\ v_{i_x \downarrow}^n(k) \end{bmatrix}. \quad (5-16)$$

Here,  $\xi_{i_x j_x \sigma}(k) = \epsilon_{i_x j_x \sigma}(k) - \mu_{i_x \sigma} \delta_{i_x j_x}$ . The electron density, pair field, and bond fields are given by the following equations:

$$\begin{aligned}
n_{i_x \uparrow} &= \frac{1}{N} \sum_k n_{i_x \uparrow}(k) = \frac{1}{N} \sum_{nk} |u_{i_x \uparrow}^n(k)|^2 f(E_{n \uparrow}(k)) \\
n_{i_x \downarrow} &= \frac{1}{N} \sum_k n_{i_x \downarrow}(k) = \frac{1}{N} \sum_{nk} |v_{i_x \downarrow}^n(k)|^2 [1 - f(E_{n \uparrow}(-k))] \\
\Delta_{i_x j_x \uparrow}^v(k) &= \sum_n u_{i_x \uparrow}^n(k) v_{j_x \downarrow}^{n*}(k) [1 - f(E_{n \uparrow}(k))] \\
\chi_{i_x j_x \uparrow}^v(k) &= \sum_n u_{i_x \uparrow}^{n*}(k) u_{j_x \uparrow}^n(k) f(E_{n \uparrow}(k)) \\
\chi_{i_x j_x \downarrow}^v(k) &= \sum_n v_{i_x \downarrow}^n(-k) v_{j_x \downarrow}^{n*}(-k) [1 - f(E_{n \uparrow}(-k))],
\end{aligned} \tag{5-17}$$

where  $f$  denotes the Fermi function and the sum runs over all values of  $n$ .

Equations 5-16 and 5-17 are solved self-consistently using the following procedure, very similar to that outlined in Section 2.4.

1. Choose initial guesses for the chemical potential  $\mu_0$ , hole density  $\delta_i$ , pair field  $\Delta_{ij}^v$  on NN sites, bond field  $\chi_{ij}$  on NN and NNN sites. We take pair field as a sinusoidal function with amplitude  $\Delta_0$  and wavenumber  $Q_0$ , keeping the hole density and bond fields uniform:

$$\begin{aligned}
\delta_i &= \delta_0 \\
\Delta_{i, i+\hat{x}, \uparrow}^v(k) &= \Delta_0 \cos[2\pi Q_0(i_x + 1/2)] \\
\Delta_{i, i+\hat{y}, \uparrow}^v(k) &= -\Delta_0 \cos(2\pi Q_0 i_x) \\
\chi_{i, i+\hat{x}(\hat{y}) \uparrow}^v &= \chi_{i, i+\hat{x}(\hat{y}) \downarrow}^v = \chi_0^{NN} \\
\chi_{i, i+\hat{x} \pm \hat{y} \uparrow}^v &= \chi_{i, \hat{x} \pm \hat{y} \downarrow}^v = \chi_0^{NNN}
\end{aligned} \tag{5-18}$$

The modulating pair field induces modulations in charge density [205], as they are coupled to each other through the BdG equations (Equations 5-13 and 5-17).

2. Compute the Gutzwiller factors, their relevant derivatives, and local chemical potential  $\mu_i$  using Equations 5-6 and 5-9.
3. For each  $k = \frac{m}{N}$  (in units of  $\frac{2\pi}{a_0}$ );  $m = 0, 1, 2, \dots, N - 1$  (a) construct the BdG matrix in Equation 5-16 using the definitions of matrix elements from Equation 5-14 (b) Find the eigenvalues  $E_n(k)$  and eigenvectors  $[u_{i_x \uparrow}^n(k), v_{i_x \downarrow}^n(k)]$ . (c) Find the  $k$ -space mean-fields  $n_{i_x \sigma}(k)$ ,  $\Delta_{i_x j_x \uparrow}^v(k)$ , and  $\chi_{i_x j_x \sigma}^v(k)$  using Equation 5-17.

4. Find the lattice mean-fields using following equations:

$$\begin{aligned}
n_{i\sigma} &= \frac{1}{N} \sum_k n_{i_x\sigma}(k) \\
\Delta_{i,i+\hat{x},\uparrow}^v(k) &= \frac{1}{N} \sum_k \Delta_{i_x,i_x+1,\uparrow}^v(k) \\
\Delta_{i,i+\hat{y},\uparrow}^v(k) &= \frac{1}{N} \sum_k \Delta_{i_x,i_x,\uparrow}^v(k) e^{ik} \\
\chi_{i,i+\hat{x},\sigma}^v &= \frac{1}{N} \sum_k \chi_{i_x,i_x+1,\sigma}^v(k) \\
\chi_{i,i+\hat{y},\sigma}^v &= \frac{1}{N} \sum_k \chi_{i_x,i_x,\sigma}^v(k) e^{ik} \\
\chi_{i,i+\hat{x}+\hat{y},\sigma}^v &= \frac{1}{N} \sum_k \chi_{i_x,i_x+1,\sigma}^v(k) e^{ik}.
\end{aligned} \tag{5-19}$$

5. Check convergence. If mean fields obtained in step 4 do not change from their values in previous iterations up to a desired accuracy then convergence is achieved and there is no need for further iterations; otherwise go to step 6.
6. Update the mean-fields and chemical potential by mixing the mean fields from current and previous iterations.
7. Go to step 2.

### 5.2.3 Calculation of STM Observables

In most previous theoretical work [15, 180, 186, 196], the intra-unit cell form factors ( $s$ ,  $s'$ , and  $d$ ) of the charge order have been determined from the Fourier transform of the charge density on Cu lattice sites and the NN bond order parameter  $\chi_{i,i+\hat{x}(\hat{y})}$  which can be thought as a measure of charge density on the Cu-O bonds. Mathematically,

$$\begin{aligned}
D^x(\mathbf{q}) &= FT(\tilde{\chi}_{i,i+\hat{x}} - \tilde{\chi}_{i,i+\hat{y}})/2 \\
S'^x(\mathbf{q}) &= FT(\tilde{\chi}_{i,i+\hat{x}} + \tilde{\chi}_{i,i+\hat{y}})/2 \\
S^x(\mathbf{q}) &= FT(1 - \tilde{\delta}_i).
\end{aligned} \tag{5-20}$$

Here,  $FT$  represents the Fourier transform and  $\tilde{\phantom{x}}$  refers to the subtraction of the spatial average of the corresponding quantity. Clearly, there is no bias dependence of the form factors defined in this way. However, the STM experiments [66] used phase-resolved LDOS

[65] obtained at Cu and O sublattices to define the form factors and calculated their bias dependence. Using the Wannier function based method described in the Section 2.3, we can adopt a similar approach.

The first step is to construct the the Green's function matrix in lattice space, using the self-consistent solution of the BdG equations (Equations 5–13 and 5–17), through following equations.

$$\begin{aligned}
G_{ij\sigma}(\omega) &= \frac{1}{N} \sum_k g_{ij}^t G_{i_x j_x \sigma}(k, \omega) e^{ik(R_{i_y} - R_{j_y})} \\
G_{i_x j_x \sigma}(k, \omega) &= \sum_{n>0} \left[ \frac{u_{i_x \sigma}^n(k) u_{j_x \sigma}^{n*}(k)}{\omega - E_{n\sigma} + i0^+} + \frac{v_{i_x \sigma}^{n*}(k) v_{j_x \sigma}^n(k)}{\omega + E_{n\bar{\sigma}}(k) + i0^+} \right].
\end{aligned} \tag{5-21}$$

Here,  $0^+$  is the artificial broadening and  $n > 0$  indicates that the sum is to be performed over eigenstates with positive eigenvalues only. With lattice Green's functions in hand, the continuum LDOS  $\rho_\sigma(\mathbf{r}, \omega)$  at a continuum position  $\mathbf{r}$  and a given bias  $\omega$  can be obtained using Equations 2–14 and 2–18. Following the experimental procedure [66], we obtain the continuum LDOS map at a typical STM tip height  $z \approx 5 \text{ \AA}$  above the BiO plane at positive and negative biases, and construct the  $Z$ -maps defined below [35],

$$\rho^Z(\mathbf{r}, \omega > 0) = \frac{\sum_\sigma \rho_\sigma(\mathbf{r}, \omega)}{\sum_\sigma \rho_\sigma(\mathbf{r}, -\omega)}. \tag{5-22}$$

Subsequently, we segregate the  $Z$ -maps in three sublattices:  $Cu^Z(\mathbf{r}, \omega)$ ,  $O_x^Z(\mathbf{r}, \omega)$  and  $O_y^Z(\mathbf{r}, \omega)$  corresponding to a Cu and two inequivalent O atoms along mutually orthogonal CuO bond directions  $x$  and  $y$  in the unit cell. The form factors can be obtained by taking proper linear combinations of the Fourier transforms of the sublattice  $Z$ -maps as follows [66]

$$\begin{aligned}
D^Z(\mathbf{q}, \omega) &= (\tilde{O}_x^Z(\mathbf{q}, \omega) - \tilde{O}_y^Z(\mathbf{q}, \omega))/2 \\
S'^Z(\mathbf{q}, \omega) &= (\tilde{O}_x^Z(\mathbf{q}, \omega) + \tilde{O}_y^Z(\mathbf{q}, \omega))/2 \\
S^Z(\mathbf{q}, \omega) &= \tilde{C}u^Z(\mathbf{q}, \omega).
\end{aligned} \tag{5-23}$$

In addition to the bias dependence of the intra-unit cell form factors, Hamidian et al. [66] also obtained the the bias dependence of the average spatial phase difference

( $\Delta\phi$ ) between the  $d$ -form factor modulations above and below the Fermi energy and found that it switches from 0 to  $\pi$  close to the energy scale where the  $d$ -form factor becomes dominant. To address this intriguing observation, we compute  $\Delta\phi$  following the experimental procedure [66]. We first obtain the  $d$ -form factor  $D^g(\mathbf{q}, \omega)$  using the sublattice continuum LDOS maps (or  $g$ -maps). Subsequently, the  $d$ -form factor modulation vector  $\mathbf{Q}_d$  is filtered out using a Gaussian filter, followed by the inverse Fourier transform to yield a spatial map  $D(\mathbf{r}, \omega)$ . Finally, its phase  $\phi(\mathbf{r}, \omega)$  is calculated at  $\pm\omega$  and their difference is averaged over space to obtain  $\Delta\phi$ . Mathematically,

$$\begin{aligned}
D^g(\mathbf{q}, \omega) &= (\tilde{O}_x^g(\mathbf{q}, \omega) - \tilde{O}_y^g(\mathbf{q}, \omega))/2 \\
D(\mathbf{r}, \omega) &= \frac{2}{(2\pi)^2} \int d\mathbf{q} e^{i\mathbf{q}\mathbf{r}} D^g(\mathbf{q}, \omega) e^{-\frac{(\mathbf{q}-\mathbf{Q}_d)^2}{2\Lambda^2}} \\
\phi(\mathbf{r}, \omega) &= \arctan(\text{Im}[D(\mathbf{r}, \omega)]/\text{Re}[D(\mathbf{r}, \omega)]) \\
\Delta\phi &= \langle \phi(\mathbf{r}, \omega) - \phi(\mathbf{r}, -\omega) \rangle.
\end{aligned} \tag{5-24}$$

### 5.3 Unidirectional Charge Ordered States in Extended $t - J$ Model

Although the  $t - J$  model supports a variety of charge ordered states [189, 190], here we will focus on the APCDW and nPCDW states which are shown to have dominant  $d$ -form factor [190]. To obtain the APCDW state with periodicity of four lattice constants, we work with a system size which is a multiple of 8 and initialize the BdG equations (Equations 5-13 and 5-17) with a sinusoidal  $d$ -wave pair field modulating with wavenumber  $Q_0 = 1/8$  (in units of  $\frac{2\pi}{a_0}$ ). Although, it is impossible to obtain a true incommensurate charge ordered state in a finite lattice calculation, we can still obtain a quasi-incommensurate state with a periodicity equal to the system's length. Such a state can be thought as a mixture of several commensurate states with different lattice periodicities and can be obtained by initializing BdG equations with a modulating pair-field with  $Q_0 \neq \frac{m}{N}$ , where  $m$  is an integer. We emphasize that the initializing BdG equations with a pair density wave drives the charge ordering. This can be easily seen through Equation 5-9 which shows that the local chemical potential  $\mu_{i\sigma}$  depends on the

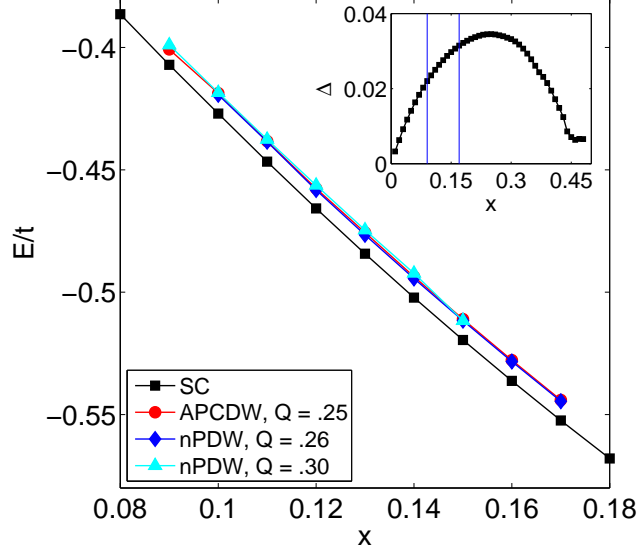


Figure 5-3. Energy per site ( $E/t$ ) at various hole dopings ( $x$ ) for homogeneous superconducting state, APCDW, and nPDW states. Inset: Variation of superconducting order parameter in the homogeneous state as a function of hole doping. Vertical lines mark the doping range in which APCDW and nPDW states are realized.

square of pair fields  $|\Delta_{ij\sigma}^v|^2$ . Thus,  $\Delta$  with a modulating component  $Q_0$  in the off-diagonal terms of the BdG matrix in Equation 5-13 induces a modulating component  $2Q_0$  in the diagonal terms, resulting into a  $2Q_0$  modulating component in the electron density when the self-consistent solution converges. Similar conclusions were drawn in [205], however, using the Green's functions method.

The doping dependence of the energy per site ( $E/t$ ) for the uniform superconducting state, APCDW state with charge modulation wavevector  $[Q, 0]$ ;  $Q = 0.25$ , and nPDW state with  $Q = 0.26$  and  $0.3$  is shown in Figure 5-3. The inset depicts a plot of  $d$ -wave order parameter in the uniform superconducting state as function of hole doping ( $x$ ) showing a dome like shape in range  $x = 0.01 - 0.48$ . The charge ordered states occur in a narrow doping range of  $0.09 - 0.17$ . We find that the APCDW and nPDW states, with different wavevectors, have almost identical energy per site at all dopings. At this point, it is not clear whether this near degeneracy of charge ordered states is an intrinsic feature of the  $t - t' - J$  model or just an artifact of the Gutzwiller approximation. Although

we just show two nPDW states with different wavevectors, we find that there are many possible nPDW states with  $Q$  in the range of 0.2-0.35. We note that the STM and x-ray scattering experiments find the charge order in cuprates existing in the a doping and wavevector range very similar to our finding [36, 66]. However, we can not address the doping dependence of the ordering wavevector [36] within our model, as the nPDW states with different  $Q$  are almost degenerate.

It is clear from Figure 5-3 that the uniform state has lowest energy at all dopings. A similar conclusion was drawn in the previous studies of the  $t - J$  like models using different numerical schemes [189–192, 195]. However, the energy difference between the charge ordered and uniform state is very small,  $O(1 \text{ meV})$  per site, and can be overcome by other effects such as electron-phonon coupling and disorder, thus, stabilizing charge ordered states as the ground state. The STM [59] and resonant x-ray scattering [36] observation of short coherence length ( $\approx 30 \text{ \AA}$  [36]) indeed points towards the important role of disorder. We leave the systematic study of charge ordering in the disordered  $t - J$  model for a future project. The application of a magnetic field of order 10 T (or 1 meV) might be another possible route to tip the energy balance in favor of charge ordered states. In fact, the charge ordered states with large coherence length ( $> 100$  lattice constants) have been recently observed in YBCO in the presence of a magnetic field of  $O(30 \text{ T})$  [206]. We plan to study the effects of the magnetic field on the charge ordered states realized in the extended  $t - J$  model in a future project.

In what follows, we describe the characteristics of the APCDW and nPDW states and show that the latter exhibit bias dependence of the LDOS, form factors, and spatial phase difference, very similar to that observed in the STM experiments [35, 66]. Although many properties of the APCDW state such as its commensurate nature, bias dependence of the continuum LDOS and the spatial phase difference do not conform to the experimental observations [36, 66], we still discuss it in detail to set the stage for a more complicated nPDW state.

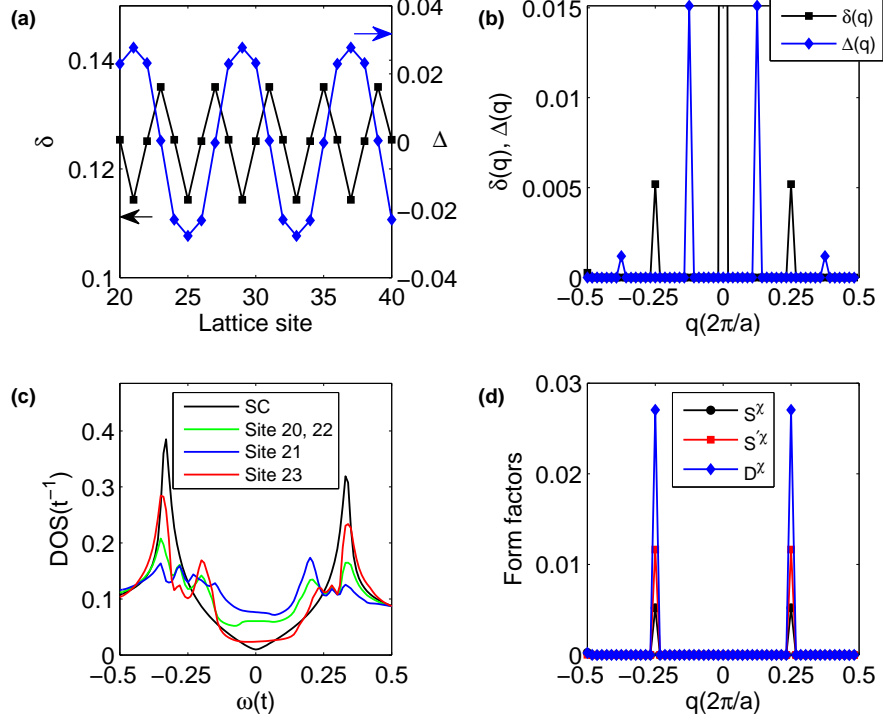


Figure 5-4. Characteristic features of the APCDW state. (a) Variation of the hole density ( $\delta$ ) and gap order parameter ( $\Delta$ ) with lattice sites in the central region of a  $56 \times 56$  system. y-axis in left (right) corresponds to  $\delta$  ( $\Delta$ ). (b) Fourier transform of the hole density ( $\delta(q)$ ) and gap order parameter ( $\Delta(q)$ ). The  $q = 0$  component of the hole density modulation, not shown in the plot, is 0.125. (c) Density of states in the homogeneous superconducting state and, APCDW state over a period of lattice sites. (d) Intra-unit cell form factors in APCDW state computed using Equation 5-20.

### 5.3.1 Anti-Phase Charge Density Wave State

Figure 5-4 shows the characteristics of the APCDW state obtained for a  $56 \times 56$  lattice system at the doping level  $x = 0.125$ . The hole density ( $\delta$ ) and superconducting gap order parameter ( $\Delta$ ) modulate along the  $x$ -axis with a periodicity of 4 and 8 lattice constants, respectively, as shown in Figure 5-4(a).  $\Delta$  changes sign after a period of charge modulation, hence the name 'anti-phase' pair density wave. The maximum of hole density occurs at the domain wall sites where  $\Delta$  vanishes. The real space findings are echoed in the Fourier domain where we find that the dominant charge and gap modulation wavevectors are  $Q = 0.25$  and  $Q_{\Delta} = 0.125$ , respectively, as shown in Figure 5-4(b). The

relation  $Q = 2Q_\Delta$  is also found in the Ginzburg-Landau theories of the CDW driven by a PDW [163].

Figure 5-4(c) shows the LDOS at a set of four inequivalent lattice sites in the APCDW state. LDOS in the uniform  $d$ -wave superconducting state is also shown for the comparison. In the APCDW state, LDOS is non-vanishing at all sites and all energies and has a U-shape with two sets of coherence peaks, with peaks at the higher energies almost coinciding with the uniform  $d$ -wave coherence peaks. The coherence peaks in the APCDW state arise from the Andreev bound states (ABS) [189]. ABS occur at the domain wall sites where the superconducting changes sign and form one-dimensional band due to translational invariance in  $y$ -direction. Moreover, the hybridization between the Andreev states at the neighboring domain walls leads to the broadening of ABS peaks, and a shift in the ABS energy away from the chemical potential [189, 207].

Figure 5-4(d) shows the wavevector dependence of the intra-unit cell form factors in the APCDW state, calculated from the bond order parameter  $\chi_{ij\sigma}$  using Equation 5-20. Clearly, all form factors peak at  $q = Q$  with  $d$ -form factor having the largest weight. However, as discussed in Section 5.2.3, to find the bias dependence of the form factors in a manner similar to the STM experiments [66] we must find the continuum LDOS at Cu and O sites and calculate the form factors using Equation 5-23.

We take the Wannier function for BSCCO (discussed in detail in Section 4.2) as an input and calculate the continuum LDOS at a height  $z \approx 5 \text{ \AA}$  above the the BiO plane using Equations 5-21, 2-14, and 2-18. Very recently, we found that the shape of NaCCOC Wannier function at the heights few  $\text{\AA}$  above the surface exposed to the STM tip, is very similar to the BSCCO, and hence we expect that both should have similar real space pattern of continuum LDOS. Indeed, the STM experiments find a very similar ladder-like patterns (Figure 5-2(a-b)) in both compounds [35]. Figure 5-5(a) shows the continuum LDOS map at  $\omega = 0.25t$  in a  $20 \times 20$  unit cell area located in the central region of  $56 \times 56$  system. Clearly, the continuum LDOS exhibits a periodic modulation in the  $x$ -direction

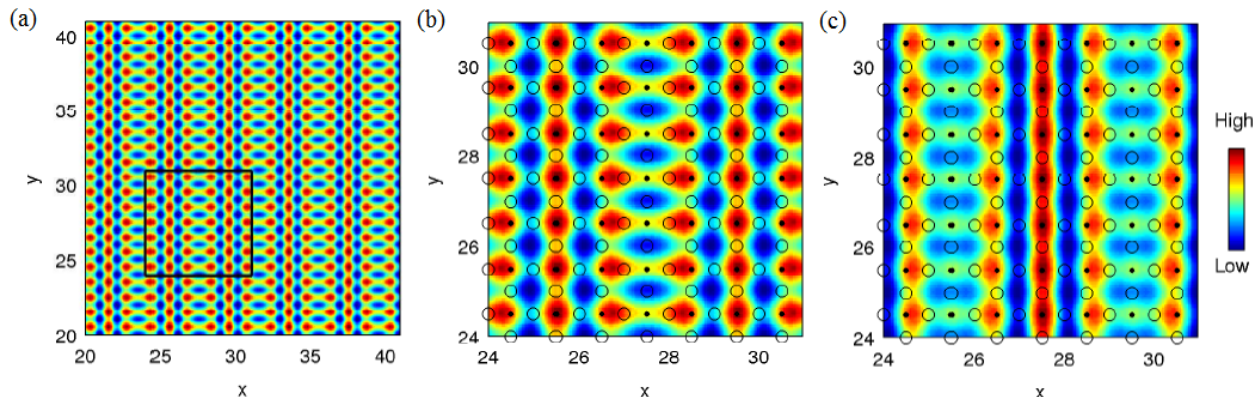


Figure 5-5. Continuum LDOS map at  $\omega = \pm 0.25t$  and at a height  $z \approx 5 \text{ \AA}$  above the BiO plane in the APCDW state. (a) LDOS map at  $\omega = 0.25t$  in a range of  $20 \times 20$  unit cells. (b) Zoomed-in view of the area marked by square in (a). Black dots and open circles represent position of Cu and O atoms, respectively, in the CuO plane underneath. (c) LDOS map at  $\omega = -0.25t$  in the same region as in (b).

with a wavelength of four lattice constants. A zoomed-in view of the region bounded by the black square is shown in Figure 5-5(b). Black dots and circles mark the locations of Cu and O sites, respectively, underneath. We find that the LDOS shows modulation on both Cu and O sites, suggesting that all form factors ( $s, s'$ , and  $d$ ) have non-zero weight at this particular bias. Moreover, when the LDOS on a  $O_x$  site in a unit cell is large then the LDOS on  $O_y$  site in the same cell is small, implying that the modulations on  $O_x$  and  $O_y$  sites are out of phase. Thus, at this particular bias the  $d$ -form factor must have larger weight than the  $s'$ -form factor. Figure 5-5(c) shows the continuum LDOS map at the negative bias  $\omega = -0.25t$  in the same region as in Figure 5-5(b). Comparing both figures, we find that the sites with larger LDOS at the positive bias have smaller LDOS at the negative bias, suggesting a spatial phase difference of  $\pi$  between the two biases.

Now, we will examine the bias dependence of the continuum LDOS, form factors, and spatial phase differences in the APCDW state. Figure 5-6(a) shows the continuum LDOS spectrum at the Cu and two inequivalent O sites ( $O_x$  and  $O_y$ ) in the unit cell  $[27, 27]$  at a height  $z \approx 5 \text{ \AA}$  above the BiO plane. The inset shows the position of the Cu and O sites, marked by a black dot and circles, respectively, with reference to the continuum

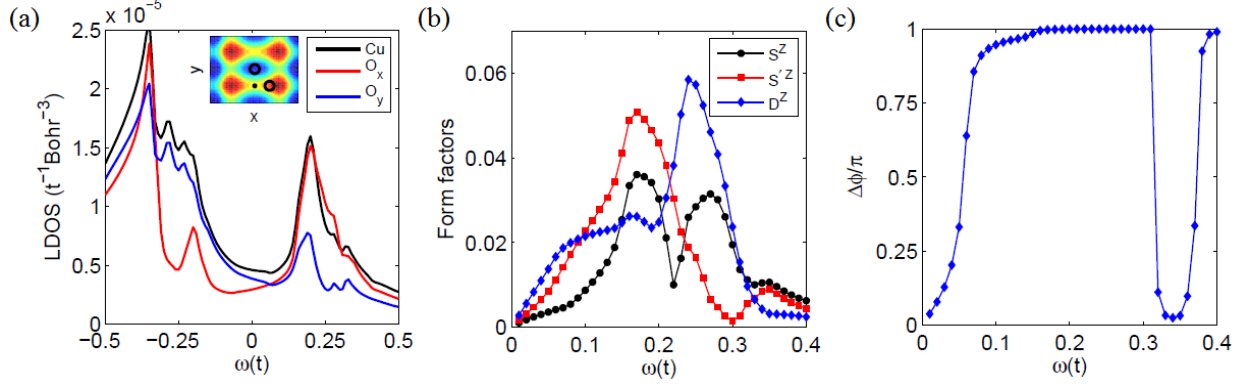


Figure 5-6. (a) Continuum LDOS spectrum registered above Cu, O<sub>x</sub> and O<sub>y</sub> sites in the unit cell [27, 27] at the height  $z \approx 5 \text{ \AA}$  above the BiO plane. The location of the unit cell can be inferred from Figure 5-5(b). Bias dependence of the (b) intra-unit cell form factors and (c) average spatial phase difference at doping  $x = 0.125$ .

LDOS map shown in Figure 5-5(b). The low-energy U-shape feature, similar to the lattice LDOS spectrum, can be easily observed. This is very different from the STM conductance measurements [35, 66] which find a V-shaped nodal structure around  $\omega = 0$  (see Figure 5-9(c)). Figure 5-6(b) shows the bias dependence of the form factors evaluated at the wavevector  $\mathbf{q} = [0.25, 0]$ . The  $s'$ -form factor shows a peak at an energy  $\omega = 0.17t$  whereas the  $d$ -form factor peaks at a higher energy  $\omega = 0.24t$ . Moreover, the  $s$ -form factor has the least weight at all energies below  $0.3t$ . Although, these features resemble the experimental observation [66] (see Figure 5-10(b)), the bias dependence of the spatial phase difference ( $\Delta\phi$ ) shown in the Figure 5-10(c) exhibits a qualitative departure from the experiment [66]. In the APCDW state  $\Delta\phi$  is non-zero at all energies in the window  $[0, 0.4t]$ , and displays a steep increase from a small value at  $\omega = 0$  to close to  $\pi$  at  $\omega = 0.17t$ . The STM experiments, however, find that at low energies  $\Delta\phi$  remains nearly zero up to an  $\omega$  which falls between the  $s'$ - and  $d$ -form factor peaks (compare Figures 5-11(b) and 5-10(b)). In the following section, we show that the nPDW state correctly captures all qualitative features of the bias dependence of the form factors as well as the spatial phase difference.

To obtain an quasi-incommensurate nPDW state, we solve the BdG equations (Equations 5-13 and 5-17) self-consistently on a  $60 \times 60$  lattice. As an initial guess,

we take a pair field modulating with wavenumber  $Q_0 = 0.154$  keeping uniform values for the hole density and bond field. Figure 5-7 shows the characteristics of the nPDW state at the doping level  $x = 0.125$ . The variation of the hole density ( $\delta$ ) and the  $d$ -wave superconducting gap order parameter  $\Delta$  with lattice sites is shown in the Figure 5-7(a). We find that the hole density shows a root mean square deviation of  $\Delta\delta = 0.01$  holes from the average value of 0.125, similar to the NMR results [34] showing a hole density variation of  $\Delta\delta = 0.03 \pm 0.01$  in the charge ordered phase of the 10.8% hole-doped YBCO. Moreover, the hole density is observed to be maximum at the domain wall sites where  $\Delta$  changes sign. As shown in Figure 5-7(b), the Fourier transform of the hole density contains many Fourier components, with largest contribution from  $Q_\delta = 0.3$ , reflecting the quasi-incommensurate nature. The gap order parameter too has many Fourier components with dominant contribution from the  $Q_\Delta = 0.15$ . The relations  $Q_\delta = 2Q_\Delta$  holds as in the case of APCDW. However, in contrast to the APCDW, the nPDW state has a non-vanishing uniform ( $q = 0$ ) component of the  $d$ -wave gap parameter. Thus, the nPDW state intertwines incommensurate CDW, incommensurate PDW, and uniform  $d$ -wave superconductivity. The effect of a finite uniform component can be seen as the appearance of a V-shape nodal structure in the lattice LDOS at low energies as shown in the Figure 5-7(c). As in the case of APCDW, we find the two sets of coherence peaks at the energies  $\approx \pm 0.21t$  and  $\approx \pm 0.37t$  which can be attributed to the Andreev bound states as explained in Section 5.3.1. In Figure 5-7(d), we plot the wavevector dependence of the form factors obtained from the bond order parameter using Equation 5-20. We find that all form factors peak at  $q = Q_\delta = 0.3$  with the  $d$ -form factor having the largest weight.

### 5.3.2 Nodal Pair Density Wave State

To compare with the STM findings of Hamidian et. al. [66], we obtain continuum LDOS in the nPDW state and use it to find the bias dependence of the form factors and spatial phase difference. Figure 5-8(a) shows the continuum LDOS map at  $\omega = 0.25t$  and a height  $z \approx 5 \text{ \AA}$  above the BiO plane in a  $20 \times 20$  unit cell area located in the

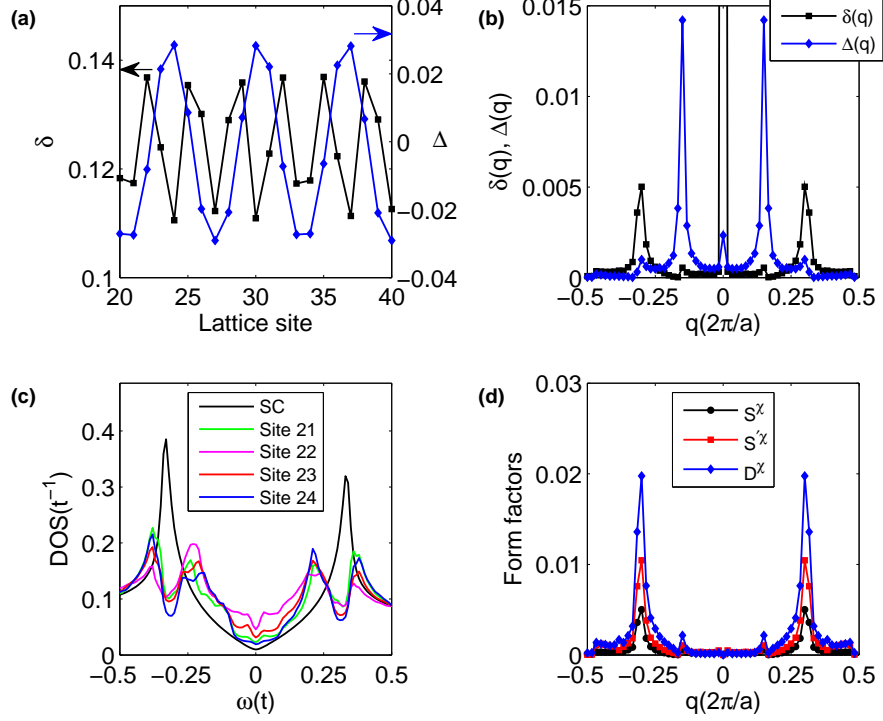


Figure 5-7. Characteristic features of nPDW state. (a) Variation of hole density ( $\delta$ ) and gap order parameter ( $\Delta$ ) with lattice sites in the central region of  $60 \times 60$  system. y-axis on left (right) corresponds to  $\delta$  ( $\Delta$ ). (b) Fourier transform of the hole density ( $\delta(q)$ ) and gap order parameter ( $\Delta(q)$ ). The  $q = 0$  component of hole density modulation, not shown in the plot, is 0.125. (c) Density of states in the homogeneous superconducting state and nPDW state on four consecutive lattice sites. (d) Intra-unit cell form factors in nPDW state computed using Equation 5-20.

central region of the  $60 \times 60$  unit cell system. Two kinds of modulating stripes can be seen here. A zoomed-in view of one of these stripes in the area marked by the black square is shown in Figure 5-8(b). Black dots and open circles mark the Cu and O sites, respectively, underneath. LDOS modulations are observed on both Cu and O sites, suggesting non-zero weights for all form factors. Also, the modulations at the  $O_x$  and  $O_y$  sites are out of phase, indicating that the  $d$ -form factor has a larger contribution at this bias compared to the  $s'$ -form factor. Moreover, a comparison with the LDOS map at the negative bias  $\omega = -0.25t$  plotted in the Figure 5-8(b) shows a spatial phase difference of  $\pi$  between them, similar to the case of APCDW state discussed in Section 5.3.1. In the following paragraphs, we make these statements more quantitative by calculating the bias

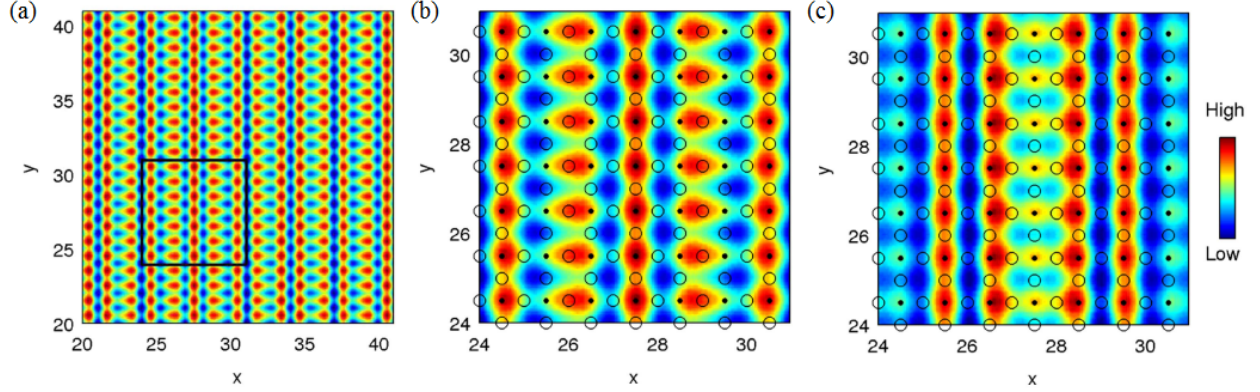


Figure 5-8. Continuum LDOS map at  $\omega = \pm 0.25t$  and at the height  $z \approx 5 \text{ \AA}$  above BiO plane. (a) LDOS map at  $\omega = 0.25t$  in a range of  $20 \times 20$  unit cells. (b) Zoomed-in view of the area marked by square in (a). Black dots and open circles represent position of Cu and O atoms, respectively, in the CuO plane underneath. (c) LDOS map at  $\omega = -0.25t$  in the same region as in (b).

dependence of form factors and spatial phase difference using Equations 5–23 and 5–24, respectively.

Figure 5-9(a) shows the continuum LDOS spectrum at the Cu,  $O_x$ , and  $O_y$  sites in the unit cell  $[25, 25]$  at a height  $z \approx 5 \text{ \AA}$  above the BiO plane. The inset shows the position of the Cu and O sites, marked by a black dot and circles, respectively, with reference to the continuum LDOS map shown in the Figure 5-8(b). The breaking of four-fold rotational symmetry is evident from the different LDOS spectrum at  $O_x$  and  $O_y$  sites. Moreover, A small V-shape structure is present near  $\omega = 0$  as a consequence of the uniform component of the  $d$ -wave pairing order parameter. Furthermore, two sets of coherence peaks at the energies  $\approx \pm 0.21t$  and  $\approx \pm 0.37t$  are present as in the case of lattice LDOS (Figure 5-7(c)). At present, the continuum LDOS does not bear a close resemblance to experimental data (see Figure 5-9(c)). However, the higher energy coherence peaks are expected to be smeared by the inelastic scattering processes [126] considered to be intrinsically present in the optimal-to-underdoped cuprates [208, 209]. Following [126], we model such processes by a linear-in- $\omega$  scattering rate  $\Gamma = \alpha|\omega|$ . The constant  $\alpha$  was determined to be in the range of 0.25 – 0.33 for the local spectral gap lying in the range 80 – 100 meV in the underdoped BSCCO [126]. We replace the artificial broadening  $i0^+$  in

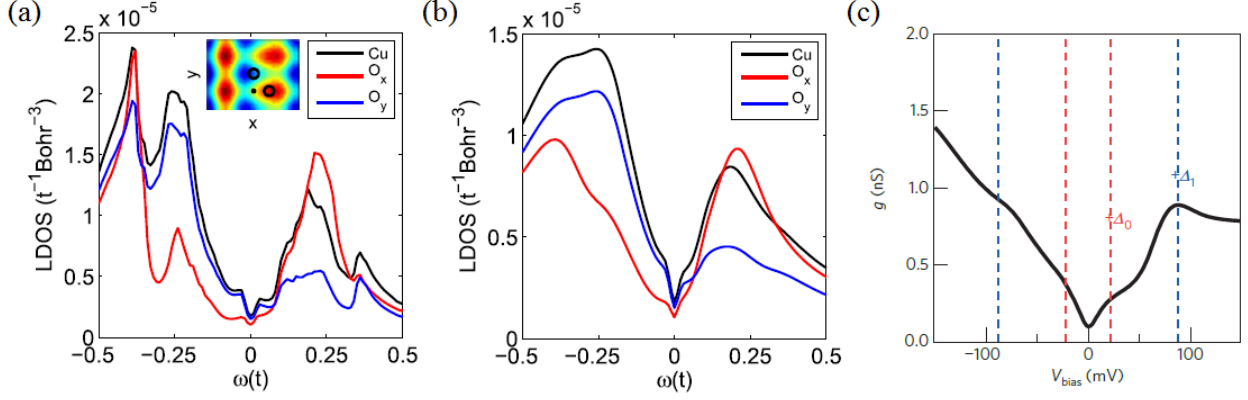


Figure 5-9. Continuum LDOS spectrum registered above Cu,  $O_x$  and  $O_y$  sites in the unit cell  $[25, 25]$  at a height  $z \approx 5 \text{ \AA}$  above the BiO plane (a) without, and (b) with  $\Gamma = \alpha|\omega|$  inelastic scattering;  $\alpha = 0.25$  as extracted in [126]. The location of the unit cell can be referred from Figure 5-8(b) as shown in the inset. Dots and open circles represent Cu and O atoms, respectively. (c) A typical tunneling conductance spectrum over a Cu site in BSCCO sample with 6% hole doping. Reprinted by permission from Macmillan Publishers Ltd: Nature [66], copyright 2015.

the Green's function, defined in Equation 5-21, by  $i0^+ + i\Gamma$  to incorporate the effects of the inelastic scattering in our analysis. Figure 5-9(b) shows the continuum LDOS spectrum thus obtained for  $\alpha = 0.25$ . Clearly, the higher energy coherence peaks are significantly broadened and can not be resolved any more. The spectra are very similar to the STM conductance spectra taken over various Cu and O sites in [35]. For a comparison, we show the typical tunneling conductance spectra taken over a Cu site in the charge ordered state of the superconducting BSCCO at 6% hole-doping in Figure 5-8(c) [66]. Here,  $\Delta_0$  is the nodal superconducting gap beyond which equilibrium Bogoliubov quasiparticles cease to exist, whereas  $\Delta_1$  is considered to be the pseudogap. The corresponding features in our model, as seen in Figure 5-8(b), are associated with the uniform component of the superconducting gap and the lower PDW coherence peak. Interestingly, the energy scales in the two figures are also similar, given that the bare NN hopping  $t$  in BSCCO is  $300 - 400 \text{ meV}$  [124].

The bias dependence of the intra-unit cell form factors at wavevector  $\mathbf{q} = [0.3, 0]$ , derived from the continuum LDOS in the nPDW state using Equation 5-23, is plotted in

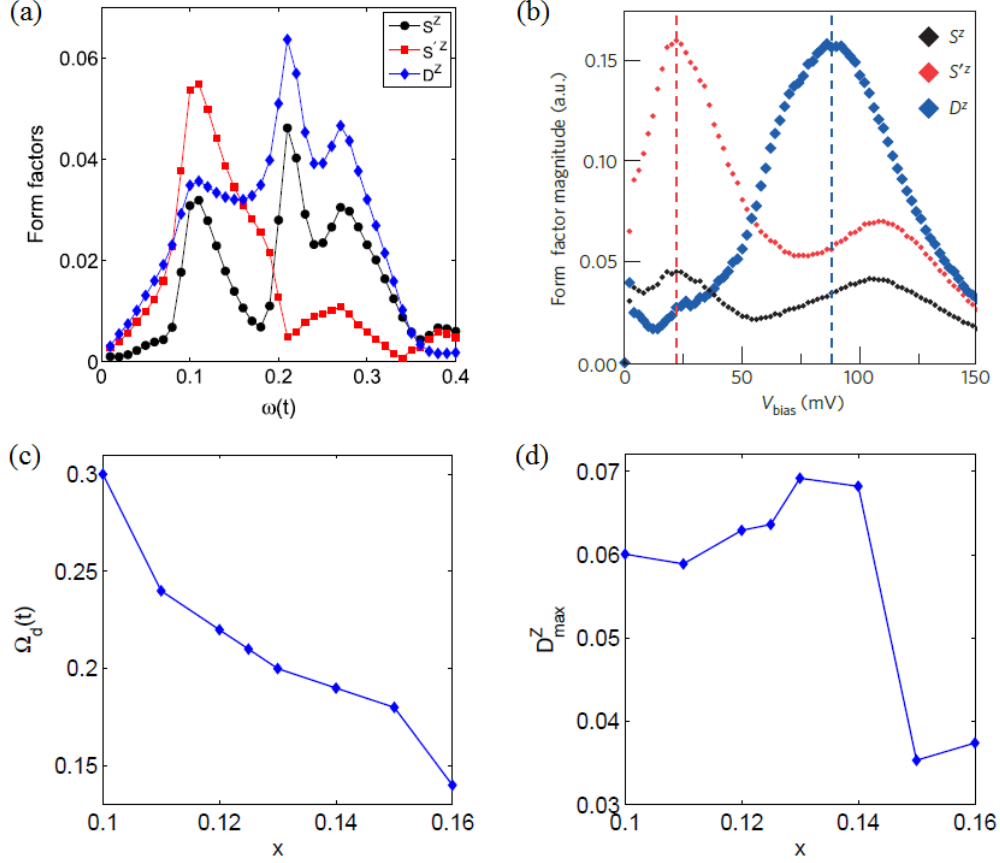


Figure 5-10. (a) Bias dependence of the form factors at  $x = 0.125$  computed from Equation 5-23. (b) Bias dependence of the form factors as observed in the STM experiment. Reprinted by permission from Macmillan Publishers Ltd: Nature [66], copyright 2015. Doping dependence of (c) energy at which  $d$ -form factor peaks ( $\Omega_d$ ) and (d) corresponding magnitude ( $D^Z_{\text{max}}$ ).

Figure 5-10(a). The corresponding experimental result [66] is reproduced in the Figure 5-10(b). We find that the  $s'$ - and  $d$ -form factors display peaks at a lower ( $\Omega_{s'} = 0.11t$ ) and a higher energy ( $\Omega_d = 0.21t$ ), respectively, in agreement with the experiment [66]. Comparing with lattice LDOS (Figure 5-7(c)) and continuum LDOS spectra (Figure 5-9(a)), we find that the  $d$ -form factor peaks at the energy corresponding to the lower coherence peak in the LDOS occurring due to hybridization of ABS as explained in the Section 5.3.1. Thus, we can conclude that the  $d$ -form factor nature of the charge order is intimately related to the PDW character. A more convincing analysis to support this claim is presented at the end of this section. We note that the relative magnitude of form

factors close to  $\omega = 0$  is different from the experimental results. Also, we find that the  $s$ -form factor is comparable, but lower at all biases, to the  $s'$ - and  $d$ -form factors, whereas in the experiment it is much more suppressed. The doping dependence of the energy at which the  $d$ -form factor peaks ( $\Omega_d$ ) and the corresponding peak value ( $D_{max}^Z$ ) is plotted in Figures 5-10(b) and (c). We find that  $\Omega_d$  decreases monotonically with increasing hole-doping ( $x$ ) whereas  $D_{max}^Z$  shows a non-monotonic behavior; first, it increases slowly with  $x$ , attains a maximum at  $x = 0.13$ , and drops rapidly with a slight increase in doping. The doping dependence of  $D_{max}^Z$  is very similar to the experimentally determined intensity of the density modulation wavevector [65], which can be considered as an analogue of  $D_{max}^Z$ . We note that no other theory has been able to calculate bias dependence of intra-unit cell observables. Figures 5-10(c) and (d) are predictions of our model which can be easily tested by repeating the experimental work presented in [66] for several hole dopings.

In Figure 5-11(a), we plot the calculated bias dependence of the average spatial phase difference ( $\Delta\phi$ ) between  $d$ -form factor modulations at positive and negative biases in the nPDW state, evaluated using Equation 5-24. The corresponding experimental result [66] is reproduced in Figure 5-11(b). In agreement with experiment, we find that at low energies  $\omega < 0.08t$ ,  $\Delta\phi$  is 0, and sharply increases afterwards achieving the value  $\pi$  at  $\omega \approx 0.12t$ . The transition occurs near the energy where the  $d$ -form factor becomes dominant (compare with Figure 5-10(a)). The doping dependence of the energy  $\Omega_\pi$  at which the spatial phase changes to  $\pi$  is shown in Figure 5-11(c). We find that  $\Omega_\pi$  decreases monotonically with hole-doping. This result is in agreement with the  $\Omega_\pi$  extracted from the bias-dependence of  $\Delta\phi$  at additional dopings  $x = 0.06, 0.17$  presented in the supplementary information of [66].

Hamidian et al. [66] attributed the particular bias dependence of the form factors and spatial phase difference to the  $d$ -form factor nature of charge order, where anti-phase modulations occurs at the two inequivalent O atoms in the  $\text{CuO}_2$  unit cell. However, in

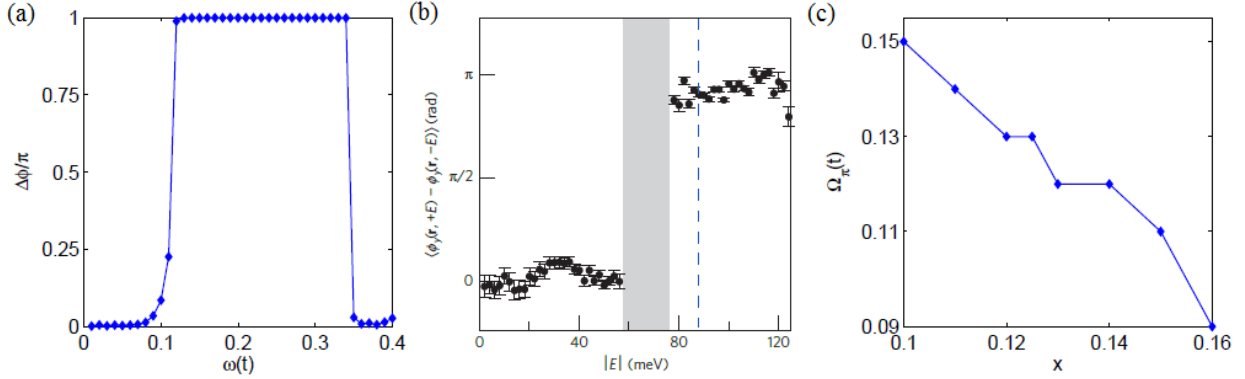


Figure 5-11. (a) Bias dependence of average spatial phase difference ( $\Delta\phi$ ) defined in Equation 5–24. (b) Bias dependence of  $\Delta\phi$  as observed in the STM experiments [66]. Reprinted by permission from Macmillan Publishers Ltd: Nature [66], copyright 2015. (c) Doping dependence of the energy  $\Omega_\pi$  at which the initial  $\pi$  phase jump in  $\Delta\phi$  takes place.

our analysis, we find that the charge order is driven by the PDW order. Moreover, the correspondence between the energy at which the  $d$ -form factor peaks, and the particular coherence peaks in the LDOS spectrum arising due to the PDW order, strongly suggest that the latter is pivotal to get the bias dependence of the form factors and spatial phase difference as seen in the experiment.

We further substantiate this claim by disentangling uniform superconductivity, CDW, and PDW orders intertwined in the nPDW state "by hand". First, we keep only PDW order and turn off the CDW order. This is done by taking the mean-fields in the nPDW state and replacing the spatially varying hole density ( $\delta_i$ ) and bond fields ( $\chi_{ij\sigma}^v$ ) in the BdG equation (Equation 5–16) by the corresponding quantities ( $\delta_0$  and  $\chi_0^v$ ) in the uniform  $d$ -wave superconducting state, i.e.  $\delta_i \rightarrow \delta_0$  and  $\chi_{ij\sigma}^v \rightarrow \chi_0^v$ . The pair field  $\Delta_{ij\sigma}^v$  is kept the same (and thus modulating) as in the nPDW state. The chemical potential is adjusted to yield the correct average electron filling. We solve Equation 5–16 with these changes and calculate the lattice LDOS, form factors, and the spatial phase difference; results are shown in Figures 5-12(a), (b), and (c), respectively. Comparing Figures 5-12(a) and 5-7(c), we conclude the coherence peaks come from the PDW order and artificially setting the charge modulation to zero has a small effect on it. Moreover, the peak in  $d$ -form

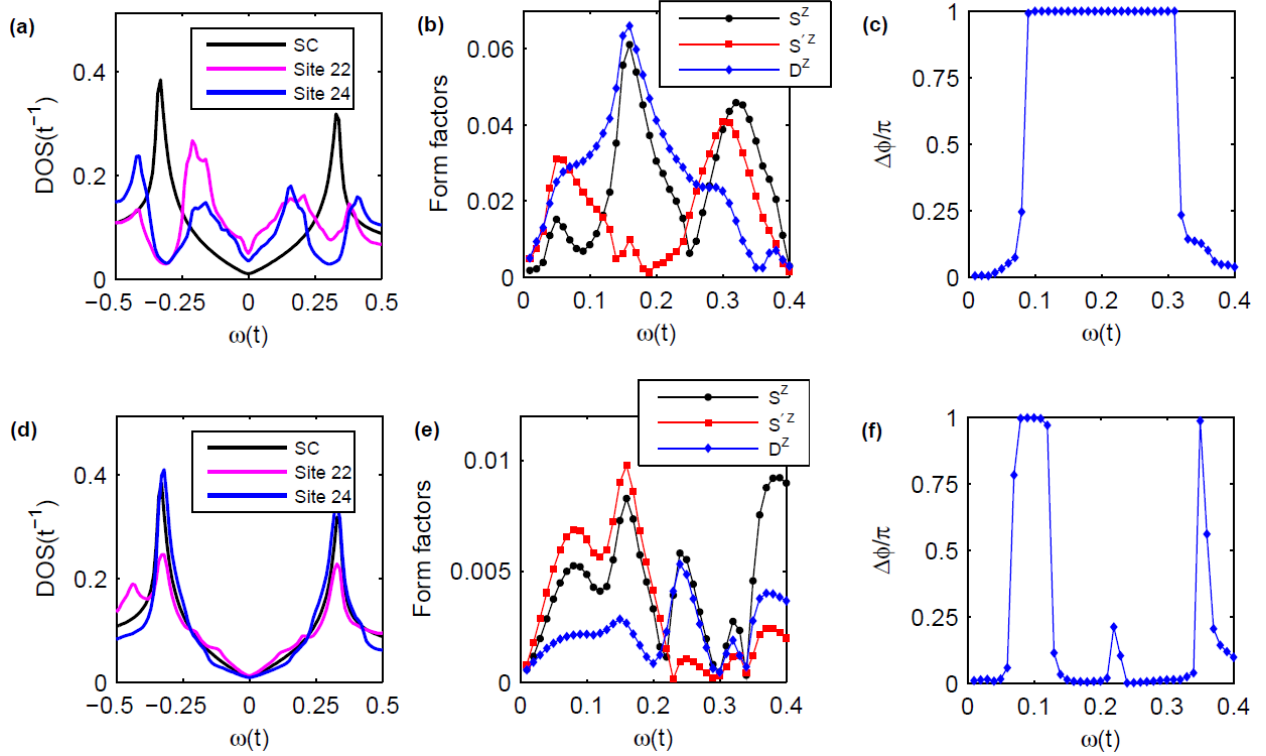


Figure 5-12. (a)-(c) Lattice LDOS, form factors and average spatial phase difference ( $\Delta\phi$ ) in the case when nPDW charge and bond modulations are set to zero "by hand" keeping only pair field modulations. (d)-(f) Lattice LDOS, form factors and average spatial phase difference ( $\Delta\phi$ ), respectively, in the case when nPDW pair field modulations are set to zero "by hand" keeping charge and bond modulations.

factor survives even in the absence of the CDW order. Furthermore, the bias dependence of  $\Delta\phi$  is also very similar to the nPDW state (see Figure 5-11(a)). Thus, we find that the qualitative features of the bias dependence of various quantities in the nPDW state remains intact even if the CDW order is artificially turned off. Finally, we do the similar exercise again, but now setting the PDW order to zero "by hand" and keeping the CDW and uniform superconductivity. This is achieved by taking the mean-fields in the nPDW state and replacing the modulating pair field  $\Delta_{ij\sigma}^v$  in Equation 5-16 by the corresponding quantity ( $\Delta_0^v$ ) in the uniform  $d$ -wave superconducting state while keeping the modulating bond field and hole density unchanged. Results are shown in Figures 5-12(d)-(f). Clearly, the lattice LDOS does not show much difference from the uniform  $d$ -wave superconducting

state. More importantly, the bias dependence of the form factors and spatial phase difference look very different from the nPDW state and the experimental observation. Thus, we can conclude that the PDW order is crucial to yield the bias dependence of LDOS, form factors, and spatial phase difference as observed in the STM experiments.

#### 5.4 Conclusion

In this chapter, we studied charge ordered states in the  $t - t' - J$  model, which has been widely used in past to understand the phenomenology of the underdoped cuprates from a strong coupling perspective. Using the renormalized mean-field theory (Gutzwiller approximation), along with a partial Fourier transform scheme substantially reducing the computational cost, we obtained the commensurate and incommensurate charge ordered states which are nearly degenerate to the uniform  $d$ -wave superconducting state. The incommensurate nPDW state intertwines CDW, PDW, and uniform superconductivity and has properties very similar to the charge ordered states observed in cuprates in STM experiments [35, 36, 66]. Particularly, the ladder-like real-space pattern of the continuum LDOS are similar to what has been observed in BSCCO and NaCCOC [35]. Moreover, the bias dependence of continuum LDOS, intra-unit cell form factors, and spatial phase difference in the nPDW state are in good agreement with the experiments [66].

We have used a Wannier function based method to calculate the Cu and O sublattice LDOS and obtained the bias-dependent form factors and spatial phase difference in a manner similar to the experiments [66]. This is a qualitative improvement over the theoretical schemes used previously in literature which considered static form factors derived from the renormalization of the NN hoppings. We found that in the nPDW state the  $s'$ -form factor dominates at lower energies, whereas the  $d$ -form factor dominates at higher energies, in agreement with the STM results [66]. Moreover, the  $d$ -form factor peak amplitude shows a non-monotonic behavior with respect to the hole doping, whereas the energy corresponding to the peak decreases monotonically with increasing doping. The average spatial phase difference in the nPDW state shows a jump from 0 to  $\pi$  at an energy

scale where the  $d$ -form factor exceeds the  $s'$ -form factor as seen in the STM experiments [66]. Furthermore, the energy at which the  $\pi$  phase shift occurs decreases monotonically with increasing hole doping, similar to experiment. Finally, we showed that the PDW character of the nPDW state is crucial to obtain the bias dependence of various quantities as seen in the experiments.

Although the nPDW state is not the ground state within Gutzwiller approximation, its energy difference with the uniform  $d$ -wave state which is the ground state is extremely small and can be overcome by small perturbations like electron-phonon coupling. We discussed the possibility that the disorder which is intrinsically present in cuprates can stabilize the nPDW state locally, yielding a short coherence length as seen in many STM experiments. Moreover, a magnetic field of  $O(10 \text{ T})$  can tilt the energy balance in favor of the nPDW state and result into a charge ordered state with a large coherence length as seen in the experiments. We leave these two scenarios for the future projects.

## CHAPTER 6 SUMMARY AND FINAL CONCLUSIONS

In this work, we have proposed a novel 'BdG+W' method, combining solutions of the lattice Bogoliubov-de Gennes equations and first principles Wannier functions, to theoretically compute the continuum LDOS at typical STM tip positions which can be directly compared with the experimental STM conductance. This method yields sub-unit cell spatial resolution and captures the effects of all atoms in the unit cell through Wannier function, without any substantial increase of computational complexity compared to the conventional BdG equations. Although the BdG+W method is quite general, we have mainly focused on its application to the problem of inhomogeneous states in cuprates and FeSCs. These are layered materials where the layer exposed to the STM tip is different from the 'active' layer (CuO layer in cuprates and Fe-layer in FeSCs) responsible for superconductivity. The effect of intervening layers, which is often ignored but can lead to a non-trivial tunneling paths, is easily accounted for the BdG+W method via first principles Wannier functions.

In Chapter 2, we derived an elementary expression for the continuum Green's function in terms of lattice Green's functions, using a basis transformation from the lattice to 3D continuum space with Wannier functions as matrix elements, which can be used to obtain continuum LDOS at the STM tip position. Moreover, we presented an efficient numerical scheme to solve the multi-orbital BdG equations on the lattice and combine their solution with Wannier function to obtain the continuum LDOS.

As a first application of the BdG+W method, we studied the non-magnetic impurity-induced states in the FeSe superconductor in Chapter 3. We started with a DFT derived 10-orbital tight-binding model and a corresponding Wannier basis to describe the normal state of FeSe. Next, to introduce the superconductivity, we calculated pair-potentials via a spin-fluctuation theory calculation within the random phase approximation. The superconducting state thus obtained was found to have  $s_{\pm}$  gap

symmetry. Further, by solving the 10-orbital BdG equations self-consistently, we found that a strong non-magnetic impurity, modeled simply as an on-site repulsive potential, induces bound states in the  $s_{\pm}$  superconducting gap. Moreover, the continuum LDOS map and topograph obtained above the Se layer at the bound state energy yields an atomic-scale dimer like pattern around the impurity position that is very similar to the geometric dimer states observed in FeSe [63] and other FeSCs [49, 77, 79]. This is the first and only explanation of these states to our knowledge.

In Chapter 4, we used the BdG+W method to study Zn and Ni impurity-induced states in the superconducting BSCCO. We first obtained the 1-band tight-binding model and corresponding Cu- $d_{x^2-y^2}$  Wannier function using first principles calculations. We showed that the  $d_{x^2-y^2}$  symmetry of the Wannier function leads to a change of the low energy spectral features in the homogeneous  $d$ -wave superconducting state from a V-shaped spectrum in the lattice LDOS to a more U-shaped spectrum in the continuum LDOS. This indeed corresponds to experimental data in the literature for optimal-to-overdoped cuprates, although it had never been noted before, to our knowledge. Next, modeling Zn as a strong attractive on-site potential scatterer in a  $d$ -wave superconductor, we solved the lattice BdG equations and found, as others had before us, that it induces a sharp in-gap resonance state. Further, the lattice LDOS showed a minimum right at the Zn site and maxima at the nearest-neighbor sites, as predicted in earlier theories, but in contrast to the STM experiments [60] which show an opposite intensity pattern. We resolved this longstanding paradox by calculating continuum LDOS map a few Å above BiO plane, where the STM tip would be typically located, which displayed excellent agreement with the STM results [60]. We found that the intensity maximum at the impurity site in BSCCO can be attributed to the electron transfer from nearest-neighbor unit cells via apical oxygen atoms. Finally, we studied the Ni impurity problem in BSCCO by using a simple model of a magnetic impurity with weak on-site potential and exchange scattering, and showed that such an impurity induced

two spin-polarized in-gap resonance states. Moreover, as in the case of Zn problem, the continuum LDOS maps at the resonance energies displayed excellent agreement with the corresponding STM results [64].

In Chapter 5, we addressed a very recent STM experiment [66] on the charge ordered state in BSCCO that has captured the attention of the high- $T_c$  community. By solving the  $t - t' - J$  model within renormalized mean-field theory (Gutzwiller approximation), we obtained two kinds of unidirectional charge ordered states, namely the commensurate anti-phase charge density wave (APCDW), and incommensurate nodal pair density wave (nPDW) states, which had been earlier shown to possess a dominant  $d$ -form factor [190]. Using the Wannier function based approach developed in Chapter 2, we calculated the continuum LDOS at typical STM tip positions, and subsequently obtained the bias dependence of the intra-unit cell form factors and spatial phase difference in the APCDW and the nPDW state, closely following the experimental analysis [65, 66]. We found that the nPDW state which intertwines charge density wave, pair density wave (PDW), and uniform superconductivity, has characteristics very similar to the STM observations [66, 125]. The continuum LDOS maps in the nPDW state shows ladder-like spatial patterns similar to the experiments [125]. Moreover, the continuum LDOS above Cu sites has a nodal spectrum, arising from the uniform component of  $d$ -wave superconducting order parameter, that resembles very closely the STM tunneling conductance spectrum [66, 125] once the effects of inelastic scattering [126] are properly taken into account. Furthermore, in the nPDW state, the  $s'$ -form factor dominates at lower energies, whereas the  $d$ -form factor dominates at higher energies, in agreement with the STM results [66]. Finally, the average spatial phase difference in the nPDW state shows a jump from 0 to  $\pi$  at an energy scale where the  $d$ -form factor exceeds the  $s'$ -form factor as seen in the STM experiments [66].

In this work, we not only explained the past STM observations that had defied a microscopic explanation for a long time, for example Zn and Ni impurity patterns in

BSCCO, and geometric dimer states in FeSCs, but also made new predictions which can be tested experimentally to validate our theory. In Section 4.3, we showed that the continuum LDOS in superconducting overdoped BSCCO at a typical STM tip height and bias  $\omega \rightarrow 0$  varies as  $|\omega|^3$ , in contrast to the commonly assumed linear-in- $|\omega|$  variation. With sub-meV resolution of the modern STM apparatus, this result can be directly checked by comparing goodness of fit for the cubic and linear curves to the measured low-bias differential tunneling conductance spectra in overdoped BSCCO. In Section 5.3.2, we predict that the bias at which the  $d$ -form factor acquires the largest value, and the bias at which the spatial phase difference first changes from 0 to  $\pi$ , should decrease with increasing hole-doping, whereas the amplitude of the  $d$ -form factor should first increase, achieve a maximum, and drop rapidly until the charge order vanishes with further hole doping. Again, these predictions can be easily tested by repeating the experimental analysis presented in [66] for BSCCO samples with different hole dopings. The predictive power of the BdG+W approach is also reflected in a recent combined theoretical and STM study [109] of superconducting LiFeAs, a widely studied FeSC, where some of the authors first predicted the registration of Li or As states in the STM topography as a function of tip-sample distance and setpoint current using the Wannier function based approach, which was later verified by other co-authors via actual STM measurements. Finally, in a very recent investigation, which is still a work in progress, we find that the Wannier function in another cuprate compound NaCCOC has a very similar shape to that in BSCCO, in spite of a very different crystal structure. It strongly suggests that if the STM experiments with Zn and Ni doping are repeated for NaCCOC, the same spatial pattern of the impurities should be observed as in BSCCO, despite the fact that the intervening layers between the surface and the  $\text{CuO}_2$  plane are quite different in the two materials. This is another non-trivial prediction which can be easily tested by STM experiments.

The BdG+W method presented in this thesis represents a qualitative improvement over the conventional methods such as lattice BdG equations and T-matrix, used

extensively in literature to understand the STM experiments on layered superconductors like cuprates and FeSCs. First and foremost, it allows the calculation of the continuum LDOS at a typical STM tip position, which can be directly compared with the STM tunneling conductance at low temperatures. In contrast to the previously proposed methods [62, 120, 121], which are similar in spirit but tailor-made for a particular compound (BSCCO) and do not treat inhomogeneities and superconductivity on the same footing, the BdG+W method provides a systematic framework to study any superconductor at the mean-field level in the context of STM experiments. It captures the local symmetry internal to the unit cell and yields a sub-unit cell spatial resolution, comparable to the STM results, enabling a better visualization of the atomic-scale phenomena in inhomogeneous superconductors. Furthermore, the QPI pattern calculated using BdG+W method captures wavevectors in all Brillouin zones, in contrast to the conventional lattice calculations which yield wavevectors only in the first Brillouin zone, leading to a qualitative improvement when compared with the experiment. Looking back on the history of STM experiments on cuprates and FeSCs, one finds many instances where the crude level of theory led to misunderstanding of experimental data. We anticipate that with the advent of computationally inexpensive and user-friendly *ab initio* platforms, experimental groups will increasingly adopt our approach to understand their results.

There are some important directions in which the work presented in this thesis can be expanded. The method itself can be improved to include the effects of correlations and impurities on the Wannier functions. As an initial approximation, we assumed that the Wannier functions around impurity sites are unaffected by the impurity substitution, and ignored the effects of electronic correlations in the normal state. The first assumption can be relaxed by obtaining Wannier functions as well as impurity potentials from the first-principles calculation for a single impurity in the normal state within the supercell approximation [210]. The correlation effects on the Wannier function can be accounted

for via LDA+U and LDA+DMFT methods [138, 211, 212]. Apart from improving the method, there are few open questions from the work presented in Chapter 4 and 5 that I would like to address in future. First, how does the continuum LDOS change from a more U-shaped to V-shaped spectral dependence when moving from overdoped cuprate samples (sample areas) to optimally doped samples (see Section 4.3 for details)? Second, can disorder or magnetic field stabilize the charge ordered states in the  $t - J$  model as the ground state (see Section 5.3 for details)? If the latter can be shown to be correct, we will have established a consistent picture of the charge ordered phases over the entire cuprate phase diagram, which would constitute a major step forward in understanding high temperature superconductivity.

APPENDIX A  
DERIVATION OF BOGOLIUBOV-DE GENNES EQUATIONS

Following the discussion in Section 2.2.2, we compute the commutator  $[H_{\text{MF}}, c_{i\mu\sigma}]$  for the two definitions of mean-field Hamiltonian as in Equations 2-5 and 2-8. If the transformation given in Equation 2-7 diagonalizes the mean-field Hamiltonian, then the two commutators must be equal and by comparing the coefficients of  $\gamma$  operators we will get the BdG equations.

$$\begin{aligned}
[H_{\text{MF}}^0, c_{i'\mu'\sigma'}] &= \left[ \sum_{ij\mu\nu\sigma} t_{ij}^{\mu\nu} c_{i\mu\sigma}^\dagger c_{j\nu\sigma} - \mu_0 \sum_{i\mu\sigma} c_{i\mu\sigma}^\dagger c_{i\mu\sigma}, c_{i'\mu'\sigma'} \right] \\
&= \sum_{ij\mu\nu\sigma} (t_{ij}^{\mu\nu} - \mu_0 \delta_{ij} \delta_{\mu\nu}) [c_{i\mu\sigma}^\dagger c_{j\nu\sigma}, c_{i'\mu'\sigma'}] \\
&= \sum_{ij\mu\nu\sigma} (t_{ij}^{\mu\nu} - \mu_0 \delta_{ij} \delta_{\mu\nu}) (-\delta_{ii'} \delta_{\mu\mu'} \delta_{\sigma\sigma'} c_{j\nu\sigma}) \\
&= - \sum_{j\nu} (t_{i'j}^{\mu'\nu} - \mu_0 \delta_{i'j} \delta_{\mu'\nu}) c_{j\nu\sigma'}. \tag{A-1}
\end{aligned}$$

$$\begin{aligned}
[H_{\text{MF}}^{\text{BCS}}, c_{i'\mu'\sigma'}] &= \left[ - \sum_{ij\mu\nu} (\Delta_{ij}^{\mu\nu} c_{i\mu\uparrow}^\dagger c_{j\nu\downarrow}^\dagger + \text{H.c.}), c_{i'\mu'\sigma'} \right] \\
&= - \sum_{ij\mu\nu} (\Delta_{ij}^{\mu\nu} [c_{i\mu\uparrow}^\dagger c_{j\nu\downarrow}^\dagger, c_{i'\mu'\sigma'}] + \Delta_{ij}^{\mu\nu*} [c_{j\nu\downarrow} c_{i\mu\uparrow}, c_{i'\mu'\sigma'}]) \\
&= - \sum_{ij\mu\nu} (\Delta_{ij}^{\mu\nu} c_{i\mu\uparrow}^\dagger \{c_{j\nu\downarrow}^\dagger, c_{i'\mu'\sigma'}\} - \Delta_{ij}^{\mu\nu} \{c_{i\mu\uparrow}^\dagger, c_{i'\mu'\sigma'}\} c_{j\nu\downarrow}^\dagger) \\
&= - \sum_{ij\mu\nu} (\Delta_{ij}^{\mu\nu} c_{i\mu\uparrow}^\dagger \delta_{j i'} \delta_{\nu\mu'} \delta_{\downarrow\sigma'} - \Delta_{ij}^{\mu\nu} \delta_{i i'} \delta_{\mu\mu'} \delta_{\uparrow\sigma'} c_{j\nu\downarrow}^\dagger).
\end{aligned}$$

Thus,

$$\begin{aligned}
[H_{\text{MF}}^{\text{BCS}}, c_{i'\mu'\uparrow}] &= \sum_{j\nu} \Delta_{i'j}^{\mu'\nu} c_{j\nu\downarrow}^\dagger \\
[H_{\text{MF}}^{\text{BCS}}, c_{i'\mu'\downarrow}] &= \sum_{j\nu} \Delta_{j i'}^{\nu\mu'} c_{j\nu\uparrow}^\dagger, \tag{A-2}
\end{aligned}$$

$$\begin{aligned}
[H_{\text{MF}}^{\text{imp}}, c_{i'\mu'\sigma'}] &= \left[ \sum_{\mu\sigma} V_{\text{imp}} c_{i^*\mu\sigma}^\dagger c_{i^*\mu\sigma}, c_{i'\mu'\sigma'} \right] \\
&= V_{\text{imp}} \sum_{\mu\sigma} [c_{i^*\mu\sigma}^\dagger c_{i^*\mu\sigma}, c_{i'\mu'\sigma'}]
\end{aligned}$$

$$\begin{aligned}
&= V_{\text{imp}} \sum_{\mu\sigma} (-\delta_{i^*i'} \delta_{\mu\mu'} \delta_{\sigma\sigma'} c_{i^*\mu\sigma}) \\
&= -V_{\text{imp}} \delta_{i^*i'} c_{i'\mu'\sigma'}.
\end{aligned} \tag{A-3}$$

From Equations A-1, A-2, and A-3

$$\begin{aligned}
[H_{\text{MF}}, c_{i'\mu'\uparrow}] &= -\sum_{j\nu} t_{i'j}^{\mu'\nu} c_{j\nu\uparrow} + \sum_{j\nu} \Delta_{i'j}^{\mu'\nu} c_{j\nu\downarrow}^\dagger - V_{\text{imp}} \delta_{i^*i'} c_{i'\mu'\uparrow} \\
&= -\sum_{j\nu} \left( \xi_{i'j}^{\mu'\nu} c_{j\nu\uparrow} - \Delta_{i'j}^{\mu'\nu} c_{j\nu\downarrow}^\dagger \right),
\end{aligned} \tag{A-4}$$

where,  $\xi_{ij}^{\mu\nu} = t_{ij}^{\mu\nu} - \delta_{ij} \delta_{\mu\nu} \mu_0 + \delta_{i^*i} \delta_{\mu\nu} \delta_{ij} V_{\text{imp}}$ . Similarly,

$$\begin{aligned}
[H_{\text{MF}}, c_{i'\mu'\downarrow}] &= -\sum_{j\nu} t_{i'j}^{\nu\mu'} c_{j\nu\downarrow} - \sum_{j\nu} \Delta_{j i'}^{\nu\mu'} c_{j\nu\uparrow}^\dagger - V_{\text{imp}} \delta_{i^*i'} c_{i'\mu'\downarrow} \\
&= -\sum_{j\nu} \left( \xi_{i'j}^{\nu\mu'} c_{j\nu\downarrow} + \Delta_{j i'}^{\nu\mu'} c_{j\nu\uparrow}^\dagger \right).
\end{aligned} \tag{A-5}$$

Now, we will express commutators in terms of  $\gamma$  operators using Equation 2-7,

$$\begin{aligned}
[H_{\text{MF}}, c_{i'\mu'\uparrow}] &= -\sum_{j\nu} \left[ \xi_{i'j}^{\mu'\nu} \left( \sum_n u_{j\nu\uparrow}^n \gamma_{n\uparrow} + v_{j\nu\uparrow}^{n*} \gamma_{n\downarrow}^\dagger \right) - \Delta_{i'j}^{\mu'\nu} \left( \sum_n u_{j\nu\downarrow}^{n*} \gamma_{n\downarrow}^\dagger + v_{j\nu\downarrow}^n \gamma_{n\uparrow} \right) \right] \\
&= \sum_{nj\nu} \left[ \left( -\xi_{i'j}^{\mu'\nu} u_{j\nu\uparrow}^n + \Delta_{i'j}^{\mu'\nu} v_{j\nu\downarrow}^n \right) \gamma_{n\uparrow} + \left( \Delta_{i'j}^{\mu'\nu} u_{j\nu\downarrow}^{n*} - \xi_{i'j}^{\mu'\nu} v_{j\nu\uparrow}^{n*} \right) \gamma_{n\downarrow}^\dagger \right],
\end{aligned} \tag{A-6}$$

$$\begin{aligned}
[H_{\text{MF}}, c_{i'\mu'\downarrow}] &= -\sum_{j\nu} \left[ \xi_{i'j}^{\mu'\nu} \left( \sum_n u_{j\nu\downarrow}^n \gamma_{n\downarrow} + v_{j\nu\downarrow}^{n*} \gamma_{n\uparrow}^\dagger \right) + \Delta_{j i'}^{\nu\mu'} \left( \sum_n u_{j\nu\uparrow}^{n*} \gamma_{n\uparrow}^\dagger + v_{j\nu\uparrow}^n \gamma_{n\downarrow} \right) \right] \\
&= \sum_{nj\nu} \left[ \left( -\xi_{i'j}^{\mu'\nu} u_{j\nu\downarrow}^n - \Delta_{j i'}^{\nu\mu'} v_{j\nu\uparrow}^n \right) \gamma_{n\downarrow} + \left( -\Delta_{j i'}^{\nu\mu'} u_{j\nu\uparrow}^{n*} - \xi_{i'j}^{\mu'\nu} v_{j\nu\downarrow}^{n*} \right) \gamma_{n\uparrow}^\dagger \right].
\end{aligned} \tag{A-7}$$

Computing commutators using diagonalized Hamiltonian (Equation 2-8),

$$\begin{aligned}
[H_{\text{MF}}, c_{i'\mu'\sigma'}] &= \sum_{nn'\sigma} \left[ E_{n\sigma} \gamma_{n\sigma}^\dagger \gamma_{n\sigma}, u_{i'\mu'\sigma'}^{n'} \gamma_{n'\sigma'} + v_{i'\mu'\sigma'}^{n'*} \gamma_{n'\bar{\sigma}'}^\dagger \right] \\
&= \sum_{nn'\sigma} \left( E_{n\sigma} u_{i'\mu'\sigma'}^{n'} [\gamma_{n\sigma}^\dagger \gamma_{n\sigma}, \gamma_{n'\sigma'}] + E_{n\sigma} v_{i'\mu'\sigma'}^{n'*} [\gamma_{n\sigma}^\dagger \gamma_{n\sigma}, \gamma_{n'\sigma'}^\dagger] \right) \\
&= \sum_{nn'\sigma} \left[ E_{n\sigma} u_{i'\mu'\sigma'}^{n'} (-\delta_{nn'} \delta_{\sigma\sigma'} \gamma_{n\sigma}) + E_{n\sigma} v_{i'\mu'\sigma'}^{n'*} (\delta_{nn'} \delta_{\sigma\bar{\sigma}'} \gamma_{n\sigma}^\dagger) \right] \\
&= \sum_n \left[ (-E_{n\sigma'} u_{i'\mu'\sigma'}^n) \gamma_{n\sigma'} + (E_{n\bar{\sigma}'} v_{i'\mu'\sigma'}^{n*}) \gamma_{n\bar{\sigma}'}^\dagger \right],
\end{aligned}$$

$$[H_{\text{MF}}, c_{i'\mu'\uparrow}] = \sum_n \left[ (-E_{n\uparrow} u_{i'\mu'\uparrow}^n) \gamma_{n\uparrow} + (E_{n\downarrow} v_{i'\mu'\uparrow}^{n*}) \gamma_{n\downarrow}^\dagger \right]. \quad (\text{A-8})$$

$$[H_{\text{MF}}, c_{i'\mu'\downarrow}] = \sum_n \left[ (-E_{n\downarrow} u_{i'\mu'\downarrow}^n) \gamma_{n\downarrow} + (E_{n\uparrow} v_{i'\mu'\downarrow}^{n*}) \gamma_{n\uparrow}^\dagger \right]. \quad (\text{A-9})$$

Comparing Equations A-6 and A-8 and changing indices from  $i'\mu'$  to  $i\mu$ ,

$$\sum_{j\nu} (\xi_{ij}^{\mu\nu} u_{j\nu\uparrow}^n - \Delta_{ij}^{\mu\nu} v_{j\nu\downarrow}^n) = E_{n\uparrow} u_{i\mu\uparrow}^n, \quad (\text{A-10})$$

$$\sum_{j\nu} (\Delta_{ij}^{\mu\nu*} u_{j\nu\downarrow}^n - \xi_{ij}^{\mu\nu*} v_{j\nu\uparrow}^n) = E_{n\downarrow} v_{i\mu\uparrow}^n. \quad (\text{A-11})$$

Comparing Equations A-7 and A-9 and changing indices from  $i'\mu'$  to  $i\mu$ ,

$$\sum_{j\nu} (\xi_{ij}^{\mu\nu} u_{j\nu\downarrow}^n + \Delta_{ji}^{\nu\mu} v_{j\nu\uparrow}^n) = E_{n\downarrow} u_{i\mu\downarrow}^n, \quad (\text{A-12})$$

$$\sum_{j\nu} (-\Delta_{ji}^{\nu\mu*} u_{j\nu\uparrow}^{n*} - \xi_{ij}^{\mu\nu*} v_{j\nu\downarrow}^{n*}) = E_{n\uparrow} v_{i\mu\downarrow}^n. \quad (\text{A-13})$$

Equations A-10 and A-13 can be combined into a matrix equation

$$\sum_{j\nu} \begin{pmatrix} \xi_{ij}^{\mu\nu} & -\Delta_{ij}^{\mu\nu} \\ -\Delta_{ji}^{\nu\mu*} & -\xi_{ij}^{\mu\nu*} \end{pmatrix} \begin{pmatrix} u_{j\nu\uparrow}^n \\ v_{j\nu\downarrow}^n \end{pmatrix} = E_{n\uparrow} \begin{pmatrix} u_{i\mu\uparrow}^n \\ v_{i\mu\downarrow}^n \end{pmatrix}. \quad (\text{A-14})$$

Similarly, Equations A-12 and A-11 read

$$\sum_{j\nu} \begin{pmatrix} \xi_{ij}^{\mu\nu} & \Delta_{ji}^{\nu\mu} \\ \Delta_{ij}^{\mu\nu*} & -\xi_{ij}^{\mu\nu*} \end{pmatrix} \begin{pmatrix} u_{j\nu}^n \\ v_{j\nu}^n \end{pmatrix} = E_n \begin{pmatrix} u_{i\mu}^n \\ v_{i\mu}^n \end{pmatrix}. \quad (\text{A-15})$$

Equations A-14 and A-15 form two sets of BdG equations. If we apply the following particle-hole transformation in Equation A-14 then we get Equation A-15,

$$\begin{pmatrix} u_{j\nu\uparrow}^n \\ v_{j\nu\downarrow}^n \\ E_{n\uparrow} \end{pmatrix} \rightarrow \begin{pmatrix} v_{j\nu\uparrow}^{n*} \\ u_{j\nu\downarrow}^{n*} \\ -E_{n\downarrow} \end{pmatrix}. \quad (\text{A-16})$$

Thus, we need to solve only Equation A-14 and by using above correspondence, we can obtain the solution of Equation A-15. All subsequent expressions will be obtained in terms of the eigenvalues and eigenvectors of Equation A-14.

Now, we turn to the derivation for the mean-field quantities (Equation 2-10) in terms of the BdG solutions. The electron density can be expressed as

$$\begin{aligned}
n_{i\mu\sigma} &= \langle c_{i\mu\sigma}^\dagger c_{i\mu\sigma} \rangle \\
&= \sum_{nn'} \langle (u_{i\mu\sigma}^{n*} \gamma_{n\sigma}^\dagger + v_{i\mu\sigma}^n \gamma_{n\bar{\sigma}}) (u_{i\mu\sigma}^{n'} \gamma_{n'\sigma} + v_{i\mu\sigma}^{n'*} \gamma_{n'\bar{\sigma}}^\dagger) \rangle \\
&= \sum_{nn'} \left( u_{i\mu\sigma}^{n*} u_{i\mu\sigma}^{n'} \langle \gamma_{n\sigma}^\dagger \gamma_{n'\sigma} \rangle + v_{i\mu\sigma}^n v_{i\mu\sigma}^{n'*} \langle \gamma_{n\bar{\sigma}} \gamma_{n'\bar{\sigma}}^\dagger \rangle \right) \\
&= \sum_{nn'} \left( u_{i\mu\sigma}^{n*} u_{i\mu\sigma}^{n'} f(E_{n\sigma}) \delta_{nn'} + v_{i\mu\sigma}^n v_{i\mu\sigma}^{n'*} (1 - f(E_{n\bar{\sigma}})) \right) \\
&= \sum_{n, E_{n\sigma} > 0} |u_{i\mu\sigma}^n|^2 f(E_{n\sigma}) + \sum_{n, E_{n\bar{\sigma}} > 0} |v_{i\mu\sigma}^n|^2 (1 - f(E_{n\bar{\sigma}})). \tag{A-17}
\end{aligned}$$

Using Equation A-16,

$$\begin{aligned}
n_{i\mu\uparrow} &= \sum_{n, E_{n\uparrow} > 0} |u_{i\mu\uparrow}^n|^2 f(E_{n\uparrow}) + \sum_{n, E_{n\downarrow} > 0} |v_{i\mu\uparrow}^n|^2 (1 - f(E_{n\downarrow})) \\
&= \sum_{n, E_{n\uparrow} > 0} |u_{i\mu\uparrow}^n|^2 f(E_{n\uparrow}) + \sum_{n, -E_{n\uparrow} > 0} |u_{i\mu\uparrow}^{n*}|^2 (1 - f(-E_{n\uparrow})) \\
&= \sum_{n, E_{n\uparrow} > 0} |u_{i\mu\uparrow}^n|^2 f(E_{n\uparrow}) + \sum_{n, E_{n\uparrow} < 0} |u_{i\mu\uparrow}^n|^2 f(E_{n\uparrow}) \\
&= \sum_n |u_{i\mu\uparrow}^n|^2 f(E_{n\uparrow}). \tag{A-18}
\end{aligned}$$

Here sum runs over all eigenvalues of Equation A-14, both positive and negative.

Similarly,

$$\begin{aligned}
n_{i\mu\downarrow} &= \sum_{n, E_{n\downarrow} > 0} |u_{i\mu\downarrow}^n|^2 f(E_{n\downarrow}) + \sum_{n, E_{n\uparrow} > 0} |v_{i\mu\downarrow}^n|^2 (1 - f(E_{n\uparrow})) \\
&= \sum_{n, -E_{n\uparrow} > 0} |v_{i\mu\downarrow}^{n*}|^2 f(-E_{n\uparrow}) + \sum_{n, E_{n\uparrow} > 0} |v_{i\mu\downarrow}^n|^2 (1 - f(E_{n\uparrow})) \\
&= \sum_{n, E_{n\uparrow} < 0} |v_{i\mu\downarrow}^n|^2 (1 - f(E_{n\uparrow})) + \sum_{n, E_{n\uparrow} > 0} |v_{i\mu\downarrow}^n|^2 (1 - f(E_{n\uparrow}))
\end{aligned}$$

$$= \sum_n |v_{i\mu\downarrow}^n|^2 (1 - f(E_{n\uparrow})). \quad (\text{A-19})$$

The superconducting gap order parameter, defined in Equation 2-6, can be expressed as

$$\begin{aligned} \Delta_{ij}^{\mu\nu} &= V_{ij}^{\mu\nu} \langle c_{j\nu\downarrow} c_{i\mu\uparrow} \rangle \\ &= V_{ij}^{\mu\nu} \sum_{nn'} \langle \left( u_{j\nu\downarrow}^n \gamma_{n\downarrow} + v_{j\nu\downarrow}^{n*} \gamma_{n\uparrow}^\dagger \right) \left( u_{i\mu\uparrow}^{n'} \gamma_{n'\uparrow} + v_{i\mu\uparrow}^{n'*} \gamma_{n'\downarrow}^\dagger \right) \rangle \\ &= V_{ij}^{\mu\nu} \sum_{nn'} \left( u_{j\nu\downarrow}^n v_{i\mu\uparrow}^{n'*} \langle \gamma_{n\downarrow} \gamma_{n'\downarrow}^\dagger \rangle + u_{i\mu\uparrow}^{n'} v_{j\nu\downarrow}^{n*} \langle \gamma_{n\uparrow}^\dagger \gamma_{n'\uparrow} \rangle \right) \\ &= V_{ij}^{\mu\nu} \sum_{nn'} \left( u_{j\nu\downarrow}^n v_{i\mu\uparrow}^{n'*} (1 - f(E_{n\downarrow})) \delta_{nn'} + u_{i\mu\uparrow}^{n'} v_{j\nu\downarrow}^{n*} f(E_{n\uparrow}) \delta_{nn'} \right) \\ &= V_{ij}^{\mu\nu} \sum_{n, E_{n\downarrow} > 0} u_{j\nu\downarrow}^n v_{i\mu\uparrow}^{n*} (1 - f(E_{n\downarrow})) + V_{ij}^{\mu\nu} \sum_{n, E_{n\uparrow} > 0} u_{i\mu\uparrow}^n v_{j\nu\downarrow}^{n*} f(E_{n\uparrow}) \\ &= V_{ij}^{\mu\nu} \sum_{n, -E_{n\uparrow} > 0} v_{j\nu\downarrow}^{n*} u_{i\mu\uparrow}^n (1 - f(-E_{n\uparrow})) + V_{ij}^{\mu\nu} \sum_{n, E_{n\uparrow} > 0} u_{i\mu\uparrow}^n v_{j\nu\downarrow}^{n*} f(E_{n\uparrow}) \\ &= V_{ij}^{\mu\nu} \sum_n u_{i\mu\uparrow}^n v_{j\nu\downarrow}^{n*} f(E_{n\uparrow}). \end{aligned} \quad (\text{A-20})$$

Equations A-14, A-18, A-19, and A-20 form BdG equations that has to be solved self-consistently using the procedure described in Section 2.4. Once, solution is known we can construct single particle Green's function defined below,

$$G_{ij\sigma}^{\mu\nu}(t, t') = -i\theta(t - t') \langle [c_{i\mu\sigma}(t), c_{j\nu\sigma}^\dagger(t')]_+ \rangle. \quad (\text{A-21})$$

Here,  $\theta$  is the step function, and  $[\ ]_+$  represents the anti-commutator. To find the time evolution of  $c$  operators we have to find time evolution of the  $\gamma$  operators. Since the  $\gamma$  operators are the free quasiparticles (see Equation 2-8), their time evolution is given by following equation,

$$\gamma_{n\sigma}(t) = \gamma_{n\sigma} e^{-iE_{n\sigma}t}. \quad (\text{A-22})$$

Using Equation 2-7 and Equation A-22, we get

$$\begin{aligned} c_{i\mu\sigma}(t) &= \sum_n \left[ u_{i\mu\sigma}^n e^{-iE_{n\sigma}t} \gamma_{n\sigma} + v_{i\mu\sigma}^{n*} e^{iE_{n\bar{\sigma}}t} \gamma_{n\bar{\sigma}}^\dagger \right], \\ c_{i\mu\sigma}^\dagger(t) &= \sum_n \left[ u_{i\mu\sigma}^{n*} e^{iE_{n\sigma}t} \gamma_{n\sigma}^\dagger + v_{i\mu\sigma}^n e^{-iE_{n\bar{\sigma}}t} \gamma_{n\bar{\sigma}} \right]. \end{aligned} \quad (\text{A-23})$$

Using Equations A-23 and A-21, we find

$$\begin{aligned}
G_{ij\sigma}^{\mu\nu}(t, t') &= -i\theta(t - t') \left\langle \sum_{nn'} \left( u_{i\mu\sigma}^n u_{j\nu\sigma}^{n'*} e^{-iE_{n\sigma}t} e^{iE_{n'\sigma}t'} \delta_{nn'} + v_{i\mu\sigma}^{n*} v_{j\nu\sigma}^n e^{iE_{n\bar{\sigma}}t} e^{-iE_{n'\bar{\sigma}}t'} \delta_{nn'} \right) \right\rangle \\
&= -i\theta(t - t') \left\langle \sum_n \left( u_{i\mu\sigma}^n u_{j\nu\sigma}^{n'*} e^{-iE_{n\sigma}t} e^{iE_{n'\sigma}t'} \delta_{nn'} + v_{i\mu\sigma}^{n*} v_{j\nu\sigma}^n e^{iE_{n\bar{\sigma}}t} e^{-iE_{n'\bar{\sigma}}t'} \delta_{nn'} \right) \right\rangle \\
&= -i\theta(t - t') \sum_n \left[ u_{i\mu\sigma}^n u_{j\nu\sigma}^{n*} e^{-iE_{n\sigma}(t-t')} + v_{i\mu\sigma}^{n*} v_{j\nu\sigma}^n e^{iE_{n\bar{\sigma}}(t-t')} \right]. \tag{A-24}
\end{aligned}$$

Taking the Fourier transform of Equation A-24 yields the Green's function in frequency space,

$$\begin{aligned}
G_{ij\sigma}^{\mu\nu}(\omega) &= \int_{-\infty}^{\infty} d(t - t') G_{ij\sigma}^{\mu\nu}(t, t') e^{i\omega(t-t')}, \\
&= \sum_{n>0} \left[ \frac{u_{i\mu\sigma}^n u_{j\nu\sigma}^{n*}}{\omega - E_{n\sigma} + i0^+} + \frac{v_{i\mu\sigma}^{n*} v_{j\nu\sigma}^n}{\omega + E_{n\bar{\sigma}} + i0^+} \right]. \tag{A-25}
\end{aligned}$$

Here,  $0^+$  is the artificial broadening, taken to be much smaller than smallest physical energy in the problem, and  $n > 0$  indicates that the sum is to be performed over eigenstates with positive eigenvalues only. Now, we will express the above Greens function only in the terms of the solutions of Equation A-14.

$$\begin{aligned}
G_{ij\uparrow}^{\mu\nu}(\omega) &= \sum_{n, E_{n\uparrow} > 0} \frac{u_{i\mu\uparrow}^n u_{j\nu\uparrow}^{n*}}{\omega - E_{n\uparrow} + i0^+} + \sum_{n, E_{n\downarrow} > 0} \frac{v_{i\mu\uparrow}^{n*} v_{j\nu\uparrow}^n}{\omega + E_{n\downarrow} + i0^+} \\
&= \sum_{n, E_{n\uparrow} > 0} \frac{u_{i\mu\uparrow}^n u_{j\nu\uparrow}^{n*}}{\omega - E_{n\uparrow} + i0^+} + \sum_{n, -E_{n\uparrow} > 0} \frac{u_{i\mu\uparrow}^n u_{j\nu\uparrow}^{n*}}{\omega - E_{n\uparrow} + i0^+} \\
&= \sum_n \frac{u_{i\mu\uparrow}^n u_{j\nu\uparrow}^{n*}}{\omega - E_{n\uparrow} + i0^+}. \tag{A-26}
\end{aligned}$$

Here, we have used Equation A-16 in the second step. Now, the sum runs over all values of  $n$ . Similarly,

$$\begin{aligned}
G_{ij\downarrow}^{\mu\nu}(\omega) &= \sum_{n, -E_{n\uparrow} > 0} \frac{v_{i\mu\downarrow}^{n*} v_{j\nu\downarrow}^n}{\omega + E_{n\uparrow} + i0^+} + \sum_{n, E_{n\uparrow} > 0} \frac{v_{i\mu\downarrow}^{n*} v_{j\nu\downarrow}^n}{\omega + E_{n\uparrow} + i0^+} \\
&= \sum_n \frac{v_{i\mu\downarrow}^{n*} v_{j\nu\downarrow}^n}{\omega + E_{n\uparrow} + i0^+}. \tag{A-27}
\end{aligned}$$

## APPENDIX B SUPERCELL METHOD

The solution of the inhomogeneous BdG equations (Equation 2-9) on a  $N \times N$  lattice with  $N_o$  orbitals per lattice site yields  $2N^2N_o$  eigenvalues, which very often turns out to be insufficient for obtaining a smooth LDOS spectrum. In such a scenario, the supercell method is widely used to increase the spectral resolution without increasing the number of lattice sites. In this method, first, the BdG equations on  $N \times N$  lattice are self-consistently solved, then the  $N \times N$  lattice is pictured as a 'supercell', a big unit cell with  $N^2N_o$  orbitals, which is repeated  $M \times M$  times to make a larger lattice. Then periodic boundary conditions are imposed on this system. Thus, the system now becomes translationally invariant and can be described in momentum space with the following supercell BdG equation (written in matrix form to avoid the cluttering of symbols):

$$\begin{pmatrix} H_0(\mathbf{K}) & -\Delta(\mathbf{K}) \\ -\Delta^\dagger(\mathbf{K}) & -H_0(\mathbf{K}) \end{pmatrix} \begin{pmatrix} U_\uparrow^n(\mathbf{K}) \\ V_\downarrow^n(\mathbf{K}) \end{pmatrix} = E_{n\uparrow}(\mathbf{K}) \begin{pmatrix} U_\uparrow^n(\mathbf{K}) \\ V_\downarrow^n(\mathbf{K}) \end{pmatrix}, \quad (\text{B-1})$$

$$H_0(\mathbf{K}) = \sum_I T_{I,0} e^{i\mathbf{K} \cdot \mathbf{R}_I}, \quad (\text{B-2})$$

$$\Delta(\mathbf{K}) = \sum_I \Delta_{I,0} e^{i\mathbf{K} \cdot \mathbf{R}_I}. \quad (\text{B-3})$$

Here,  $T_{I,0}$  and  $\Delta_{I,0}$  are the  $N^2N_o \times N^2N_o$  hopping and superconducting gap matrix between the supercell at origin and supercell with lattice vector  $\mathbf{R}_I$ ,  $\mathbf{K}$  is the supercell momentum vector with components  $K_x, K_y = \frac{n}{M}, m = 0, 1, 2, \dots, M - 1$  (in units of  $\frac{2\pi}{Na_0}$ ),  $U_\uparrow^n(\mathbf{K})$  and  $V_\downarrow^n(\mathbf{K})$  are column vectors with  $N^2N_o$  elements  $u_{i\mu\uparrow}^n$  and  $v_{i\mu\downarrow}^n$ , respectively, where  $i = 1, 2, \dots, N^2$  and  $\mu = 1, 2, \dots, N_o$ .

$T_{I,0}$  and  $\Delta_{I,0}$  can be found from the hopping elements  $t_{i_0}^{\mu\nu}$  (for the original unit cell), and the chemical potential  $\mu$  and the gap field obtained from the self-consistent solution of lattice BdG equations (Equation 2-9) as shown schematically in the Figure B-1. Clearly, there are only nine supercells from which hopping to the central cell is possible. These

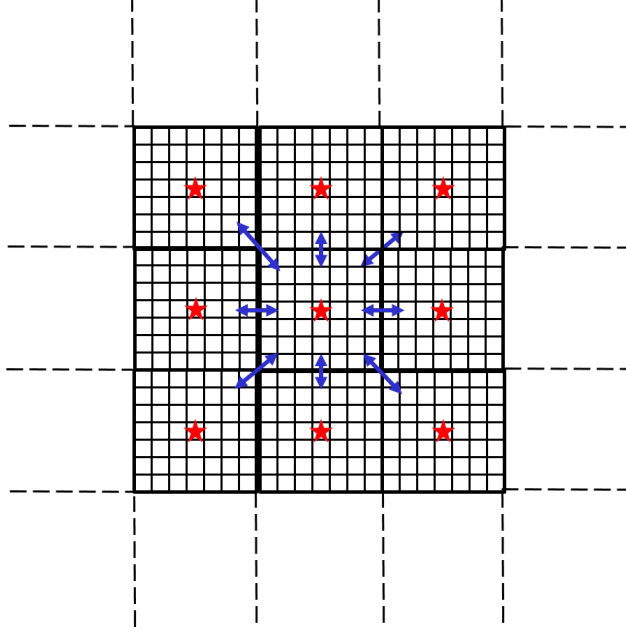


Figure B-1. Schematic of the supercell set-up. The supercell is schematically represented by bigger squares containing  $N \times N$  unit cells (here  $N = 7$ ) denoted by smaller squares. An impurity at the center of supercell is represented by a red star. This supercell is repeated  $M \times M$  times as indicated by the dotted lines. After periodic boundary conditions are imposed, the system can be described by hopping and superconducting gap field matrices between the central cell and 8 neighboring supercells as discussed in the text.

include the on-site, four nearest neighbor (NN), and for next nearest neighbor (NNN) supercells. The on-site matrices  $T_{0,0}$  and  $\Delta_{0,0}$  have elements same elements  $\xi_{ij\sigma}^{\mu\nu}$  and  $\Delta_{ij\sigma}^{\mu\nu}$  as in Equation 2-9 with one difference that the periodic boundary conditions are not imposed while finding the elements. The other supercell matrices  $T_{I,0}$  and  $\Delta_{I,0}$  can be obtained in a similar way by considering the hopping and gap field between orbitals in the central and neighboring (NN and NNN) supercells. The non-vanishing matrix elements will only occur for the orbitals around the edges of the central supercells and they are schematically indicated by double-headed arrows in the Figure B-1. Note that for  $\mathbf{K} = \mathbf{0}$ , the supercell BdG equations (Equation B-1) reduce to the lattice BdG equations (Equation 2-9).

With supercell hopping and gap field matrices in hand, the supercell BdG equation (Equation B-1) is solved for each  $\mathbf{K}$ . Note that for  $\mathbf{K} = \mathbf{0}$ , the supercell BdG equations

reduce to the lattice BdG equations (Equation 2-9). Using the eigenvalues  $E_n(\mathbf{K})$  and eigenvectors  $U_{\uparrow}^n(\mathbf{K})$  and  $V_{\uparrow}^n(\mathbf{K})$  the lattice Greens function matrix is calculated via following equations

$$\begin{aligned}
 G_{ij\uparrow}^{\mu\nu}(\omega) &= \frac{1}{M^2} \sum_{n,\mathbf{K}} \frac{u_{i\mu\uparrow}^n(\mathbf{K})u_{j\nu\uparrow}^{n*}(\mathbf{K})}{\omega - E_{n\uparrow}(\mathbf{K}) + i0^+}, \\
 G_{ij\downarrow}^{\mu\nu}(\omega) &= \frac{1}{M^2} \sum_{n,\mathbf{K}} \frac{v_{i\mu\downarrow}^{n*}(\mathbf{K})v_{j\nu\downarrow}^n(\mathbf{K})}{\omega + E_{n\uparrow}(\mathbf{K}) + i0^+}.
 \end{aligned}
 \tag{B-4}$$

Comparing with Equation 2-12, we can see that with supercell method  $M^2 - 1$  additional eigenvalues are obtained which helps to increase the spectral resolution leading to a smooth lattice and continuum LDOS spectrum.

APPENDIX C  
ANALYTICAL PROOF OF U-SHAPED CONTINUUM LDOS IN  
SUPERCONDUCTING BSCCO

In this appendix, we show that the continuum LDOS for BSCCO above a Cu site, at height several Å above the BiO plane where the STM tip is typically placed, at low energies varies as  $\rho(\mathbf{r}, \omega \rightarrow 0) \sim |\omega|^3$  yielding a U-shape in the spectrum. We work in units where  $\hbar = 1$ .

In a translationally invariant system, the lattice Greens function  $G_{ij\sigma}$  can be represented as

$$G_{ij\sigma}(\omega) = \sum_{\mathbf{k}} G_{\sigma}(\mathbf{k}, \omega) e^{i\mathbf{k} \cdot (\mathbf{R}_i - \mathbf{R}_j)}. \quad (\text{C-1})$$

Here, we have considered a 1-band system, and, hence, the orbital indices are suppressed. Using Equations C-1 and 2-18 we obtain

$$G_{\sigma}(\mathbf{r}, \omega) = \sum_{\mathbf{k}} G_{\sigma}(\mathbf{k}, \omega) |W_{\mathbf{k}}(\mathbf{r})|^2, \quad (\text{C-2})$$

where

$$W_{\mathbf{k}}(\mathbf{r}) = \sum_i w_i(\mathbf{r}) e^{i\mathbf{k} \cdot \mathbf{R}_i}. \quad (\text{C-3})$$

Here,  $w_i(\mathbf{r})$  is the Wannier function centered at the lattice vector  $\mathbf{R}_i$ , and  $W_{\mathbf{k}}(\mathbf{r})$  can be called as the  $\mathbf{k}$ -space Wannier function.

Now, using Equations 2-14 and C-2, we can write continuum LDOS  $\rho_{\sigma}(\mathbf{r}, \omega)$  as

$$\rho_{\sigma}(\mathbf{r}, \omega) = \sum_{\mathbf{k}} A_{\sigma}(\mathbf{k}, \omega) |W_{\mathbf{k}}(\mathbf{r})|^2, \quad (\text{C-4})$$

where the  $\mathbf{k}$ -space spectral function  $A_{\sigma}(\mathbf{k}, \omega)$  can be expressed as

$$\begin{aligned} A_{\sigma}(\mathbf{k}, \omega) &= -\frac{1}{\pi} \text{Im}[G_{\sigma}(\mathbf{k}, \omega)] \\ &= -\frac{1}{\pi} \text{Im} \left[ \frac{|u_{\mathbf{k}}|^2}{\omega - E_{\mathbf{k}} + i0^+} + \frac{|v_{\mathbf{k}}|^2}{\omega + E_{\mathbf{k}} + i0^+} \right] \\ &= |u_{\mathbf{k}}|^2 \delta(\omega - E_{\mathbf{k}}) + |v_{\mathbf{k}}|^2 \delta(\omega + E_{\mathbf{k}}). \end{aligned} \quad (\text{C-5})$$

Here,  $\delta$  is the Dirac delta function. The coherence factors  $u_{\mathbf{k}}$  and  $v_{\mathbf{k}}$ , and the quasiparticle energy in the superconducting state  $E_{\mathbf{k}}$  are given by following expressions

$$|u_{\mathbf{k}}|^2 = \frac{1}{2} \left( 1 + \frac{\xi_{\mathbf{k}}}{E_{\mathbf{k}}} \right) = 1 - |v_{\mathbf{k}}|^2, \quad (\text{C-6})$$

$$E_{\mathbf{k}} = \sqrt{\xi_{\mathbf{k}}^2 + \Delta_{\mathbf{k}}^2}. \quad (\text{C-7})$$

Here,  $\xi_{\mathbf{k}}$  is the band energy relative to the Fermi energy. For cuprates, the  $d$ -wave superconducting gap order parameter  $\Delta_{\mathbf{k}}$  can be expressed as

$$\Delta_{\mathbf{k}} = \Delta_0(\cos k_x - \cos k_y). \quad (\text{C-8})$$

Using Equations C-4, C-5, and C-6, we can write

$$\rho_{\sigma}(\mathbf{r}, \omega) = \frac{1}{2} \sum_{\mathbf{k}} \left( 1 + \frac{\xi_{\mathbf{k}}}{E_{\mathbf{k}}} \right) |W_{\mathbf{k}}(\mathbf{r})|^2 \delta(\omega - E_{\mathbf{k}}). \quad (\text{C-9})$$

In following paragraphs, we will derive expression for continuum LDOS as  $\omega \rightarrow 0$  only for positive energies. The results can be easily extended to the negative energies using particle-hole symmetry.

For the continuum position above the Cu site,  $\mathbf{r}_0 = [0, 0, z]$ , at heights  $z$  several Å above the BiO plane, the dominant contribution to the sum in the right hand side of the Equation C-3 comes from the the Wannier function at the nearest neighbor sites; it can be easily inferred from the Wannier function cut at the height  $z \approx 5$  Å shown in the Figure 4-4. Thus, the  $\mathbf{k}$ -space Wannier function at such positions can be approximated as:

$$W_{\mathbf{k}}(\mathbf{r}_0) \approx w_0 + 2w_1(\cos k_x - \cos k_y) \quad (\text{C-10})$$

where,  $w_0$  and  $w_1$  are the values of the Wannier function at  $\mathbf{r} = \mathbf{r}_0$ , and  $\mathbf{r} = \mathbf{r}_0 + a_0 \hat{x}$ , where  $a_0$  is the in-plane lattice vector. The  $d_{x^2-y^2}$ -wave symmetry of the Wannier function dictates that  $w_0 = 0$ , however, we still keep it to facilitate discussions presented latter in this appendix. Also, the same symmetry assures that the all higher order terms, which might arise in Equation C-10 from the contributions of the other neighbors, must have

the  $d_{x^2-y^2}$ -wave symmetry. For example, contributions from NNN sites would be zero, and that from 3rd nearest neighbors would be  $w_3(\cos 2k_x - \cos 2k_y)$ . All such higher order terms will not qualitatively change our final conclusions regarding the shape of the continuum LDOS spectrum at low energies.

Using Equations C-9 and C-10, we can express the continuum LDOS above the Cu site as

$$\begin{aligned}
\rho_\sigma(\mathbf{r}_0, \omega) &= \rho^{00} + \rho^{10} + \rho^{11} \\
\rho^{00} &= \frac{1}{2}w_0^2 \sum_{\mathbf{k}} \left(1 + \frac{\xi_{\mathbf{k}}}{E_{\mathbf{k}}}\right) \delta(\omega - E_{\mathbf{k}}) \\
\rho^{10} &= 2w_0w_1 \sum_{\mathbf{k}} \left(1 + \frac{\xi_{\mathbf{k}}}{E_{\mathbf{k}}}\right) (\cos k_x - \cos k_y) \delta(\omega - E_{\mathbf{k}}) \\
\rho^{11} &= 2w_1^2 \sum_{\mathbf{k}} \left(1 + \frac{\xi_{\mathbf{k}}}{E_{\mathbf{k}}}\right) (\cos k_x - \cos k_y)^2 \delta(\omega - E_{\mathbf{k}}).
\end{aligned} \tag{C-11}$$

At low energies the momentum space integrals will have dominant contributions from the nodal regions of the Brillouin zone. Accordingly, we can expand  $\xi_{\mathbf{k}}$  and  $\Delta_{\mathbf{k}}$  around the nodal point  $\mathbf{k}_0 = [k_x^0, k_y^0]$ , with  $k_x^0 = k_y^0 = \frac{1}{\sqrt{2}}k_0$ , and shift the  $k$ -space origin to the same to facilitate the computation of integral. The new coordinate axes  $k_1$  and  $k_2$ , given by following transformations, are shown in the Figure C-1.

$$\begin{aligned}
k_1 &= \frac{1}{\sqrt{2}}(k_y - k_x) \\
k_2 &= \frac{1}{\sqrt{2}}(k_y + k_x) + k_0.
\end{aligned} \tag{C-12}$$

Linearizing the spectrum around the nodal point yields

$$\xi_{\mathbf{k}} = v_F k_2 + O(k^2), \tag{C-13}$$

where  $v_F$  is the Fermi velocity at the node. Note that for a NN tight-binding model  $v_F = -2\sqrt{2}t \sin k_x^0$ . We can also linearize the gap function by expanding around the node as

$$\begin{aligned}
\Delta_{\mathbf{k}} &= v_\Delta k_1 + O(k^2), \\
v_\Delta &= \sqrt{2}\Delta_0 \sin k_x^0.
\end{aligned} \tag{C-14}$$

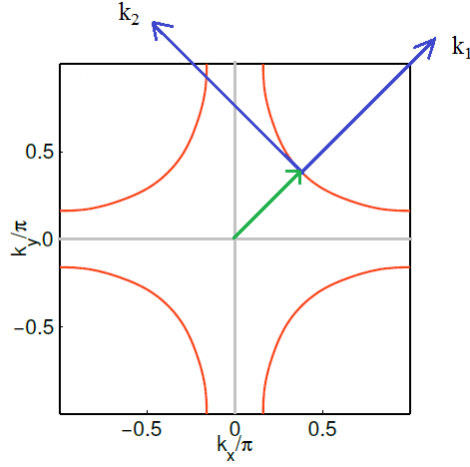


Figure C-1. Coordinate system  $(k_1, k_2)$  with axes parallel and perpendicular to a nodal direction and origin located at a node  $\mathbf{k}_0$  denoted by the green arrow.

From Equations C-8, C-13, and C-14, we have

$$E_{\mathbf{k}} = \sqrt{v_{\Delta}^2 k_1^2 + v_F^2 k_2^2}. \quad (\text{C-15})$$

Now, using Equations C-11 and C-13, and converting the sum over  $\mathbf{k}$  in former to an integral

$$\rho^{00} = \frac{1}{2} M w_0^2 \iint_{\Omega} \frac{d\mathbf{k}}{(2\pi)^2} \left(1 + \frac{v_F k_2}{\sqrt{v_{\Delta}^2 k_1^2 + v_F^2 k_2^2}}\right) \delta(\omega - \sqrt{v_{\Delta}^2 k_1^2 + v_F^2 k_2^2}), \quad (\text{C-16})$$

where  $\Omega$  is a circular region of radius  $\Gamma$  around the nodal point  $\mathbf{k}_0$ , and  $M = 4$  is the number of nodes. The above integral can be simplified by scaling the coordinates as  $k'_1 = v_{\Delta} k_1$  and  $k'_2 = v_F k_2$ , followed by a transformation to the polar coordinates with  $k'_1 = k' \cos \theta'$  and  $k'_2 = k' \sin \theta'$ . Following is the resulting expression.

$$\begin{aligned} \rho^{00} &= \frac{1}{2} M w_0^2 \frac{1}{v_F v_{\Delta}} \frac{1}{(2\pi)^2} \left[ \int_0^{\Gamma} \int_0^{2\pi} k' dk' d\theta' \delta(\omega - k') + \int_0^{\Gamma} \int_0^{2\pi} k' dk' d\theta' \delta(\omega - k') \sin \theta' \right] \\ &= \frac{1}{2} M w_0^2 \frac{1}{v_F v_{\Delta}} \frac{1}{(2\pi)^2} [2\pi\omega + 0]. \end{aligned} \quad (\text{C-17})$$

Hence,

$$\rho^{00} = \left( \frac{w_0^2}{\pi v_F v_{\Delta}} \right) \omega. \quad (\text{C-18})$$

Note that setting the Wannier function factor to 1 in Equation C-4 yields the lattice LDOS  $N(\omega) = \sum_{\mathbf{k}} A_{\mathbf{k}}(\omega)$ , suggesting that we can simply obtain the expression for lattice LDOS as  $\omega \rightarrow 0$  by setting  $w_0 = 1$  and  $w_1 = 0$ . Hence, using Equation C-18 with  $w_0 = 1$ , we get the lattice LDOS at low (positive) energies as

$$N(\omega) = \left( \frac{1}{\pi v_F v_{\Delta}} \right) \omega. \quad (\text{C-19})$$

Which shows that as  $\omega \rightarrow 0$  lattice LDOS varies linearly yielding a V-shape. However, in case of the continuum LDOS  $w_0 = 0$ , as explained earlier, thus, this linear term does not contribute to the low energy DOS. In following we show that the  $\rho^{10}$  vanishes and  $\rho^{11}$  yields a  $\omega^3$  variation, thus, yielding a U-shape.

Using Equations C-11, C-13, C-14, and C-15, we get

$$\rho^{10} = 2w_0 w_1 M \iint_{\Omega} \frac{d\mathbf{k}}{(2\pi)^2} \left( 1 + \frac{v_F k_2}{\sqrt{v_{\Delta}^2 k_1^2 + v_F^2 k_2^2}} \right) (2\sqrt{2}t \sin k_x^0 k_1) \delta(\omega - \sqrt{v_{\Delta}^2 k_1^2 + v_F^2 k_2^2}). \quad (\text{C-20})$$

Rescaling the coordinates, followed by a transformation to polar coordinates in above integral yields angular integrals of  $\cos \theta'$  and  $\cos \theta' \sin \theta'$  over  $\theta = [0, 2\pi]$ . These angular integrals vanish resulting into

$$\rho^{10} = 0. \quad (\text{C-21})$$

Finally, we evaluate  $\rho^{11}$  using Equations C-11, C-13, C-14, and C-15.

$$\rho^{11} = 2w_1^2 M \iint_{\Omega} \frac{d\mathbf{k}}{(2\pi)^2} \left( 1 + \frac{v_F k_2}{\sqrt{v_{\Delta}^2 k_1^2 + v_F^2 k_2^2}} \right) (2\sqrt{2}t \sin k_x^0 k_1)^2 \delta(\omega - \sqrt{v_{\Delta}^2 k_1^2 + v_F^2 k_2^2}). \quad (\text{C-22})$$

Rescaling the coordinates, followed by a transformation to polar coordinates in above integral yields

$$\begin{aligned} \rho^{11} &= \frac{4M w_1^2 \sin^2 k_x^0}{(2\pi)^2 v_F v_{\Delta}^3} \left[ \int_0^{\Gamma} \int_0^{2\pi} k' dk' d\theta' \delta(\omega - k') (k'^2 \cos^2 \theta' + \sin \theta' \cos^2 \theta') \right] \\ &= \frac{4M w_1^2 \sin^2 k_x^0}{(2\pi)^2 v_F v_{\Delta}^3} \left[ \omega^3 \frac{1}{\pi} + 0 \right]. \end{aligned} \quad (\text{C-23})$$

Hence,

$$\rho^{11} = \left( \frac{4w_1^2 \sin^2 k_x^0}{\pi^3 v_F v_\Delta^3} \right) \omega^3. \quad (\text{C-24})$$

Combining Equations C-11, C-18, C-21, and C-24, we get the expression for low energy continuum LDOS as

$$\begin{aligned} \rho_\sigma(\mathbf{r}_0, \omega) &= a_0 \omega + a_1 \omega^3, \\ a_0 &= \frac{w_0^2}{\pi v_F v_\Delta}, \quad a_1 = \frac{4w_1^2 \sin^2 k_x^0}{\pi^3 v_F v_\Delta^3}. \end{aligned} \quad (\text{C-25})$$

The coefficient of the linear in  $\omega$  term vanishes as  $w_0 = 0$  due to  $d_{x^2-y^2}$  symmetry of the Wannier function. However, the cubic in  $\omega$  term is non-zero, and yields a U-shaped spectrum.

APPENDIX D  
MICROSCOPIC JUSTIFICATION OF THE "FILTER" THEORY

To explain the spatial pattern of the Zn impurity-induced resonance states in BSCCO [60] (see Section 1.5), Martin et al. [62] proposed a phenomenological "filter" wavefunction resulting from the non-trivial tunneling path provided by the BiO layer. The authors argued that the direct tunneling between the STM tip and the  $3d_{x^2-y^2}$  orbital of the Cu atom underneath is prohibited due to its vanishing overlap with axial orbitals (Bi- $6p_z$  and apical O- $2p_z$ ) in BiO plane. Instead, they proposed, an indirect tunneling occurs through the Cu- $4s$  (or Cu- $3d_{z^2}$ ) orbital which overlaps with the nearest-neighbor Cu- $3d_{x^2-y^2}$  orbital, resulting in the tunneling intensity on the lattice site  $i = (i_x, i_y)$ , expressed in terms of the impurity state wavefunction  $\Psi_{i_x, i_y}$ ,

$$A_{i_x, i_y}^{\text{BiO}} \propto |\Psi_{i_x+1, i_y} + \Psi_{i_x-1, i_y} - \Psi_{i_x, i_y+1} - \Psi_{i_x, i_y-1}|^2, \quad (\text{D-1})$$

which is very different from the tunneling intensity  $A_{i_x, i_y}^{\text{CuO}} \propto |\Psi_{i_x, i_y}|^2$  obtained by assuming a direct tunneling. Here, we show that the BdG+W scheme provides a microscopic justification for the aforementioned "filter" argument.

Setting orbital indices  $\mu, \nu = 1$  in Equation 2-11 the lattice Greens function matrix for the 1-band BSCCO can be written as

$$G_{ij\sigma}(\omega) = \sum_{n>0} \left[ \frac{u_{i\sigma}^n u_{j\sigma}^{n*}}{\omega - E_{n\sigma} + i0^+} + \frac{v_{i\sigma}^{n*} v_{j\sigma}^n}{\omega + E_{n\bar{\sigma}} + i0^+} \right]. \quad (\text{D-2})$$

The continuum Greens function, in case of one orbital per site, will be given by Equation 2-18

$$\begin{aligned} G_{\sigma}(\mathbf{r}, \omega) &= \sum_{ij} G_{ij\sigma}(\omega) w_i(\mathbf{r}) w_j^*(\mathbf{r}) \\ &= \sum_{n>0} \left[ \frac{(\sum_i u_{i\sigma}^n w_i(\mathbf{r})) (\sum_j u_{j\sigma}^n w_j(\mathbf{r}))^*}{\omega - E_{n\sigma} + i0^+} + \frac{(\sum_i v_{i\sigma}^n w_i(\mathbf{r}))^* (\sum_j v_{j\sigma}^n w_j(\mathbf{r}))}{\omega + E_{n\bar{\sigma}} + i0^+} \right] \\ &= \sum_{n>0} \left[ \frac{|u_{\sigma}^n(\mathbf{r})|^2}{\omega - E_{n\sigma} + i0^+} + \frac{|v_{\sigma}^n(\mathbf{r})|^2}{\omega + E_{n\bar{\sigma}} + i0^+} \right], \end{aligned} \quad (\text{D-3})$$

where  $u_\sigma^n(\mathbf{r}) = \sum_i u_{i\sigma}^n w_i(\mathbf{r})$  and  $v_\sigma^n(\mathbf{r}) = \sum_i v_{i\sigma}^n w_i(\mathbf{r})$ . As evident from Figure 4-4, at a continuum point  $\mathbf{r} = \mathbf{r}_0$  directly above the impurity site  $i^*$  located at a height a few Å above the BiO plane, the on-site Wannier function is zero, whereas the NN Wannier functions have the largest magnitude. Thus, ignoring small contributions from the Wannier functions located at distant sites, we can write

$$\begin{aligned} u_\sigma^n(\mathbf{r}_0) &\approx w_1 [u_{i^*+\hat{x},\sigma}^n + u_{i^*-\hat{x},\sigma}^n - u_{i^*+\hat{y},\sigma}^n - u_{i^*-\hat{y},\sigma}^n], \\ v_\sigma^n(\mathbf{r}_0) &\approx w_1 [v_{i^*+\hat{x},\sigma}^n + v_{i^*-\hat{x},\sigma}^n - v_{i^*+\hat{y},\sigma}^n - v_{i^*-\hat{y},\sigma}^n], \end{aligned} \quad (\text{D-4})$$

where  $w_1$  is the magnitude of the Wannier function at the NN site, and we have properly accounted for the sign change of the Wannier function with  $90^\circ$  rotation in the above expression. Equation D-4 is equivalent to the "filter" wavefunction proposed in [62] but it now has a precise definition and microscopic justification. Now, using Equations D-3 and D-4, the continuum LDOS at  $\mathbf{r} = \mathbf{r}_0$  is

$$\begin{aligned} \rho_\sigma(\mathbf{r}_0, \omega) &= -\frac{1}{\pi} \text{Im} [G_\sigma(\mathbf{r}_0, \omega)] \\ &= |w_1|^2 \sum_{\tau=\pm\hat{x},\pm\hat{y}} -\frac{1}{\pi} \text{Im} \left[ \sum_{n>0} \frac{|u_{i^*+\tau,\sigma}^n|^2}{\omega - E_{n\sigma} + i0^+} + \frac{|v_{i^*+\tau,\sigma}^n|^2}{\omega + E_{n\bar{\sigma}} + i0^+} \right] + \text{interference terms} \\ &= |w_1|^2 \sum_{\tau=\pm\hat{x},\pm\hat{y}} N_{i^*+\tau,\sigma}(\omega) + \text{interference terms}, \end{aligned} \quad (\text{D-5})$$

where we have used the definition of lattice LDOS  $N_{i\sigma}(\omega)$  as stated in Equation 2-13, in conjunction with Equation D-2.

Equation D-5 shows that the continuum LDOS above the impurity site at a height few Å above the BiO plane is equal to the sum of the lattice LDOS at the NN sites and interference terms. Since, lattice LDOS above the NN sites have large magnitude at the resonance energy ( $\Omega = -3.6$  meV) (see Figure 4-5(a)) and the sign of interference terms is not fixed, Equation D-5 implies that the continuum LDOS directly above the impurity site must have a large magnitude at the same energy, which is indeed the case (see Figure 4-5(b)). However, We note that the interference terms are important to account for the full bias dependence of the continuum LDOS. For example, simply adding NN lattice

LDOS suggests that there should be an observable weight at  $\omega = +3.6$  meV; however, the continuum LDOS plotted in Figure 4-5(b) shows no such feature.

## REFERENCES

- [1] H. Kamerlingh Onnes, *Comm. Phys. Lab. Univ. Leiden* **29**, 1 (1911).
- [2] W. Meissner and R. Ochsenfeld, *Naturwissenschaften* **21**, 787 (1933).
- [3] F. London and H. London, *Proc. Roy. Soc. (London) A* **149**, 71 (1935).
- [4] V. L. Ginzburg and L. D. Landau, *Soviet Phys. JETP* **20**, 1064 (1950).
- [5] E. Maxwell, *Phys. Rev.* **78**, 477 (1950).
- [6] C. A. Reynolds, B. Serin, W. H. Wright, and L. B. Nesbitt, *Phys. Rev.* **78**, 487 (1950).
- [7] J. Bardeen, *Phys. Rev.* **79**, 167 (1950).
- [8] H. Fröhlich, *Phys. Rev.* **79**, 845 (1950).
- [9] J. Bardeen and D. Pines, *Phys. Rev.* **99**, 1140 (1955).
- [10] L. N. Cooper, *Phys. Rev.* **104**, 1189 (1956).
- [11] J. Bardeen, L. N. Cooper, and J. R. Schrieffer, *Phys. Rev.* **106**, 162 (1957).
- [12] J. G. Bednorz and K. A. Müller, *Z. Phys. B* **64**, 189 (1986).
- [13] Y. Kamihara, T. Watanabe, M. Hirano, and H. Hosono, *J. Am. Chem. Soc.* **130**, 3296 (2008).
- [14] X. Chen, T. Wu, G. Wu, R. Liu, H. Chen, and D. Fang, *Nature* **453**, 761 (2008).
- [15] W. Qing-Yan, L. Zhi, Z. Wen-Hao, Z. Zuo-Cheng, Z. Jin-Song, L. Wei, D. Hao, O. Yun-Bo, D. Peng, C. Kai, W. Jing, S. Can-Li, H. Ke, J. Jin-Feng, J. Shuai-Hua, W. Ya-Yu, W. Li-Li, C. Xi, M. Xu-Cun, and X. Qi-Kun, *Chin. Phys. Lett.* **29**, 037402 (2012).
- [16] B. Keimer, S. Kivelson, M. Norman, S. Uchida, and J. Zaanen, *Nature* **518**, 179 (2015).
- [17] J. R. Schrieffer, *Theory of superconductivity* (Pennsylvania Univ., Philadelphia, PA, 1963).
- [18] M. Tinkham, *Introduction to Superconductivity; 2nd ed.*, Dover books on physics (Dover, Mineola, NY, 2004).
- [19] J. B. Ketterson and S. S. Nian, *Superconductivity* (Cambridge Univ. Press, Cambridge, 1999).

- [20] R. Meservey and B. Schwartz, “Equilibrium properties: comparison of experimental results with predictions of the BCS theory.” in *Superconductivity*, edited by R. D. Parks (Marcel Dekker Inc., New York, 1969) pp. 117–191.
- [21] D. M. Ginsberg and L. C. Hebel, “Nonequilibrium properties: comparison of experimental results with predictions of the BCS theory.” in *Superconductivity*, edited by R. D. Parks (Marcel Dekker Inc., New York, 1969) pp. 193–247.
- [22] J. Orenstein and A. J. Millis, [Science](#) **288**, 468 (2000).
- [23] P. W. Anderson, [Phys. Rev.](#) **79**, 350 (1950).
- [24] P. A. Lee, N. Nagaosa, and X.-G. Wen, [Rev. Mod. Phys.](#) **78**, 17 (2006).
- [25] D. J. Van Harlingen, [Rev. Mod. Phys.](#) **67**, 515 (1995).
- [26] C. C. Tsuei and J. R. Kirtley, [Rev. Mod. Phys.](#) **72**, 969 (2000).
- [27] A. Damascelli, Z. Hussain, and Z.-X. Shen, [Rev. Mod. Phys.](#) **75**, 473 (2003).
- [28] M. Sigrist and K. Ueda, [Rev. Mod. Phys.](#) **63**, 239 (1991).
- [29] M. Ogata and H. Fukuyama, [Rep. Prog. Phys.](#) **71**, 036501 (2008).
- [30] F. C. Zhang, C. Gros, T. M. Rice, and H. Shiba, [Supercond. Sci. Technol.](#) **1**, 36 (1988).
- [31] G. Baskaran, Z. Zou, and P. Anderson, [Solid State Commun.](#) **63**, 973 (1987).
- [32] A. E. Ruckenstein, P. J. Hirschfeld, and J. Appel, [Phys. Rev. B](#) **36**, 857 (1987).
- [33] G. Kotliar, [Phys. Rev. B](#) **37**, 3664 (1988).
- [34] T. Wu, H. Mayaffre, S. Krämer, M. Horvatić, C. Berthier, W. Hardy, R. Liang, D. Bonn, and M.-H. Julien, [Nature](#) **477**, 191 (2011).
- [35] Y. Kohsaka, C. Taylor, K. Fujita, A. Schmidt, C. Lupien, T. Hanaguri, M. Azuma, M. Takano, H. Eisaki, H. Takagi, S. Uchida, and J. C. Davis, [Science](#) **315**, 1380 (2007).
- [36] R. Comin and A. Damascelli, [Annu. Rev. Condens. Matter Phys.](#) **7**, 369 (2016).
- [37] J. M. Tranquada, [AIP Conf. Proc.](#) **1550**, 114 (2013).
- [38] T. Timusk and B. Statt, [Rep. Prog. Phys.](#) **62**, 61 (1999).
- [39] J. Paglione and R. L. Greene, [Nat Phys](#) **6**, 645 (2010).
- [40] A. Chubukov and P. J. Hirschfeld, [Physics today](#) **68**, 46 (2015).
- [41] D. Huang and J. E. Hoffman, [Annu. Rev. Condens. Matter Phys.](#) **8** (2017).

- [42] J.-F. Ge, Z.-L. Liu, C. Liu, C.-L. Gao, D. Qian, Q.-K. Xue, Y. Liu, and J.-F. Jia, *Nat. Mater.* **14**, 285 (2015).
- [43] S. He, J. He, W. Zhang, L. Zhao, D. Liu, X. Liu, D. Mou, Y.-B. Ou, Q.-Y. Wang, Z. Li, L. Wang, Y. Peng, Y. Liu, C. Chen, L. Yu, G. Liu, X. Dong, J. Zhang, C. Chen, Z. Xu, X. Chen, X. Ma, Q. Xue, and X. J. Zhou, *Nat. Mater.* **12**, 605 (2013).
- [44] W. Ku, T. Berlijn, L. Wang, and C.-C. Lee, “First-principles studies in fe-based superconductors,” in *Iron-Based Superconductivity*, edited by P. D. Johnson, G. Xu, and W.-G. Yin (Springer International Publishing, Cham, 2015) pp. 223–253.
- [45] Y. Zhang, Z. R. Ye, and D. L. Feng, “Electron spectroscopy: Arpes,” in *Iron-Based Superconductivity*, edited by P. D. Johnson, G. Xu, and W.-G. Yin (Springer International Publishing, Cham, 2015) pp. 115–149.
- [46] P. Dai, *Rev. Mod. Phys.* **87**, 855 (2015).
- [47] R. M. Fernandes, A. V. Chubukov, and J. Schmalian, *Nat. Phys.* **10**, 97 (2014).
- [48] J.-H. Chu, J. G. Analytis, K. De Greve, P. L. McMahon, Z. Islam, Y. Yamamoto, and I. R. Fisher, *Science* **329**, 824 (2010).
- [49] E. P. Rosenthal, E. F. Andrade, C. J. Arguello, R. M. Fernandes, L. Y. Xing, X. C. Wang, C. Q. Jin, A. J. Millis, and A. N. Pasupathy, *Nat. Phys.* **10**, 225 (2014).
- [50] M. Yi, D. Lu, J.-H. Chu, J. G. Analytis, A. P. Sorini, A. F. Kemper, B. Moritz, S.-K. Mo, R. G. Moore, M. Hashimoto, W.-S. Lee, Z. Hussain, T. P. Devereaux, I. R. Fisher, and Z.-X. Shen, *Proc. Natl. Acad. Sci. U.S.A.* **108**, 6878 (2011).
- [51] S. Kasahara, H. Shi, K. Hashimoto, S. Tonegawa, Y. Mizukami, T. Shibauchi, K. Sugimoto, T. Fukuda, T. Terashima, A. H. Nevidomskyy, *et al.*, *Nature* **486**, 382 (2012).
- [52] H.-H. Wen and S. Li, *Annu. Rev. Condens. Matter Phys.* **2**, 121 (2011).
- [53] M. Long and Y. Wei-Qiang, *Chin. Phys. B* **22**, 087414 (2013).
- [54] S. Onari and H. Kontani, “Orbital+spin multimode fluctuation theory in iron-based superconductors,” in *Iron-Based Superconductivity*, edited by P. D. Johnson, G. Xu, and W.-G. Yin (Springer International Publishing, Cham, 2015) pp. 331–376.
- [55] A. Chubukov, “Itinerant electron scenario,” in *Iron-Based Superconductivity*, edited by P. D. Johnson, G. Xu, and W.-G. Yin (Springer International Publishing, Cham, 2015) pp. 255–329.
- [56] J. E. Hoffman, *Rep. Prog. Phys.* **74**, 124513 (2011).
- [57] O. Fischer, M. Kugler, I. Maggio-Aprile, C. Berthod, and C. Renner, *Rev. Mod. Phys.* **79**, 353 (2007).

- [58] K. Fujita, A. R. Schmidt, E.-A. Kim, M. J. Lawler, D. H. Lee, J. Davis, H. Eisaki, and S. ichi Uchida, *J. Phys. Soc. Jpn.* **81**, 011005 (2012).
- [59] A. Yazdani, E. H. da Silva Neto, and P. Aynajian, *Annu. Rev. Condens. Matter Phys.* **7**, 11 (2016).
- [60] S. Pan, E. Hudson, K. Lang, H. Eisaki, S. Uchida, and J. Davis, *Nature* **403**, 746 (2000).
- [61] A. V. Balatsky, M. I. Salkola, and A. Rosengren, *Phys. Rev. B* **51**, 15547 (1995).
- [62] I. Martin, A. V. Balatsky, and J. Zaanen, *Phys. Rev. Lett.* **88**, 097003 (2002).
- [63] C.-L. Song, Y.-L. Wang, Y.-P. Jiang, L. Wang, K. He, X. Chen, J. E. Hoffman, X.-C. Ma, and Q.-K. Xue, *Phys. Rev. Lett.* **109**, 137004 (2012).
- [64] E. Hudson, K. Lang, V. Madhavan, S. Pan, H. Eisaki, S. Uchida, and J. Davis, *Nature* **411**, 920 (2001).
- [65] K. Fujita, M. H. Hamidian, S. D. Edkins, C. K. Kim, Y. Kohsaka, M. Azuma, M. Takano, H. Takagi, H. Eisaki, S.-i. Uchida, A. Allais, M. J. Lawler, E.-A. Kim, S. Sachdev, and J. C. S. Davis, *Proc. Natl. Acad. Sci. U.S.A.* **111**, E3026 (2014).
- [66] M. Hamidian, S. Edkins, C. K. Kim, J. Davis, A. Mackenzie, H. Eisaki, S. Uchida, M. Lawler, E.-A. Kim, S. Sachdev, *et al.*, *Nat. Phys.* **16**, 150 (2015).
- [67] P. Choubey, T. Berlijn, A. Kreisel, C. Cao, and P. J. Hirschfeld, *Phys. Rev. B* **90**, 134520 (2014).
- [68] H. Alloul, J. Bobroff, M. Gabay, and P. J. Hirschfeld, *Rev. Mod. Phys.* **81**, 45 (2009).
- [69] P. Anderson, *J. Phys. Chem. Solids* **11**, 26 (1959).
- [70] A. A. Abrikosov and L. P. Gor'kov, *Sov. Phys. JETP* **12**, 1243 (1961).
- [71] Y. Luh, *Acta Phys. Sin.* **21**, 75 (1965).
- [72] H. Shiba, *Prog. Theor. Phys.* **40**, 435 (1968).
- [73] A. I. Rusinov, *JETP Lett.* **9**, 85 (1969).
- [74] N. E. Hussey, *Adv. Phys.* **51**, 1685 (2002).
- [75] A. V. Balatsky, I. Vekhter, and J.-X. Zhu, *Rev. Mod. Phys.* **78**, 373 (2006).
- [76] A. Yazdani, B. A. Jones, C. P. Lutz, M. F. Crommie, and D. M. Eigler, *Science* **275**, 1767 (1997).
- [77] S. Grothe, S. Chi, P. Dosanjh, R. Liang, W. N. Hardy, S. A. Burke, D. A. Bonn, and Y. Pennec, *Phys. Rev. B* **86**, 174503 (2012).

- [78] W. Li, H. Ding, P. Deng, K. Chang, C. Song, K. He, L. Wang, X. Ma, J.-P. Hu, X. Chen, *et al.*, [Nat. Phys. \*\*8\*\*, 126 \(2012\)](#).
- [79] H. Yang, Z. Wang, D. Fang, Q. Deng, Q.-H. Wang, Y.-Y. Xiang, Y. Yang, and H.-H. Wen, [Nat. Commun. \*\*4\*\*, 2749 \(2013\)](#).
- [80] Q. Fan, W. Zhang, X. Liu, Y. Yan, M. Ren, R. Peng, H. Xu, B. Xie, J. Hu, T. Zhang, *et al.*, [Nat. Phys. \*\*11\*\*, 946 \(2015\)](#).
- [81] X. Chen, V. Mishra, S. Maiti, and P. J. Hirschfeld, [Phys. Rev. B \*\*94\*\*, 054524 \(2016\)](#).
- [82] W. Ku, H. Rosner, W. E. Pickett, and R. T. Scalettar, [Phys. Rev. Lett. \*\*89\*\*, 167204 \(2002\)](#).
- [83] A. A. Mostofi, J. R. Yates, G. Pizzi, Y.-S. Lee, I. Souza, D. Vanderbilt, and N. Marzari, [Comput. Phys. Commun. \*\*185\*\*, 2309 \(2014\)](#).
- [84] C.-L. Song, Y.-L. Wang, P. Cheng, Y.-P. Jiang, W. Li, T. Zhang, Z. Li, K. He, L. Wang, J.-F. Jia, H.-H. Hung, C. Wu, X. Ma, X. Chen, and Q.-K. Xue, [Science \*\*332\*\*, 1410 \(2011\)](#).
- [85] T. Watashige, Y. Tsutsumi, T. Hanaguri, Y. Kohsaka, S. Kasahara, A. Furusaki, M. Sigrist, C. Meingast, T. Wolf, H. v. Löhneysen, T. Shibauchi, and Y. Matsuda, [Phys. Rev. X \*\*5\*\*, 031022 \(2015\)](#).
- [86] S. Chi, R. Aluru, U. R. Singh, R. Liang, W. N. Hardy, D. A. Bonn, A. Kreisel, B. M. Andersen, R. Nelson, T. Berlijn, W. Ku, P. J. Hirschfeld, and P. Wahl, [Phys. Rev. B \*\*94\*\*, 134515 \(2016\)](#).
- [87] X. Zhou, C. Ye, P. Cai, X. Wang, X. Chen, and Y. Wang, [Phys. Rev. Lett. \*\*106\*\*, 087001 \(2011\)](#).
- [88] M. N. Gastiasoro, P. J. Hirschfeld, and B. M. Andersen, [Phys. Rev. B \*\*89\*\*, 100502 \(2014\)](#).
- [89] D. Huang, T. A. Webb, C.-L. Song, C.-Z. Chang, J. S. Moodera, E. Kaxiras, and J. E. Hoffman, [Nano Lett. \*\*16\*\*, 4224 \(2016\)](#).
- [90] T. Kariyado and M. Ogata, [J. Phys. Soc. Jpn. \*\*79\*\*, 083704 \(2010\)](#).
- [91] R. Beaird, I. Vekhter, and J.-X. Zhu, [Phys. Rev. B \*\*86\*\*, 140507 \(2012\)](#).
- [92] M. N. Gastiasoro, P. J. Hirschfeld, and B. M. Andersen, [Phys. Rev. B \*\*88\*\*, 220509 \(2013\)](#).
- [93] Q.-E. Wang, Z.-J. Yao, and F.-C. Zhang, [Europhys. Lett. \*\*101\*\*, 57002 \(2013\)](#).
- [94] S. Margadonna, Y. Takabayashi, M. T. McDonald, K. Kasperkiewicz, Y. Mizuguchi, Y. Takano, A. N. Fitch, E. Suard, and K. Prassides, [Chem. Commun. \*\*43\*\*, 5607 \(2008\)](#).

- [95] K. Schwarz, P. Blaha, and G. Madsen, *Comput. Phys. Commun.* **147**, 71 (2002).
- [96] M. D. Watson, T. K. Kim, L. C. Rhodes, M. Eschrig, M. Hoesch, A. A. Haghighirad, and A. I. Coldea, *Phys. Rev. B* **94**, 201107 (2016).
- [97] M. D. Watson, T. K. Kim, A. A. Haghighirad, N. R. Davies, A. McCollam, A. Narayanan, S. F. Blake, Y. L. Chen, S. Ghannadzadeh, A. J. Schofield, M. Hoesch, C. Meingast, T. Wolf, and A. I. Coldea, *Phys. Rev. B* **91**, 155106 (2015).
- [98] P. J. Hirschfeld, M. M. Korshunov, and I. I. Mazin, *Rep. Prog. Phys.* **74**, 124508 (2011).
- [99] A. Chubukov, *Annu. Rev. Condens. Matter Phys.* **3**, 57 (2012).
- [100] P. J. Hirschfeld, *C. R. Phys.* **17**, 197 (2016).
- [101] I. I. Mazin, D. J. Singh, M. D. Johannes, and M. H. Du, *Phys. Rev. Lett.* **101**, 057003 (2008).
- [102] A. F. Kemper, T. A. Maier, S. Graser, H.-P. Cheng, P. J. Hirschfeld, and D. J. Scalapino, *New J. Phys.* **12**, 073030 (2010).
- [103] R. M. Fernandes and A. V. Chubukov, *Rep. Prog. Phys.* **80**, 014503 (2017).
- [104] K. Kuroki, S. Onari, R. Arita, H. Usui, Y. Tanaka, H. Kontani, and H. Aoki, *Phys. Rev. Lett.* **101**, 087004 (2008).
- [105] S. Graser, T. A. Maier, P. J. Hirschfeld, and D. J. Scalapino, *New J. Phys.* **11**, 025016 (2009).
- [106] T. Moriya and K. Ueda, *Rep. Prog. Phys.* **66**, 1299 (2003).
- [107] K. Nakamura, R. Arita, and H. Ikeda, *Phys. Rev. B* **83**, 144512 (2011).
- [108] T. Berlijn, C.-H. Lin, W. Garber, and W. Ku, *Phys. Rev. Lett.* **108**, 207003 (2012).
- [109] A. Kreisel, R. Nelson, T. Berlijn, W. Ku, R. Aluru, S. Chi, H. Zhou, U. R. Singh, P. Wahl, R. Liang, W. N. Hardy, D. A. Bonn, P. J. Hirschfeld, and B. M. Andersen, *Phys. Rev. B* **94**, 224518 (2016).
- [110] A. Kreisel, P. Choubey, T. Berlijn, W. Ku, B. M. Andersen, and P. J. Hirschfeld, *Phys. Rev. Lett.* **114**, 217002 (2015).
- [111] A. Yazdani, C. M. Howald, C. P. Lutz, A. Kapitulnik, and D. M. Eigler, *Phys. Rev. Lett.* **83**, 176 (1999).
- [112] T. Machida, T. Kato, H. Nakamura, M. Fujimoto, T. Mochiku, S. Ooi, A. D. Thakur, H. Sakata, and K. Hirata, *Phys. Rev. B* **84**, 064501 (2011).

- [113] M. H. Hamidian, I. A. Firmo, K. Fujita, S. Mukhopadhyay, J. W. Orenstein, H. Eisaki, S. Uchida, M. J. Lawler, E.-A. Kim, and J. C. Davis, [New J. Phys. \*\*14\*\*, 053017 \(2012\)](#).
- [114] M. E. Flatté, [Phys. Rev. B \*\*61\*\*, R14920 \(2000\)](#).
- [115] J.-M. Tang and M. E. Flatté, [Phys. Rev. B \*\*66\*\*, 060504 \(2002\)](#).
- [116] J.-M. Tang and M. E. Flatté, [Phys. Rev. B \*\*70\*\*, 140510 \(2004\)](#).
- [117] A. Polkovnikov, S. Sachdev, and M. Vojta, [Phys. Rev. Lett. \*\*86\*\*, 296 \(2001\)](#).
- [118] B. M. Andersen, A. Melikyan, T. S. Nunner, and P. J. Hirschfeld, [Phys. Rev. Lett. \*\*96\*\*, 097004 \(2006\)](#).
- [119] J.-X. Zhu, C. S. Ting, and C.-R. Hu, [Phys. Rev. B \*\*62\*\*, 6027 \(2000\)](#).
- [120] L.-L. Wang, P. J. Hirschfeld, and H.-P. Cheng, [Phys. Rev. B \*\*72\*\*, 224516 \(2005\)](#).
- [121] J. Nieminen, I. Suominen, R. S. Markiewicz, H. Lin, and A. Bansil, [Phys. Rev. B \*\*80\*\*, 134509 \(2009\)](#).
- [122] M. I. Salkola, A. V. Balatsky, and J. R. Schrieffer, [Phys. Rev. B \*\*55\*\*, 12648 \(1997\)](#).
- [123] M. S. Hybertsen and L. F. Mattheiss, [Phys. Rev. Lett. \*\*60\*\*, 1661 \(1988\)](#).
- [124] R. S. Markiewicz, S. Sahrakorpi, M. Lindroos, H. Lin, and A. Bansil, [Phys. Rev. B \*\*72\*\*, 054519 \(2005\)](#).
- [125] Y. Kohsaka, C. Taylor, P. Wahl, A. Schmidt, J. Lee, K. Fujita, J. W. Alldredge, K. McElroy, J. Lee, H. Eisaki, S. Uchida, D.-H. Lee, and J. C. Davis, [Nature \*\*454\*\*, 1072 \(2008\)](#).
- [126] J. W. Alldredge, J. Lee, K. McElroy, M. Wang, K. Fujita, Y. Kohsaka, C. Taylor, H. Eisaki, S. Uchida, P. J. Hirschfeld, and J. C. Davis, [Nat. Phys. \*\*4\*\*, 319 \(2008\)](#).
- [127] S. H. Pan, J. P. O’Neal, R. L. Badzey, C. Chamon, H. Ding, J. R. Engelbrecht, Z. Wang, H. Eisaki, S. Uchida, A. K. Gupta, K.-W. Ng, E. W. Hudson, K. M. Lang, and J. C. Davis, [Nature \*\*413\*\*, 282 \(2001\)](#).
- [128] K. McElroy, D.-H. Lee, J. E. Hoffman, K. M. Lang, J. Lee, E. W. Hudson, H. Eisaki, S. Uchida, and J. C. Davis, [Phys. Rev. Lett. \*\*94\*\*, 197005 \(2005\)](#).
- [129] N. Miyakawa, J. F. Zasadzinski, L. Ozyuzer, P. Guptasarma, D. G. Hinks, C. Kendziora, and K. E. Gray, [Phys. Rev. Lett. \*\*83\*\*, 1018 \(1999\)](#).
- [130] N. Jenkins, Y. Fasano, C. Berthod, I. Maggio-Aprile, A. Piriou, E. Giannini, B. W. Hoogenboom, C. Hess, T. Cren, and O. Fischer, [Phys. Rev. Lett. \*\*103\*\*, 227001 \(2009\)](#).

- [131] C. Lubritto, K. Rosciszewski, and A. M. Oles, *J. Phys. Condens. Matter* **8**, 11053 (1996).
- [132] E. Pavarini, I. Dasgupta, T. Saha-Dasgupta, O. Jepsen, and O. K. Andersen, *Phys. Rev. Lett.* **87**, 047003 (2001).
- [133] C. Weber, K. Haule, and G. Kotliar, *Phys. Rev. B* **82**, 125107 (2010).
- [134] X. Wang, H. T. Dang, and A. J. Millis, *Phys. Rev. B* **84**, 014530 (2011).
- [135] L. Hozoi, L. Siurakshina, P. Fulde, and J. van den Brink, *Sci. Rep.* **1**, 65 (2011).
- [136] H. Sakakibara, K. Suzuki, H. Usui, S. Miyao, I. Maruyama, K. Kusakabe, R. Arita, H. Aoki, and K. Kuroki, *Phys. Rev. B* **89**, 224505 (2014).
- [137] H. Sakakibara, H. Usui, K. Kuroki, R. Arita, and H. Aoki, *Phys. Rev. B* **85**, 064501 (2012).
- [138] V. I. Anisimov, D. E. Kondakov, A. V. Kozhevnikov, I. A. Nekrasov, Z. V. Pchelkina, J. W. Allen, S.-K. Mo, H.-D. Kim, P. Metcalf, S. Suga, A. Sekiyama, G. Keller, I. Leonov, X. Ren, and D. Vollhardt, *Phys. Rev. B* **71**, 125119 (2005).
- [139] J. Kurzyk, W. Wójcik, and J. Spalek, *Eur. Phys. J. B* **66**, 385 (2008).
- [140] J. Spalek, J. Kurzyk, R. Podsiadły, and W. Wójcik, *Eur. Phys. J. B* **74**, 63 (2010).
- [141] P. T. Sprunger, L. Petersen, E. W. Plummer, E. Lægsgaard, and F. Besenbacher, *Science* **275**, 1764 (1997).
- [142] J. E. Hoffman, K. McElroy, D.-H. Lee, K. M. Lang, H. Eisaki, S. Uchida, and J. C. Davis, *Science* **297**, 1148 (2002).
- [143] K. Fujita, C. K. Kim, I. Lee, J. Lee, M. H. Hamidian, I. A. Firmo, S. Mukhopadhyay, H. Eisaki, S. Uchida, M. J. Lawler, E.-A. Kim, and J. C. Davis, *Science* **344**, 612 (2014).
- [144] Q.-H. Wang and D.-H. Lee, *Phys. Rev. B* **67**, 020511 (2003).
- [145] L. Capriotti, D. J. Scalapino, and R. D. Sedgewick, *Phys. Rev. B* **68**, 014508 (2003).
- [146] T. Pereg-Barnea and M. Franz, *Phys. Rev. B* **68**, 180506 (2003).
- [147] D. Zhang and C. S. Ting, *Phys. Rev. B* **67**, 100506 (2003).
- [148] B. M. Andersen and P. Hedegård, *Phys. Rev. B* **67**, 172505 (2003).
- [149] L. Zhu, W. A. Atkinson, and P. J. Hirschfeld, *Phys. Rev. B* **69**, 060503 (2004).
- [150] T. S. Nunner, W. Chen, B. M. Andersen, A. Melikyan, and P. J. Hirschfeld, *Phys. Rev. B* **73**, 104511 (2006).

- [151] E. A. Nowadnick, B. Moritz, and T. P. Devereaux, [Phys. Rev. B](#) **86**, 134509 (2012).
- [152] P. Choubey, W.-L. Tu, T.-K. Lee, and P. J. Hirschfeld, [New J. Phys.](#) **19**, 013028 (2017).
- [153] R. E. Peierls, *Quantum theory of solids* (Oxford University Press, 1955).
- [154] J.-P. Pouget, [C. R. Phys.](#) **17**, 332 (2016).
- [155] G. Grüner, [Rev. Mod. Phys.](#) **60**, 1129 (1988).
- [156] K. Miyagawa, A. Kawamoto, and K. Kanoda, [Phys. Rev. B](#) **62**, R7679 (2000).
- [157] J. M. Tranquada, D. J. Buttrey, and V. Sachan, [Phys. Rev. B](#) **54**, 12318 (1996).
- [158] H. Yoshizawa, H. Kawano, Y. Tomioka, and Y. Tokura, [Phys. Rev. B](#) **52**, R13145 (1995).
- [159] M. Cwik, M. Benomar, T. Finger, Y. Sidis, D. Senff, M. Reuther, T. Lorenz, and M. Braden, [Phys. Rev. Lett.](#) **102**, 057201 (2009).
- [160] C.-W. Chen, J. Choe, and E. Morosan, [Rep. Prog. Phys.](#) **79**, 084505 (2016).
- [161] S. A. Kivelson, I. P. Bindloss, E. Fradkin, V. Oganesyan, J. M. Tranquada, A. Kapitulnik, and C. Howald, [Rev. Mod. Phys.](#) **75**, 1201 (2003).
- [162] M. Vojta, [Adv. Phys.](#) **58**, 699 (2009).
- [163] E. Fradkin, S. A. Kivelson, and J. M. Tranquada, [Rev. Mod. Phys.](#) **87**, 457 (2015).
- [164] J. M. Tranquada, B. J. Sternlieb, J. D. Axe, Y. Nakamura, and S. Uchida, [Nature](#) **375**, 561 (1995).
- [165] J. M. Tranquada, J. D. Axe, N. Ichikawa, Y. Nakamura, S. Uchida, and B. Nachumi, [Phys. Rev. B](#) **54**, 7489 (1996).
- [166] A. R. Moodenbaugh, Y. Xu, M. Suenaga, T. J. Folkerts, and R. N. Shelton, [Phys. Rev. B](#) **38**, 4596 (1988).
- [167] G. Ghiringhelli, M. Le Tacon, M. Minola, S. Blanco-Canosa, C. Mazzoli, N. B. Brookes, G. M. De Luca, A. Frano, D. G. Hawthorn, F. He, T. Loew, M. M. Sala, D. C. Peets, M. Salluzzo, E. Schierle, R. Sutarto, G. A. Sawatzky, E. Weschke, B. Keimer, and L. Braicovich, [Science](#) **337**, 821 (2012).
- [168] J. Chang, E. Blackburn, A. T. Holmes, N. B. Christensen, J. Larsen, J. Mesot, R. Liang, D. A. Bonn, W. N. Hardy, A. Watenphul, M. v. Zimmermann, E. M. Forgan, and S. M. Hayden, [Nat. Phys.](#) **8**, 871 (2012).
- [169] R. Comin, A. Frano, M. M. Yee, Y. Yoshida, H. Eisaki, E. Schierle, E. Weschke, R. Sutarto, F. He, A. Soumyanarayanan, Y. He, M. Le Tacon, I. S. Elfimov, J. E. Hoffman, G. A. Sawatzky, B. Keimer, and A. Damascelli, [Science](#) **343**, 390 (2014).

- [170] N. Doiron-Leyraud, S. Lepault, O. Cyr-Choinière, B. Vignolle, G. Grissonnanche, F. Laliberté, J. Chang, N. Barišić, M. K. Chan, L. Ji, X. Zhao, Y. Li, M. Greven, C. Proust, and L. Taillefer, [Phys. Rev. X \*\*3\*\*, 021019 \(2013\)](#).
- [171] N. Barisic, S. Badoux, M. K. Chan, C. Dorow, W. Tabis, B. Vignolle, G. Yu, J. Beard, X. Zhao, C. Proust, and M. Greven, [Nat. Phys. \*\*9\*\*, 761 \(2013\)](#).
- [172] T. Wu, H. Mayaffre, S. Kramer, M. Horvatic, C. Berthier, P. L. Kuhns, A. P. Reyes, R. Liang, W. N. Hardy, D. A. Bonn, and M.-H. Julien, [Nat. Commun. \*\*4\*\*, 2113 EP \(2013\)](#).
- [173] E. H. da Silva Neto, P. Aynajian, A. Frano, R. Comin, E. Schierle, E. Weschke, A. Gyenis, J. Wen, J. Schneeloch, Z. Xu, S. Ono, G. Gu, M. Le Tacon, and A. Yazdani, [Science \*\*343\*\*, 393 \(2014\)](#).
- [174] W. D. Wise, M. C. Boyer, K. Chatterjee, T. Kondo, T. Takeuchi, H. Ikuta, Y. Wang, and E. W. Hudson, [Nat. Phys. \*\*4\*\*, 696 \(2008\)](#).
- [175] M. J. Lawler, K. Fujita, J. Lee, A. R. Schmidt, Y. Kohsaka, C. K. Kim, H. Eisaki, S. Uchida, J. C. Davis, J. P. Sethna, and E.-A. Kim, [Nature \*\*466\*\*, 347 \(2010\)](#).
- [176] E. Blackburn, J. Chang, M. Hücker, A. T. Holmes, N. B. Christensen, R. Liang, D. A. Bonn, W. N. Hardy, U. Rütt, O. Gutowski, M. v. Zimmermann, E. M. Forgan, and S. M. Hayden, [Phys. Rev. Lett. \*\*110\*\*, 137004 \(2013\)](#).
- [177] A. J. Achkar, R. Sutarto, X. Mao, F. He, A. Frano, S. Blanco-Canosa, M. Le Tacon, G. Ghiringhelli, L. Braicovich, M. Minola, M. Moretti Sala, C. Mazzoli, R. Liang, D. A. Bonn, W. N. Hardy, B. Keimer, G. A. Sawatzky, and D. G. Hawthorn, [Phys. Rev. Lett. \*\*109\*\*, 167001 \(2012\)](#).
- [178] S. Blanco-Canosa, A. Frano, T. Loew, Y. Lu, J. Porras, G. Ghiringhelli, M. Minola, C. Mazzoli, L. Braicovich, E. Schierle, E. Weschke, M. Le Tacon, and B. Keimer, [Phys. Rev. Lett. \*\*110\*\*, 187001 \(2013\)](#).
- [179] R. Comin, R. Sutarto, F. He, E. H. da Silva Neto, L. Chauviere, A. Frano, R. Liang, W. N. Hardy, D. A. Bonn, Y. Yoshida, H. Eisaki, A. J. Achkar, D. G. Hawthorn, B. Keimer, G. A. Sawatzky, and A. Damascelli, [Nat. Mater. \*\*14\*\*, 796 \(2015\)](#).
- [180] S. Sachdev and R. La Placa, [Phys. Rev. Lett. \*\*111\*\*, 027202 \(2013\)](#).
- [181] J. Šmakov, I. Martin, and A. V. Balatsky, [Phys. Rev. B \*\*64\*\*, 212506 \(2001\)](#).
- [182] M. H. Hamidian, S. D. Edkins, S. H. Joo, A. Kostin, H. Eisaki, S. Uchida, M. J. Lawler, E.-A. Kim, A. P. Mackenzie, K. Fujita, J. Lee, and J. C. S. Davis, [Nature \*\*532\*\*, 343 \(2016\)](#).
- [183] A. Abanov, A. V. Chubukov, and J. Schmalian, [Adv. Phys. \*\*52\*\*, 119 \(2003\)](#).
- [184] M. A. Metlitski and S. Sachdev, [Phys. Rev. B \*\*82\*\*, 075128 \(2010\)](#).

- [185] Y. Wang and A. Chubukov, [Phys. Rev. B \*\*90\*\*, 035149 \(2014\)](#).
- [186] K. B. Efetov, H. Meier, and C. Pepin, [Nat. Phys. \*\*9\*\*, 442 \(2013\)](#).
- [187] T. Holder and W. Metzner, [Phys. Rev. B \*\*85\*\*, 165130 \(2012\)](#).
- [188] V. Mishra and M. R. Norman, [Phys. Rev. B \*\*92\*\*, 060507 \(2015\)](#).
- [189] K.-Y. Yang, W. Q. Chen, T. M. Rice, M. Sigrist, and F.-C. Zhang, [New. J. Phys. \*\*11\*\*, 055053 \(2009\)](#).
- [190] W.-L. Tu and T.-K. Lee, [Sci. Rep. \*\*6\*\*, 18675 \(2016\)](#).
- [191] A. Himeda, T. Kato, and M. Ogata, [Phys. Rev. Lett. \*\*88\*\*, 117001 \(2002\)](#).
- [192] M. Raczkowski, M. Capello, D. Poilblanc, R. Frésard, and A. M. Oleś, [Phys. Rev. B \*\*76\*\*, 140505 \(2007\)](#).
- [193] C.-P. Chou, N. Fukushima, and T. K. Lee, [Phys. Rev. B \*\*78\*\*, 134530 \(2008\)](#).
- [194] W.-J. Hu, F. Becca, and S. Sorella, [Phys. Rev. B \*\*85\*\*, 081110 \(2012\)](#).
- [195] P. Corboz, T. M. Rice, and M. Troyer, [Phys. Rev. Lett. \*\*113\*\*, 046402 \(2014\)](#).
- [196] A. Allais, J. Bauer, and S. Sachdev, [Phys. Rev. B \*\*90\*\*, 155114 \(2014\)](#).
- [197] V. J. Emery, [Phys. Rev. Lett. \*\*58\*\*, 2794 \(1987\)](#).
- [198] S. Bulut, W. A. Atkinson, and A. P. Kampf, [Phys. Rev. B \*\*88\*\*, 155132 \(2013\)](#).
- [199] W. A. Atkinson, A. P. Kampf, and S. Bulut, [New. J. Phys. \*\*17\*\*, 013025 \(2015\)](#).
- [200] M. C. Gutzwiller, [Phys. Rev. Lett. \*\*10\*\*, 159 \(1963\)](#).
- [201] M. C. Gutzwiller, [Phys. Rev. \*\*137\*\*, A1726 \(1965\)](#).
- [202] D. Vollhardt, [Rev. Mod. Phys. \*\*56\*\*, 99 \(1984\)](#).
- [203] A. Himeda and M. Ogata, [Phys. Rev. B \*\*60\*\*, R9935 \(1999\)](#).
- [204] R. B. Christensen, P. J. Hirschfeld, and B. M. Andersen, [Phys. Rev. B \*\*84\*\*, 184511 \(2011\)](#).
- [205] F. Loder, A. P. Kampf, and T. Kopp, [Phys. Rev. B \*\*81\*\*, 020511 \(2010\)](#).
- [206] H. Jang, W.-S. Lee, H. Nojiri, S. Matsuzawa, H. Yasumura, L. Nie, A. V. Maharaj, S. Gerber, Y.-J. Liu, A. Mehta, D. A. Bonn, R. Liang, W. N. Hardy, C. A. Burns, Z. Islam, S. Song, J. Hastings, T. P. Devereaux, Z.-X. Shen, S. A. Kivelson, C.-C. Kao, D. Zhu, and J.-S. Lee, [Proc. Natl. Acad. Sci. \*\*113\*\*, 14645 \(2016\)](#).
- [207] A. B. Vorontsov, J. A. Sauls, and M. J. Graf, [Phys. Rev. B \*\*72\*\*, 184501 \(2005\)](#).

- [208] T. Valla, A. V. Fedorov, P. D. Johnson, Q. Li, G. D. Gu, and N. Koshizuka, *Phys. Rev. Lett.* **85**, 828 (2000).
- [209] A. Kaminski, H. M. Fretwell, M. R. Norman, M. Randeria, S. Rosenkranz, U. Chatterjee, J. C. Campuzano, J. Mesot, T. Sato, T. Takahashi, T. Terashima, M. Takano, K. Kadowaki, Z. Z. Li, and H. Raffy, *Phys. Rev. B* **71**, 014517 (2005).
- [210] T. Berlijn, D. Volja, and W. Ku, *Phys. Rev. Lett.* **106**, 077005 (2011).
- [211] D. Korotin, A. V. Kozhevnikov, S. L. Skornyakov, I. Leonov, N. Binggeli, V. I. Anisimov, and G. Trimarchi, *Eur. Phys. J. B* **65**, 91 (2008).
- [212] V. I. Anisimov, *AIP Conf. Proc.* **1297**, 3 (2010)

## BIOGRAPHICAL SKETCH

Peayush Choubey was born in Ballia, India. He completed his schooling in his hometown, and admitted to the Indian School of Mines, Dhanbad, India, in 2004, where he graduated with Bachelor of Technology degree in Electronics Engineering in 2008. Subsequently, He worked at the Center for Airborne Systems, Bangalore, India. In fall 2010, he went to the University of Florida, Gainesville, USA, and completed his Doctor of Philosophy in physics in spring 2017.